ROMA TRE
UNIVERSITÀ DEGLI STUDI

Science Department

Matter Science, Nanotechnology and Complex Systems

PhD Thesis

Thiol-functionalized gold and silver nanoparticles using mixed ligands: a close look at the atomic structure and chemico-physical properties by SR-XPS and SERS

Tutor:
Prof. Chiara Battocchio

PhD Student:
Laura Carlini

Academic Year 2017/2018

To my family
& my friends.

For their love,
endless support,
& encouragement.

Contents

List of Figures

List of Tables

Introduction

In recent years the field of *Nanotechnology* has shown increasing prominence in the scientific, regulatory, and public spheres. The development of nano-sized systems (with dimensions in the range of $10^{-9} \div 10^{-7}$ m) has been improved more and more, exploring all the possible applications of nano-structured systems, from medicine to electronics to cultural heritage. The possibility to tune (*e.g.* by controlling size and surface functionalization) a wide range of properties in these nanosystems promotes their use in many fields, from catalysis [1] to optics [2] to biomedicine [3]. It is mandatory to achieve a fine control of the chemico-physical properties of these nanosystems, thus, the field of nanotechnologies welcomes a "multidisciplinary task force" of physicists, chemists, biologists, computer engineers, and so on, to design, produce and fully characterize these systems.

Among the different nano-sized systems, *Noble Metal Nanoparticles* (MNPs) have been proven themselves to be a very useful tool in the biological field (*e.g.* gold nanoparticles have shown a great efficacy as radiosensitizers under X-Ray irradiation for cancer treatment *in vivo* [4]), due to the peculiar properties that MNPs show in the nanoscale range. Metal nanoparticles are formed by few atoms ($10^1 \div 10^6$) and their dimensions usually vary from 1 to 10^2 nm, *e.g.* a gold nanoparticle of about 1 nm is made of a cluster with ca. 55 atoms [5]. They can show a wide range of shape (spheres, nanocages, nanorods, nanostars, *etc...*) and dimension, according to the synthesis procedure and the envisaged applications. Nanometric size and chemical versatility of these systems are the fundamental parameters that justify the huge nanomaterials diffusion.

Concerning noble metal nanoparticles (like Au, Ag, Pd and Pt), it is noteworthy that their proprieties at the nanoscale range were exploited without awareness since Roman Ages. Indeed, in our history there are several references to solutions of "colloidal gold", *e.g.* ancient chinese medicine books refer to "gold solutions" (V-IV century *BC*), at the same time Indians were using a treatment called "liquid gold", while in the renaissance Europe the colloidal gold were used to treat many different diseases [6].

In recent years, MNPs have been used for diagnostic and therapeutic purposes, as well as for microscopy, bioimaging and immunology. Nanometric dimensions promote the nanoparticles use as carriers for delivering therapeutics to disease sites, opening up new therapeutic strategies in cancer therapy or antimicrobial treatments [7, 8]. Besides *Drug Delivery*, nanomaterials applications are emerging in anti-tumoral therapies, like *Plasmonic Photo-Thermal Therapy* (PPTT), *Photodynamic Therapy* (PDT) and *Radiotherapy* (RT) as well[1].

The striking difference in color between bulk metals and metal nanoparticles corresponds to dramatic changes in material properties [9], the different optical response at the nanoscale range is due to the *plasmon resonance* energy shift of metal nanoparticles as the particle size changes. Nowadays, the study of the interaction between light and nanometric particles of noble metals have lead to useful applications in the field of medicine. Indeed, one of the most exploited application of metal nanoparticles is their use as radiosensitizers due to their higher energy-absorbing property when compared to soft tissues, which enables a local physical dose enhancement [10]. However, the exploitation of nanoparticle-light interaction is not the only example of the noble metal nanoparticle huge influence in medicine and biology. Nanomaterials properties exploitation in medicine has been so intense that the nanomedicine main aim has become "the use of nanostructures for diagnostic and therapeutic purposes[2]" [11].

This PhD project is focused on the study of the structural, electronic and morphological properties of MNPs for innovative applications in nanomedicine and nano-biotechnology. A key point for the technological development of nano-structured materials and practical biomedical devices based on MNPs is the achievement of a fine control of the stability and toxicity of the system. The chemical functionalization of metal nanoparticles can be done by means of capping metallic clusters with appropriate organic ligands. The *molecule-capping method* provides a reliable control of particle composition, shape and size distribution making the functionalized MNPs suitable for active purposes in catalysis, nanoelectronics, sensing and bio-

---

[1] PPTT is a minimally-invasive therapy in which photon energy is converted into heat to kill cancer. PDT involves administration of a photosensitizing agent followed by irradiation at a wavelength corresponding to an absorbance band of the sensitizer. In the presence of oxygen, a series of events lead to direct tumor cell death, damages to the microvasculature and induction of a local inflammatory reaction. RT consists in the use of *Ionizing Radiation* (IR) to induce DNA damage in tumor cells.

[2] The possibility of introducing functionalized metallic nanoparticles into living cells or living organisms enables many *in vitro* and *in vivo* medical applications beyond diagnostics and therapy, including theranostics and surgery guidance (with sufficient sensitivity).

analysis [12]. Indeed, the capping molecules play a double role: on one hand, they protect and stabilize the MNPs, preventing their aggregation; on the other, they can be opportunely selected to functionalize the metal cluster, thus making the resulting hybrid system better suited for the application of interest. To answer to the constant demand for more stable and functional nanoparticles, this PhD project provides a deep study concerning the fully characterization, by means of *Synchrotron Radiation induced X-Ray Photoelectron Spectroscopy* (SR-XPS) and *Surface-Enhanced Raman Spectroscopy* (SERS), of innovative noble metal (Au, Ag) nanoparticles, which can selectively enter tumors, act as suitable candidate for drug delivery, for diagnostic or radiosensing applications.

The here presented gold and silver nanoparticles functionalized with mixed organic ligands, the *3-mercapto-1-propansulfonate* (3MPS) and the *2-diethylaminoethanethiol hydrochloride* (DEA), were prepared with different metal/thiol stoichiometric molar ratios with the aim to modulate the properties of the functionalized nanoparticles. Gold and silver nanoparticles, composed of a metallic core and a ligand shell show a peculiar optical behaviour and provide a very powerful tool for biotechnological applications. The molecular overlayer has been selected on purpose for the biomedical applications [13], as well as to stabilize the nanoparticles. The changes in the stoichiometric ratio between metal and different capping agents can influence the chemical properties of ligands functional groups and the dimension of the functionalized MNPs. Moreover, the biocompatibility of the system depends strictly on the charge and thickness of capping molecules layer.

The investigation of the structural and electronic properties of this complex nanosystems was carried out by means of SR-XPS, with the aim to probe the nature of the interactions at the metal/organic ligands interface as well as the stability of the functionalized systems and capping molecules. SR-XPS data allow to achieve a deep understanding of the influence of the thiols stoichiometric ratio on the electronic properties and stability of functionalized noble metal nanoparticles. SR-XPS provides information on the local bonding environment of a given species and it has been demonstrated to be an unique tool for investigating the nature of the interaction at the capping agent/metal nanoparticle interface, as well as the chemical structure of MNPs surface [14].

The study of the interaction between light and metallic nanostructures is a rapidly emerging research area known as *plasmonics*[3]. SERS is a highly

---

[3] *Surface plasmons* (SPs) are the collective excitation of free conductive electrons excited by electromagnetic radiation at the metal-dielectric interface. They are supported by noble metal thin films or noble metal nanoparticles surfaces.

specific molecular technique that uses plasmonics to obtain detailed chemical information of molecules or molecular assemblies adsorbed or attached to nanostructured metallic surfaces. This powerful technique is based on the enhancement of the Raman signal of molecules situated in the near vicinity of metallic nanostructures to obtain detailed information regarding the identity of those molecules, with sensitivities down to single-molecule level. SERS has many advantages over ordinary spectroscopic analytical techniques such as extremely high sensitivity, molecular selectivity, intense signals and great precision. Thus, this technique is well suitable for bioanalytical investigation applied to small molecules, proteins, DNA, and biologically relevant nanoparticles [15].

Complementary information about the electronic, chemical and molecular structure can be obtained combining SERS and SR-XPS data, allowing to evidence structural similarities and differences related to the noble metal choice and to the synthesis stoichiometric molar ratio. In conclusion, this PhD project compares the semi-quantitative SR-XPS and SERS analysis to obtain a better understanding of the system, exploring the potential synergy between different techniques in order to give new insights in the field of nanomaterials.

Dithiols-functionalized nanoparticles-based networks

In the last section of Chapter 5 a nano-structured system formed by networks of MNPs (Au, Ag or PdNPs) will be presented and the main results obtained by means of SR-XPS analysis will be reported and discussed.

While many studies have tackled the synthesis and characterization of gold dimers and networks with peculiar plasmon resonance behaviour [16, 17], organization of Ag and PdNPs in 2D or 3D superlattices is less common. The characteristic plasmonic properties of MNPs are strongly dependent on interparticle interactions, since in the near-field adjacent particles may couple together the plasmon oscillations. The frequency of coupled-particle *Localized Surface Plasmon Resonance* (LSPR) is generally shifted from the single particle resonance depending on the strength of the inter-particle coupling that, in turn, is a function of interparticle spacing. Therefore, obtaining conveniently spaced nanoparticles with sharp interparticle distance distribution is mandatory for applicative purposes, from analytical sensors to catalysis and fuel cells. Bi-functional ligands with intrinsic self-assembling properties are specially suited in this context, as they produce ordered 2D or 3D networks with reproducible interparticle spacing [18].

Bifunctional organometallic ligands with terminal dithiols have been used as efficient stabilizing agents preparing MNPs by grafting them with *trans,*

trans-$[CH_3CO\text{-}S\text{-}Pt(PBu_3)_2(C{\equiv}C\text{-}C_6H_4\text{-}C_6H_4\text{-}C{\equiv}C)\text{-}Pt(PBu_3)_2\text{-}S\text{-}COCH_3]$ (Pt-DEBP) which was in situ deacylated to give the -SH derivative covalently bound to Au, Ag or Pd [19, 20]. Pt(II) organometallic complexes and related oligomers show self-assembly ability to form different nanoscale supramolecular architectures; in particular, Pt-containing rod-like organometallic polymer shows molecular arrangement in the *trans* configuration and an unusual supramolecular structure of Pt-DEBP in the *cis* configuration [21].

The three-dimensional network structure arising from self-assembly of Pt complex and Au, Ag and PdNPs stabilized with this bifunctional organometallic dithiolate have been investigated. SR-XPS is a well suited technique to investigate the sulfur-metal bond of self-assembled monolayers of organometallic thiols on flat surfaces, as well as MNPs. The here reported results show that organometallic dithiols can be successfully used to stabilize gold, silver and palladium nanoparticles, leading to complex arrangements in dyads. It should be noted that the LSPR is definitively affected by the nature of the MNP surface and the chemical bonds at the interface between the capping agents and the metal.

The NPs metal choice leads to peculiar plasmon resonance behaviour stressing out interesting differences in sensing and emission properties. Thus, the here reported study compares dithiols-functionalized Au, Ag and PdNPs-based networks, establishing correlations between organometallic superstructures and noble metal nanoparticles on the basis of their very different chemico-physical properties.

Chapter 1

Photoemission and Raman effect theories

The processes of absorption, emission and diffusion of photons are the basis of all the experimental techniques for the study of systems of particles (like atoms, molecules and solids) [22]. They can be described by perturbation expansion, at the various level of approximations. In the following sections, from the photoemission and Raman effect theories here presented, will be derived the *quantum differential cross sections* describing these processes.

1.1 The radiation-matter interaction

In the classical elettrodynamics the free electromagnetic field is described by the Maxwell equations[1]:

$$\begin{aligned} \nabla \cdot \mathbf{E} = 4\pi\rho \qquad & \nabla \times \mathbf{B} = \frac{4\pi \mathbf{J}}{c} + \frac{1}{c}\frac{\partial \mathbf{E}}{\partial t} \\ \nabla \cdot \mathbf{B} = 0 \qquad & \nabla \times \mathbf{E} = -\frac{1}{c}\frac{\partial \mathbf{B}}{\partial t} \end{aligned}$$

where ρ is the charge density and $\mathbf{J}$ is the current density.
Now, by substituting

$$4\pi\varepsilon_0 = 1; \quad \mu_0 = 1/\varepsilon_0 c^2; \quad \mathbf{B} \to \mathbf{B}/c$$

the electric field and the magnetic induction field have the same units and the electromagnetic force on a charge q, that moves with velocity v, is given by:

$$\mathbf{F} = q\mathbf{E} + q\frac{v}{c} \times \mathbf{B}$$

---

[1] In the SI system.

The real vector fields $\mathbf{E}(\mathbf{r},t)$ and $\mathbf{B}(\mathbf{r},t)$ that are solutions of Maxwell equations can be derived by a scalar potential $\varphi(\mathbf{r},t)$ and vector potential $\mathbf{A}(\mathbf{r},t)$ through the relations

$$\begin{aligned} \mathbf{E}(\mathbf{r},t) &= -\nabla\varphi(\mathbf{r},t) - \frac{1}{c}\frac{\partial \mathbf{A}(\mathbf{r},t)}{\partial t} && (1.1) \\ \mathbf{B}(\mathbf{r},t) &= \nabla \times \mathbf{A}(\mathbf{r},t) && (1.2) \end{aligned}$$

The 1.1 and 1.2 are left unchanged under *Gauge transformations* on the potentials

$$\varphi(\mathbf{r},t) \to \varphi(\mathbf{r},t) + \frac{1}{c}\frac{\partial f(\mathbf{r},t)}{\partial t} \quad ; \quad \mathbf{A}(\mathbf{r},t) \to \mathbf{A}(\mathbf{r},t) - \nabla f(\mathbf{r},t)$$

The equation of motion for the potentials can be obtained by substitution in the Maxwell equation:

$$\begin{aligned} \nabla(\nabla\cdot\mathbf{A}) &- \nabla^2\mathbf{A} + \frac{1}{c^2}\frac{\partial}{\partial t}\nabla\varphi + \frac{1}{c^2}\frac{\partial^2 \mathbf{A}}{\partial^2 t} = \frac{4\pi}{c}\mathbf{J} && (1.3) \\ &- \nabla^2\varphi - \nabla\cdot(\frac{1}{c}\frac{\partial \mathbf{A}}{\partial t}) = 4\pi\rho && (1.4) \end{aligned}$$

where $\rho(\mathbf{r},t)$ and $\mathbf{J}(\mathbf{r},t)$ are the charge density and the current density, respectively. Now, a vector field can be written as a sum of a conservative or irrotational field (*transverse*) and a solenoidal field with zero divergence (*longitudinal*):

$$\begin{aligned} \nabla\cdot\mathbf{J}_T = 0 \qquad &\textit{and} \qquad \nabla\times\mathbf{J}_L = 0 \\ \mathbf{J}(\mathbf{r},t) = \ &\mathbf{J}_T(\mathbf{r},t) + \ \mathbf{J}_L(\mathbf{r},t) \end{aligned}$$

As a consequence of this substitution only $\mathbf{J}_L$ appears in the continuity equation

$$\nabla\mathbf{J}_L = -\frac{\partial\rho}{\partial t}$$

The separation into a transverse and a longitudinal part can be done also for the potential $\mathbf{A}$. It is easy to observe that a gauge transformation affects only the scalar potential $\varphi(\mathbf{r},t)$ and the longitudinal part of vector potential $\mathbf{A}_L(\mathbf{r},t)$. Therefore the transverse part $\mathbf{A}_T(\mathbf{r},t)$ in *gauge invariant.*

Out of the domain of high-energy physics the so called *Coulomb gauge*[2] is the convenient choice of the gauge in order to have $\nabla\cdot\mathbf{A} = 0$ or identically

---

[2] The convenient choice of the gauge for the description of the interaction between free high-energy charged particles and e.m. fiel is the *Lorentz gauge*. In this approach the potential $A^\mu = (\varphi, \mathbf{A})$ is a 4-vector where $\mu = 0,1,2,3$ labels the 4-coordinates. Time and space coordinates are grouped into a 4-vector $x^\mu = (ct, \mathbf{r})$. The Lorentz-gauge condition is $(\partial/\partial x^\mu)A^\mu = 0$, that has the advantage to be relativistically covariant.

$\mathbf{A}_L = 0$. Thus, in this gauge, the equations of the potentials are decoupled:

$$\begin{aligned} -\nabla^2\varphi &= 4\pi\rho && (1.5) \\ -\nabla^2\mathbf{A} + \frac{1}{c}\frac{\partial^2\mathbf{A}}{\partial^2 t} &= \frac{4\pi}{c}\mathbf{J}_T && (1.6) \end{aligned}$$

From equation 1.4 a particular solution can be chosen in the form:

$$\varphi(\mathbf{r}, t) = \int d\mathbf{r}' \frac{\rho(\mathbf{r}', t)}{|\mathbf{r} - \mathbf{r}'|}$$

The scalar potential becomes the *electrostatic* potential determined by the charge distribution at the same fixed time in all space (*instantaneous Coulomb potential*). As a consequence, a particular solution of 1.6 is given by

$$\mathbf{A}(\mathbf{r}, t) = \int d\mathbf{r}' \frac{\mathbf{J}_T(\mathbf{r}', t')}{|\mathbf{r} - \mathbf{r}'|}$$

$$t' = t - \frac{|\mathbf{r} - \mathbf{r}'|}{c}$$

The vector potential is due to the distribution of the transverse density of current, this dependency takes account of the retardation effect due to the finite value of the velocity of light.

Now, in absence of charge or current

$$\varphi = 0 \quad ; \quad \nabla^2\mathbf{A} - \frac{1}{c^2}\frac{\partial^2\mathbf{A}}{\partial^2 t} = 0 \tag{1.7}$$

The solution for the free electromagnetic field can be expanded in complex plane waves (each of them identified by the wavevector $\mathbf{k}$ and the polarization index s)

$$\mathbf{A}(\mathbf{r}, t) = \sum_{\mathbf{k},s}(\mathcal{A}(\mathbf{k}, s)\hat{\epsilon}_{s\mathbf{k}} e^{i\mathbf{k}\cdot\mathbf{r} - i\omega_{\mathbf{k}}t} + \mathcal{A}^*(\mathbf{k}, s)\hat{\epsilon}^*_{s\mathbf{k}} e^{-i\mathbf{k}\cdot\mathbf{r} + i\omega_{\mathbf{k}}t}) \tag{1.8}$$

Fixing the normalization volume $\mathcal{V} = L_x L_y L_z$ (with the requirement that $\mathcal{V} \to \infty$ will not affect the calculations), adopting the *periodic boundary conditions* on the whole volume $\mathcal{V}$ and considering that n_x, n_y, n_z span the whole set of relative integers, the grid of allowed wavevectors $\mathbf{k}$ is given by

$$\mathbf{k} = 2\pi(\frac{n_x}{L_x}, \frac{n_y}{L_y}, \frac{n_z}{L_z})$$

For each wavevector, there are two independent polarization vectors[3], orthogonal to $\mathbf{k}$

$$\hat{\epsilon}_{1\mathbf{k}} \cdot \mathbf{k} = 0 \qquad \hat{\epsilon}_{2\mathbf{k}} \cdot \mathbf{k} = 0$$

$$\textit{and} \qquad \hat{\epsilon}_{1\mathbf{k}} \cdot \hat{\epsilon}^*_{2\mathbf{k}} = 0$$

and the angular frequency of each mode is given by

$$\omega_{\mathbf{k}} = c|\mathbf{k}|$$

Using the definition of vector potential $\mathbf{A}(\mathbf{r}, t)$, the electric fiel $\mathbf{E}(\mathbf{r}, t)$ and the magnetic induction field $\mathbf{B}(\mathbf{r}, t)$ can be derived by equation 1.1 and 1.2, respectively. And the total energy of the free field, in absence of charges and current, is the Hamiltonian:

$$\mathcal{H}_f = \frac{1}{8\pi} \int (\mathbf{E}^2 + \mathbf{B}^2) d\mathbf{r} \tag{1.9}$$

Now, defining new *adimensional dynamical variables*[4], $a_{\mathbf{k}s}(t)$ and its hermitian conjugate $a^\dagger_{\mathbf{k}s}(t)$, the expansion of the vector potential can be written as

$$\mathbf{A}(\mathbf{r}, t) = \sum_{\mathbf{k},s} \left(\frac{4\pi\hbar c^2}{2\mathcal{V}\omega_{\mathbf{k}}} \right)^{\frac{1}{2}} (a_{\mathbf{k}s}(t)\hat{\epsilon}_{s\mathbf{k}} e^{i\mathbf{k}\cdot\mathbf{r}} + a^\dagger_{\mathbf{k}s}(t)\hat{\epsilon}^*_{s\mathbf{k}} e^{-i\mathbf{k}\cdot\mathbf{r}}) \tag{1.10}$$

By substituting the equation 1.10 into eqs. 1.1 and 1.2 and using the 1.9, the total energy of the free e.m. field is

---

[3] If $\hat{\epsilon}_{1\mathbf{k}}$ and $\hat{\epsilon}_{2\mathbf{k}}$ are real, they represent the two linear polarizations; if they are complex vectors

$$\hat{\epsilon}_{(+)\mathbf{k}} = -\frac{1}{2}(\hat{\epsilon}_{1\mathbf{k}} + i\hat{\epsilon}_{2\mathbf{k}}) \quad \textit{and} \quad \hat{\epsilon}_{(-)\mathbf{k}} = \frac{1}{2}(\hat{\epsilon}_{1\mathbf{k}} - i\hat{\epsilon}_{2\mathbf{k}})$$

they describe circular polarizations (left and right, respectively).

[4] This new variables can be considered not as scalar quantities but as *quantum operators* with the commutation rules

$$[a_{\mathbf{k}s}(t), a^\dagger_{\mathbf{k}'s'}(t)] = \delta_{\mathbf{k}\mathbf{k}'}\delta_{ss'}$$

where $[a, b] = ab - ba$. From equations 1.7 the following expressions can be obtained:

$$\frac{\partial^2}{\partial t^2} a_{\mathbf{k}s}(t) = -\omega^2_{\mathbf{k}} a_{\mathbf{k}s}(t) \quad \rightarrow \quad a_{\mathbf{k}s}(t) = a_{\mathbf{k}s}(t) e^{-i\omega_{\mathbf{k}} t}$$

and in the same way $a^\dagger_{\mathbf{k}s}(t) = a^\dagger_{\mathbf{k}s}(t) e^{i\omega_{\mathbf{k}} t}$.

$$\mathcal{H}_f = \sum_{\mathbf{k},s} \frac{1}{2}\hbar\omega_{\mathbf{k}}(a^{\dagger}_{\mathbf{k}s}a_{\mathbf{k}s} + a_{\mathbf{k}s}a^{\dagger}_{\mathbf{k}s})$$

that is independent on time and, imposing the commutation relations, the energy assumes the familiar expression:

$$\mathcal{H}_f = \sum_{\mathbf{k},s} \hbar\omega_{\mathbf{k}} \left(a^{\dagger}_{\mathbf{k}s}a_{\mathbf{k}s} + \frac{1}{2}\right) \tag{1.11}$$

Now, by defining the hermitian *number operators*[5] $\check{n}_{\mathbf{k}s} = a^{\dagger}_{\mathbf{k}s}a_{\mathbf{k}s}$, *eigenstates* and *eigenvalues* of number operators $\check{n}_{\mathbf{k}s}|n_{\mathbf{k}s}\rangle = n_{\mathbf{k}s}|n_{\mathbf{k}s}\rangle$ (with $n_{\mathbf{k}s} = 0, 1, 2, ...$), the following properties derive from the commutation rules:

$$\begin{array}{ll} \check{n}_{\mathbf{k}s}(a_{\mathbf{k}s}|n_{\mathbf{k}s}\rangle) = (n_{\mathbf{k}s} - 1)(a_{\mathbf{k}s}|n_{\mathbf{k}s}\rangle) & \langle n_{\mathbf{k}s}|n_{\mathbf{k}s}\rangle = 1 \\ \check{n}_{\mathbf{k}s}(a^{\dagger}_{\mathbf{k}s}|n_{\mathbf{k}s}\rangle) = (n_{\mathbf{k}s} + 1)(a^{\dagger}_{\mathbf{k}s}|n_{\mathbf{k}s}\rangle) & |n_{\mathbf{k}s}\rangle = \dfrac{(a^{\dagger}_{\mathbf{k}s})^{n_{\mathbf{k}s}}}{\sqrt{n_{\mathbf{k}s}!}}|0_{\mathbf{k}s}\rangle \end{array}$$

Thus $a_{\mathbf{k}s}$ and $a^{\dagger}_{\mathbf{k}s}$ are respectively the operators of *annihilation* and *creation*. They change by a unit the number of photons in the states with defined photon number.

A quantum state defined by the number of photons in each mode is

$$|\{n_{\mathbf{k}s}\}\rangle = |...n_{\mathbf{k}s}...\rangle \prod_{\mathbf{k_i}} \prod_{s_i} |n_{\mathbf{k_i}s_i}\rangle$$

where each state is labelled by the set of *occupation numbers*, giving the number of photons for each mode. This is the basis set for a *coherent* quantum state of the e.m. field and any quantum state of the free field is a linear combination of such states.

These states have a well defined number of photons and a well defined energy. They are eigenstates of N (that define the total number of photons) and H_f

$$\begin{aligned} N_{\{n_{\mathbf{k}s}\}} &= \sum_{\mathbf{k}_i s_i} n_{\mathbf{k}_i s_i} \\ E_{\{n_{\mathbf{k}s}\}} &= \sum_{\mathbf{k}_i s_i} \hbar\omega_{\mathbf{k}_i} \left(n_{\mathbf{k}_i s_i} + \frac{1}{2}\right) \end{aligned}$$

---

[5] The number operators act on a quantum state $|\Psi_{\mathbf{k}s}\rangle$ that is a *ket* vector in the Hilbert space of quantum states associated the $(\mathbf{k}s)$ mode. $|\Psi_{\mathbf{k}s}\rangle$ is a superposition of the eigenstates of the number operator

$$|\Psi_{\mathbf{k}s}\rangle = \sum_{n_{\mathbf{k}s}} c_{n_{\mathbf{k}s}} |n_{\mathbf{k}s}\rangle.$$

Using the quantum description the fields are *quantum operators*, with a part containing absorption operators, where only positive frequencies appear, and another containing creation operators, where only negative frequencies are present in the phase factors. They are observable with expectation values given by the average value (*expectation value*) on the quantum state.

Indeed, looking at the equation 1.10, the vector potential is formed by a "positive-frequency term" and a "negative-frequency term":

$$\mathbf{A}(\mathbf{r},t) = \mathbf{A}^{(+)}(\mathbf{r},t) + \mathbf{A}^{(-)}(\mathbf{r},t)$$

the first term is a combination of operators that in each mode destroy a photon, the second is made of operators that create a photon. Both are acting on the vector space of quantum states at defined photon number.

We can derive the operators of the same form that represent the electric and the magnetic field:

$$\begin{aligned}
\mathbf{E}(\mathbf{r},t) &= \sum_{\mathbf{k},s} i \left(\frac{4\pi\hbar\omega_{\mathbf{k}}}{2\mathcal{V}}\right)^{\frac{1}{2}} \left(a_{\mathbf{k}s}(t)\hat{\epsilon}_{s\mathbf{k}} e^{i\mathbf{k}\cdot\mathbf{r}-i\omega_{\mathbf{k}}t} - a^{\dagger}_{\mathbf{k}s}(t)\hat{\epsilon}^{*}_{s\mathbf{k}} e^{-i\mathbf{k}\cdot\mathbf{r}+1\omega_{\mathbf{k}}t}\right) \\
\mathbf{B}(\mathbf{r},t) &= \sum_{\mathbf{k},s} i \left(\frac{4\pi\hbar\omega_{\mathbf{k}}}{2\mathcal{V}}\right)^{\frac{1}{2}} \left(a_{\mathbf{k}s}(t)(\hat{k}\times\hat{\epsilon}_{s\mathbf{k}}) e^{i\mathbf{k}\cdot\mathbf{r}-i\omega_{\mathbf{k}}t} - a^{\dagger}_{\mathbf{k}s}(t)(\hat{k}\times\hat{\epsilon}^{*}_{s\mathbf{k}}) e^{-i\mathbf{k}\cdot\mathbf{r}+1\omega_{\mathbf{k}}t}\right)
\end{aligned}$$

where $\hat{k} = \mathbf{k}/k$ is the direction of the propagating wave.

It is easy to observe that the expectation value of the vector operator $\mathbf{E}(\mathbf{r},t)$ on the quantum state with definite number of photons is equal to zero[6], *i.e.*

$$\langle\{n_{\mathbf{k}s}\}|\mathbf{E}(\mathbf{r},t)|\{n_{\mathbf{k}s}\}\rangle = 0$$

On the contrary, the square modulus of the electric field is completely well defined (the same for magnetic field)

$$\langle\{n_{\mathbf{k}s}\}|\mathbf{E}^2(\mathbf{r},t)|\{n_{\mathbf{k}s}\}\rangle = 4\pi\hbar\omega_{\mathbf{k}}\left(n_{\mathbf{k}s}+\frac{1}{2}\right)$$

To reproduce the behaviour of a classical wave of a given wavevector $\mathbf{k}$ and polarization $\widehat{\epsilon}_s$, a well defined coherent superposition of many states with different numbers of photons in the same mode has to been built:

$$|\phi >= e^{-\frac{1}{2}|\alpha^2|}\sum_{n}\frac{\alpha^n}{(n!)^{\frac{1}{2}}}|n\rangle \qquad (1.12)$$

---

[6] This is due to the effect of the presence in the field operator $\mathbf{E}(\mathbf{r},t)$ of the absorption and creation operators, that are "non-diagonal" in the photon number eingestates.

The equation 1.12 describes a quantum state reproducing a monochromatic polarized electromagnetic wave obtained with a single mode coherent superposition of many-photon states with appropriate coefficients [23]. This state is not an eingestate of the number of photons.

Interaction of the e.m. field with a system of charged particles Now, considering a system of N moving particles (an atom, a molecule or a solid) with mass m_i and charge q_i with $i = 1, 2, ...N$, the quantum behaviour of the system is described by the commutation relations to which the dynamical variables (coordinates $\mathbf{r}_i$ and their conjugate momenta $\mathbf{p}_i$) have to obey

$$[r_{i\alpha}, p_{j\beta}] = i\hbar\delta_{ij}\delta_{\alpha\beta}$$

where the greek letters indicate the cartesian components.

In the Coulomb gauge the electric field contains, in the presence of charges, an irrotational (or conservative) part contributing to the total energy with the term

$$\frac{1}{8\pi}\int \mathbf{E}_L^2 d\mathbf{r} = \frac{1}{8\pi}\int (\nabla\varphi)^2 d\mathbf{r} = \frac{1}{8\pi}\int (-\varphi\nabla^2\varphi) d\mathbf{r} = \frac{1}{2}\int \frac{\rho(\mathbf{r},t)\rho(\mathbf{r}',t)}{|\mathbf{r}-\mathbf{r}'|} d\mathbf{r}d\mathbf{r}'$$

The last term, for a system of point charges, reduces to the instantaneous electrostatic interaction, having the well known form of the Coulombic potential energy

$$\frac{1}{2}\sum_{i\neq j}\frac{q_i q_j}{|\mathbf{r}_i - \mathbf{r}_j|}$$

Now, if the charges move in the e.m. field, the presence of the transverse radiation field is related to the following substitution for each momentum

$$\mathbf{p}_i \to \mathbf{p}_i - \frac{q_i}{c}\mathbf{A}(\mathbf{r}_j)$$

In this way, considering also the kinetic energy $\sum_i \mathbf{p}_i^2/2m_i$, the Hamiltonian of the system of charges becomes

$$\mathcal{H}_s = \sum_i \frac{1}{2m_i}\left(\mathbf{p}_i - \frac{q}{c}\mathbf{A}(\mathbf{r}_i)\right)^2 + \frac{1}{2}\sum_{i\neq j}\frac{q_i q_j}{|\mathbf{r}_i - \mathbf{r}_j|}$$

To obtain the total Hamiltonian (*charged system + free field + interaction*) it is convenient to consider different contributions

$$\mathcal{H} = \mathcal{H}_s + \mathcal{H}_f = \mathcal{H}_s^0 + \mathcal{H}_f + \mathcal{H}_I = \mathcal{H}_0 + \mathcal{H}_I$$

where $\mathcal{H}_0$ is the *unperturbed Hamiltonian*[7] and $\mathcal{H}_I$ is the interaction term

$$\begin{aligned}\mathcal{H}_0 &= \sum_i \frac{\mathbf{p}_i^2}{2m_i} + \frac{1}{2}\sum_{i\neq j}\frac{q_i q_j}{|\mathbf{r}_i - \mathbf{r}_j|} + \sum_{\mathbf{k},s}\hbar\omega_k\left(a^\dagger_{\mathbf{k}s}a_{\mathbf{k}s} + \frac{1}{2}\right)\\ \mathcal{H}_I &= \sum_i\left\{-\frac{q_i}{2m_i c}(\mathbf{p}_i\cdot\mathbf{A}(\mathbf{r}_i) + \mathbf{A}(\mathbf{r}_i)\cdot\mathbf{p}_i) + \frac{q_i^2}{2m_i c^2}\mathbf{A}^2(\mathbf{r}_i)\right\}\end{aligned}$$

Finally, using the Coulomb gauge condition $\nabla\cdot\mathbf{A} = 0$, the interaction term becomes

$$\mathcal{H}_I = \sum_i\left(-\frac{q_i}{m_i c}\mathbf{A}(\mathbf{r}_i)\cdot\mathbf{p}_i + \frac{q_i^2}{2m_i c^2}\mathbf{A}^2(\mathbf{r}_i)\right) \tag{1.13}$$

containing a linear and a quadratic term in the radiation field operator[8].

Now, considering an atom, a molecule or a solid, it is convenient to separate the coordinates of the nuclei from the electron variables and treat the first ones as classical objects

$$\mathcal{H}_s^0 = \sum_i\frac{\mathbf{p}_i^2}{2m_i} - \sum_I\frac{Z_I e^2}{|\mathbf{R}_I - \mathbf{r}_i|} + \frac{1}{2}\sum_{i\neq j}\frac{e^2}{|\mathbf{r}_i - \mathbf{r}_j|} + \frac{1}{2}\sum_{I\neq J}\frac{e^2}{|\mathbf{R}_I - \mathbf{R}_J|}$$

where $\mathbf{R}$ and $\mathbf{r}$ indicate the nuclei and the electrons coordinates, respectively.

Elementary processes: absorption and emission of a photon

The state $|\Psi_\alpha\rangle$ of the N charges system with the appropriate set of quantum numbers α and corresponding energy eigenvalue E_α can be projected onto the $3N$-coordinate cartesian space, giving the (more familiar) expression for the N-particles wavefunction

$$\Psi_\alpha(\mathbf{r}_1, \mathbf{r}_2, ..., \mathbf{r}_N) = \langle\mathbf{r}_1, \mathbf{r}_2, ..., \mathbf{r}_N|\Psi_\alpha\rangle$$

---

[7] The unperturbed Hamiltonian $\mathcal{H}_0$ describes both the system of interacting charges and the free radiation field.

[8] It is noteworthy that the total Hamiltonian of the system should takes into account the following relativistic corrections to the unperturbed Hamiltonian

$$-\frac{e}{2m^2c^2}\sum_i\mathbf{S}_i\cdot(\nabla\varphi(\mathbf{r}_i)\times\mathbf{p}_i) - \frac{1}{8m^3c^6}\sum_i\mathbf{p}_i^4 - \frac{e\hbar^2}{8m^2c^2}\sum_i\Delta\varphi(\mathbf{r}_i)$$

where the first term is the *spin-orbit contribution*, the second one is the relativistic correction to the kinetic energy and the last term is the *Darwin term*. On the other hand the interaction term becomes

$$\frac{e}{mc}\sum_i\mathbf{S}_i(\nabla\times\mathbf{A}(\mathbf{r}_i,t)) - \frac{e^2}{2m^2c^4}\sum_i\mathbf{S}_i\left(\frac{\partial\mathbf{A}(\mathbf{r}_i,t)}{\partial t}\times\mathbf{A}(\mathbf{r}_i,t)\right)$$

describing the interaction between the spin of the electrons and the electromagnetic field.

and the *unperturbed* eigenstates of non-interacting Hamiltonian $\mathcal{H}_0$ (with energy $E_\alpha + E_{\{n_{\mathbf{k}s}\}}$) can be described as

$$|\Psi\rangle = |\Psi_\alpha\rangle \otimes |\{n_{\mathbf{k}s}\}\rangle$$

where $|\{n_{\mathbf{k}s}\}\rangle$ is a state for the radiation field with fixed photon numbers.

If the electrons are described in a quantum picture and the state is depending also on ion positions $\{\mathbf{R}_i\}$ treated as classical parameters, interchanging two electron coordinates, the wavefunction or the state changes sign (according to the fermionic nature of electrons). Now, considering the evolution of a state due to the interaction 1.13 between matter and the radiation field, if the interaction is switched on at t_i and is turned off at t_f, the evolution of the system can be described in term of an *amplitude of transition*[9] among the states of the unperturbed system:

$$\langle\Psi_b|U(t_f, t_i)|\Psi_a\rangle$$

Adopting the Heisenberg picture for the non-interacting system (working in the so-called *Interaction picture*), the states of the “free system” do not evolve in time

$$|\Psi_a^I\rangle = e^{i\mathcal{H}_{\prime}t/\hbar}|\Psi_a\rangle$$

and the amplitude of transition can be written as

$$S_{ba} = \langle\Psi_b^I|\tilde{U}(t_f, t_i)|\Psi_a^I\rangle$$

where

$$\tilde{U}(t_f, t_i) = e^{i\mathcal{H}_{\prime}t/\hbar}U(t_f, t_i)e^{-i\mathcal{H}_{\prime}t/\hbar}$$

is the *evolution operator*[10] in the interaction representation.

---

[9] The amplitude of transition between $|\Psi_a\rangle$ and $|\Psi_b\rangle$ is a complex value whose square-modulus indicates the probability that the non-interacting system in the state $|\Psi_a\rangle$ at the time t_i will be found in the state $|\Psi_b\rangle$ at the time t_f, as a consequence of the interaction.

[10] The link between this operator and the interaction Hamiltonian is given by the expansion

$$\tilde{U}(t_f, t_i) = 1 + \sum_{n=1}^{\infty} \tilde{U}^{(n)}(t_f, t_i)$$

where

$$\tilde{U}^{(n)}(t_f, t_i) = \left(\frac{1}{i\hbar}\right)^n \int_{t_f \geq \tau_n \geq \tau_{n-1}} d\tau_n ... \int_{\tau_2 \geq \tau_1 \geq t_i} d\tau_1 \tilde{\mathcal{H}}_I(\tau_n)...\tilde{\mathcal{H}}_I(\tau_1)$$

and

$$\tilde{\mathcal{H}}_I(t) = e^{i\mathcal{H}_{\prime}t/\hbar}\mathcal{H}_I e^{-i\mathcal{H}_{\prime}t/\hbar}$$

This expansion at different order n is the basis of the *Feynman diagrams* of the interaction processes.

Now, considering the first order processes and including only the linear term of 1.13, the transition amplitude between $|\Psi_a\rangle = |\Psi_A, n_{\mathbf{k}s}\rangle$ initial state and $|\Psi_b\rangle = |\Psi_B, n_{\mathbf{k}s} \mp 1\rangle$ final state[11] becomes

$$S^{1a}_{ab} = \frac{e}{i\hbar m}\left(\frac{4\pi\hbar}{2\mathcal{V}\omega_{\mathbf{k}}}\right)^{\frac{1}{2}} \times$$

$$\times\langle n_{\mathbf{k}s} - 1|a_{\mathbf{k}s}|n_{\mathbf{k}s}\rangle\langle\Psi_B|\sum_i e^{i\mathbf{k}\cdot\mathbf{r}_i}\hat{\epsilon}_{s\mathbf{k}}\cdot\mathbf{p}_i|\Psi_A\rangle\times$$

$$\times\int_{t_f\geq\tau\geq\tau_i} exp\left(\frac{i}{\hbar}(E_B - E_A - \hbar\omega_{\mathbf{k}})\right)d\tau =$$

$$= -\frac{2i\pi e}{m}\left(\frac{4\pi\hbar}{2\mathcal{V}\omega_{\mathbf{k}}}\right)^{\frac{1}{2}}(n_{\mathbf{k}s})^{\frac{1}{2}}\hat{\epsilon}_{s\mathbf{k}}\cdot\langle\Psi_B|\sum_i e^{i\mathbf{k}\cdot\mathbf{r}_i}\mathbf{p}_i|\Psi_A\rangle\delta(E_B - E_A - \hbar\omega_k) \quad (1.14)$$

and refers to the diagram displayed in figure 1.1(a), representing the absorption of a photon. The time integral shown in 1.14 is extended from the beginning to the end of the interaction (from $-\infty$ to $+\infty$) and gives the conservation of energy.

The emission process, taking place only starting from an excited states[12] ($E_A > E_B$), is described by the Feynman diagram shown in 1.1(b) and the corresponding transition amplitude is

$$S^{1b}_{ab} = -\frac{2i\pi e}{m}\left(\frac{4\pi\hbar}{2\mathcal{V}\omega_{\mathbf{k}}}\right)^{\frac{1}{2}}(n_{\mathbf{k}s}+1)^{\frac{1}{2}}\hat{\epsilon}^*_{s\mathbf{k}}\cdot\langle\Psi_B|\sum_i e^{-i\mathbf{k}\cdot\mathbf{r}_i}\mathbf{p}_i|\Psi_A\rangle\delta(E_B - E_A + \hbar\omega_k)$$

The *transition matrix element*[13] can be expanded as

$$e^{i\mathbf{k}\cdot\mathbf{r}_i} = 1 + i\mathbf{k}\cdot\mathbf{r}_i + ... \quad (1.15)$$

assuming that generally the wavelength $\lambda = 2\pi/k$ is great respect to the atomic dimensions, *i.e.* $\mathbf{k}$ can be considered small.

---

[11] The number of photons in the final and initial states have difference ∓ 1, in the mode $\mathbf{k}s$, and the number of photons must be the same (even zero) for all other modes; the *absorption* of a photon corresponds to (-1) and the *emission* to $(+1)$.

[12] The probability of emission of photons in excited systems increases with the number of photons present in a single mode. This process is important in quantum optical devices (*stimulated emission*).

[13] The matrix element of the linear part of the interaction is described by

$$\langle\Psi_B|\sum_i e^{i\mathbf{k}\cdot\mathbf{r}_i}\mathbf{p}_i|\Psi_A\rangle$$

and involves the polarization of the mode $\mathbf{k}s$ and the quantum states of the system.

It is possible in many cases[14] to evaluated the matrix element in the *dipole approximation*, retaining only the first term of the expansion[15] 1.15. In this approximation the matrix element becomes

$$\langle \Psi_B | \sum_i \mathbf{p}_i | \Psi_A \rangle$$

and can be written also in an other form[16]

$$\langle \Psi_B | \sum_i \mathbf{p}_i | \Psi_A \rangle = \frac{m}{i\hbar} \langle \Psi_B | \mathbf{r}_i \mathcal{H}_s^0 - \mathcal{H}_s^0 \mathbf{r}_i | \Psi_A \rangle =$$

$$= im \frac{E_B - E_A}{\hbar} \langle \Psi_B | \mathbf{r}_i | \Psi_A \rangle = im\omega_{\mathbf{k}} \langle \Psi_B | \mathbf{r}_i | \Psi_A \rangle$$

using the identity $[\mathbf{r}_i, \mathcal{H}_s^0] = (i\hbar/m)\mathbf{p}_i$.

1.2 Absorption and photoemission

In the most common case, with only one photon, $n_{\mathbf{k}s}$ is equal to 1 in the initial state. The transitions from the ground state to various manifolds of excited states that can be reached by varying the energy and the polarization of the incoming photon is described by the *cross section* of the process.

Taking into account only dipole terms, the total cross section of the absorption process is given by the sum over the final states of the ratio between the square modulus of the transition amplitude and the incident flux $(c/\mathcal{V})$:

$$\sigma(\omega) = 4\pi^2 \alpha \hbar\omega \sum_B |\epsilon_s \cdot \langle \Psi_B | \sum_i \mathbf{r}_i | \Psi_A \rangle|^2 \delta(E_B - E_A - \hbar\omega)$$

As a function of ω the absorption spectrum presents a number of thresholds, peaks and structures and is a powerful instrument to investigate the atomic, molecular or material electronic structure.

Now, choosing a *one-electron picture*, $|\Psi_A\rangle$ and $|\Psi_B\rangle$ are single-electron states described by single-particle wavefunctions: $\phi_c(\mathbf{r})$ the core localized

---

[14] Given for example a photon with energy $\simeq 1000eV$, the wavelenght is large ($\simeq$ 12 Å) respect to the spatial extension of the wavefunction of an electron in a core state of an atom.

[15] To go beyond the dipole approximation or when the dipole matrix element is zero due to *selection rules*, it is mandatory to include also the second term originating the *orbital magnetic dipole contribution* and the *quadrupolar electric contribution*.

[16] The matrix element containing the momentum $\mathbf{p}$ is called *dipole velocity*, on the other hand the form of the matrix element related only to the variables $\mathbf{r}_i$ is called *dipole lenght.*

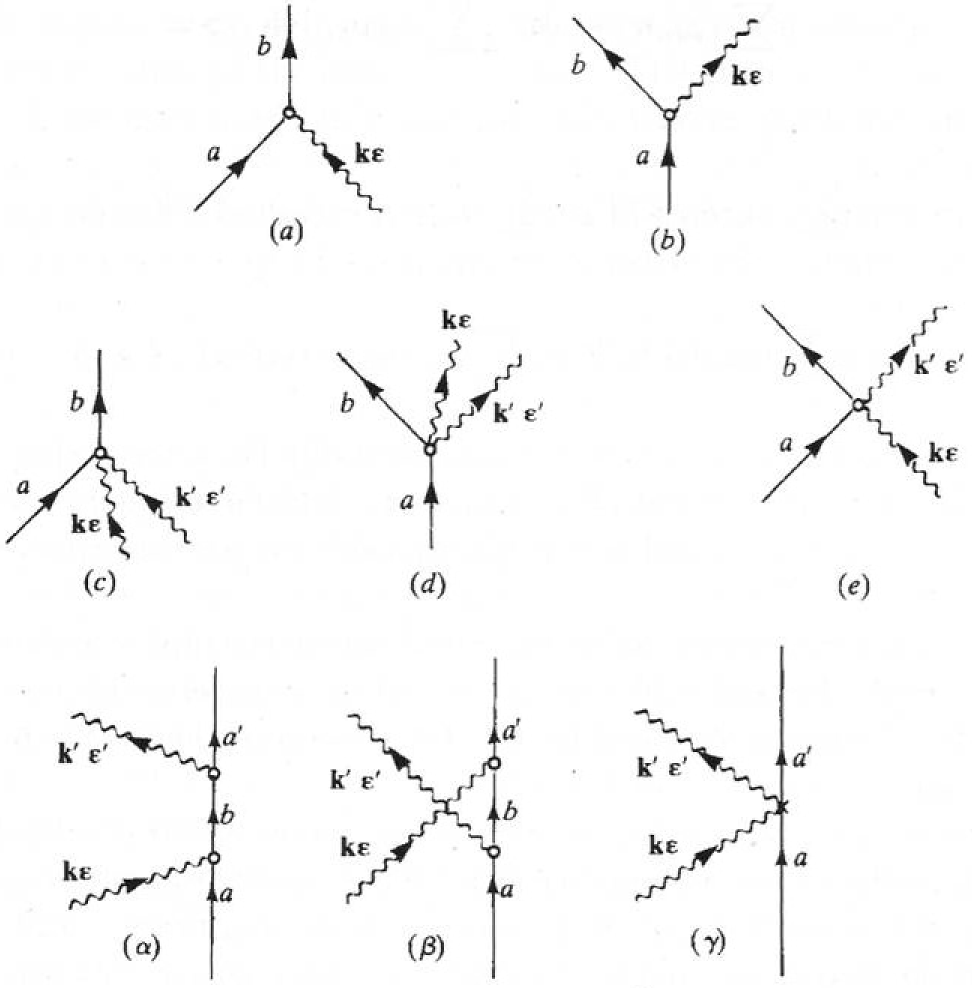

Figure 1.1: Feynman diagrams related to the absorption (a) or emission (b) of one photon due to the interaction between electrons and e.m. field. In the 2nd row, diagram (c) represents the absorption of two photons, (d) the emission of two photon and (e) the diffusion of a photon (*quadratic interaction term*). The 3rd row shows contributions at second order. The entering arrows indicate the system in state $|\Psi_A>$ and the outgoing arrows indicate the system in state $|\Psi_B>$, while the wiggling arrows represent the absorbed or emitted photon.

initial state and $\psi_k(\mathbf{r})$ the extended final state in the conduction band. Assuming that the remaining N-1 electrons do not interact during the process, their contributions can be simply neglected[17]. In this case the single electron moves in an effective potential representing the nuclei and all other electrons and the cross section becomes

$$\sigma(\omega) = 4\pi^2\alpha\hbar\omega \sum_k |\epsilon_s \cdot < \psi_k(\mathbf{r})|\mathbf{r}|\phi_c(\mathbf{r}) > |^2 \delta(\epsilon_k - \epsilon_c - \hbar\omega) \qquad (1.16)$$

$\phi_c(\mathbf{r})$ is the electron wavefunction of a core state (with negative energy ϵ_c) and $\psi_k(\mathbf{r})$ is the set of the unoccupied states of energy ϵ_k above the Fermi energy of the system, where the excited electron can be promoted. The 1.16 is the starting point to interpret the measurements of absorption profiles in the XAS (*X-ray Absorption Spectroscopy*) techniques.

The absorption of a photon can drive the system in an highly excited state in the continuum giving rise to the emission of a *photoelectron*. In the photoemission process at first-order, a hole is created in a valence or in a core state of the system and an electron is created in the continuum above the vacuum level. Thus the latter can be decomposed into a state with N-1 electrons plus a free electron in the continuum. In the one-electron picture[18] ϵ_f is the final energy of the photoemitted electron and ϵ_i is the energy of the hole[19] with $\epsilon_f > 0$ and $\epsilon_i < 0$,

$$\hbar\omega = \epsilon_f - \epsilon_i$$

Neglecting additional inelastic process, the electron is photoemitted with the following kinetic energy:

$$\frac{\hbar^2 k^2}{2m} = \epsilon_f - W = \hbar\omega - |\epsilon_i| - W$$

where W is the *Work function*[20] of the system.

---

[17] This one-particle picture is useful to describe molecule electronic structure or solid electron bands, where the multiplet splitting or other many-electron effects can be neglected.

[18] In solids, for extended electron states (uncorrelated), it is usual to work in one-electron approximation.

[19] The energies ϵ_f and ϵ_i are both expressed respect to the *Fermi level* E_F, fixed to the zero value of the energy scale chosen in this picture.

[20] The work function is the difference between the energy of the vacuum level and the Fermi energy for an electron, *i.e.* W is the barrier that an electron at the Fermi level sees passing from the system into the vacuum.

The measure of the kinetic energy allows to determine the *Binding Energy* ϵ_i. In a typical photoemission experiment, the photon energy is fixed and the number of photoelectrons is measured as a function of their kinetic energy, obtaining the *Energy Distribution Curve* (EDC) as a function of $|\epsilon_i|$. The EDC is substantially the distribution of occupied electronic state before the photoexcitation process, but its shape takes into account also *many-body effects* (correlation electron-electron) and different inelastic scattering processes of the photoelectron during its travel in the sample and across the surface of the sample to the detector.

These so-called *secondary electrons* have lost information concerning the energies of the primary process because of their inelastic interactions with the other electrons in the solid. They are moving in the conduction band continuum of states above the vacuum level and thus they are carrying information on the states of the conduction band and on the overall efficiency of the process. A schematic picture of the photoemission processes[21] is shown in figure 1.2.

From a many-electron point of view E_i^N is the N electrons initial state, while the final state is composed of the system with N-1 electrons (with energy $E_f^{N-1} + (\hbar^2 k^2)/2m$ that represents a level of a set of excited states containing a hole) plus the photoelectron. Thus the kinetic energy of the emitted electron is

$$\frac{\hbar^2 k^2}{2m} = \hbar\omega - (E_f^{N-1} - E_i^N)$$

where the *orbital energy* $(E_f^{N-1} - E_i^N)$ must be corrected to include the relaxation effect, the change in the particle density of the system induced by the hole and further corrections related to the electronic correlation:

$$(E_f^{N-1} - E_i^N) = -\epsilon_i - \Delta E_{rel} - \Delta E_{corr}$$

This expression gives an interpretation of the energy difference as a sum of three terms: an orbital energy (referred to the vacuum level) of the photoemitted electron and corrections due to the relaxation effects of the other N-1 electrons and correlation energy[22]. In metals for valence states near the Fermi energy these corrections are negligible, but usually a correlation energy should be taken into account to obtain the effective binding energy.

---

[21] The photoemission spectrum is characterized by different spectral features containing information about multiplet effect, configuration interaction, adiabatic relaxation, matrix element effects, chemical shift, change of relaxation and correlation at surfaces respect to bulk.

[22] It is noteworthy that, measuring the core level photoemission in solids, different values of the correlation and relaxation corrections can be founded at the surface respect to the bulk.

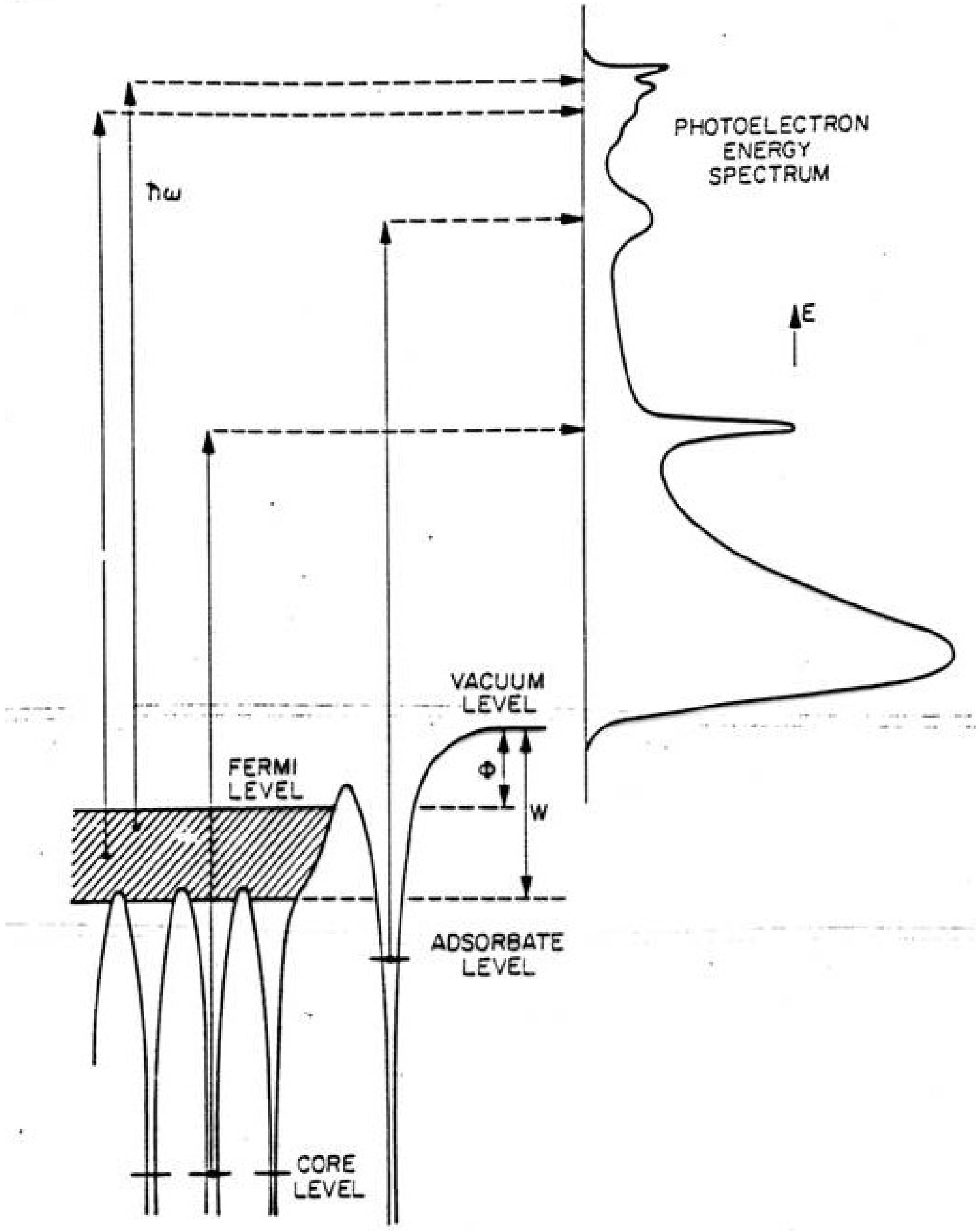

Figure 1.2: The picture shows the excitation processes of electrons from corelevels and from valence band. At low energies is visible the contribution related to the secondary electrons distribution.

Some interesting observations should be considered in the study of the photoemission process:

1. if correlation and relaxation corrections are small, the validity of the *Koopman theorem*[23] is assumed, and the ionization energy corresponds almost to the energy of the orbital of the emitted electron;
2. in the *adiabatic approximation* the process of photoemission is sufficiently slow to allow the outgoing electron "to see" the relaxation of the ion in the presence of the hole. This means that the core level EDC is characterized by a sharp peak with kinetic energy slightly larger than expected due to the relaxation of the N-1 electrons around the hole;
3. on the other hand, if the process is fast, the *sudden approximation* is valid and the EDC can have a number of structures extending to higher binding energies, *i.e.* lower kinetic energies.

The last approximation represents the case of photoemission from atoms, in which the ion left behind has a number of excited states that contribute the spectrum of the hole. In general in localized systems and in the sudden approximation conditions, many-electron effects, electronic correlation and configurational interactions can be important and dominate the photoelectron spectrum.

1.3 Raman scattering

The three last diagrams shown in figure 1.1 describe the diffusion processes. If the process is elastic, *i.e.* the energy does not change during the interaction ($\hbar\omega = \hbar\omega'$), the diffusion process is called *Rayleigh scattering*, on the contrary the *Raman scattering* is related to anelastic processes. If the energy after the interaction is lower respect the incoming energy, the process is called *Stokes* Raman scattering. On the contrary, if $\hbar\omega' > \hbar\omega$, the process is called *Anti-Stokes* scattering.

The Raman effect was observed for the first time in 1928 by Raman and Krishnan [24]. After the development of laser devices, the Raman spectroscopy has become a very useful technique for the investigation of matter,

---

[23] Koopman theorem states that the first ionization energy of a molecule is equal to the negative of the energy of the highest occupied molecular orbital (HOMO). Using the Hartree-Fock method for the approximation of orbital energy (derived from the wavefunction of the spin orbital and the kinetic and nuclear attraction energies), it is not necessary to calculate the two separate energies of the original molecule and its ion in order to find the ionization energy and electron affinity.

giving information about the internal excitations (generated or destroyed during the scattering process) of the system.

The Raman effect can be described using a *semi-classical* theory: an electromagnetic field applied to a molecular system generates a dipole momentum that depends on to the incoming field through the polarizability α:

$$P_D(\omega) = \alpha E_0 cos(\omega t) \tag{1.17}$$

where E_0 is the amplitude of the incoming field. The oscillating dipole acts as a source of electromagnetic wave. If the molecule polarizability doesn't change ($\alpha = cost$), the dipole induced radiation has the same frequency of the incoming wave (Rayleight scattering) and the intensity of the scattered radiation is

$$I = \frac{c}{8\pi}\frac{k^2}{r^2}\alpha^2 E_0^2(1 + cos^2\theta)$$

with θ angle between the incoming and the scattered wave.

Now, in case of biatomic molecules, the system can be affected by deformations associated to vibrations of the molecule *natural frequency* Ω and the distance between atoms in the system changes periodically respect the equilibrium distance R_0. The polarizzability α can be written as a function of the interatomic distance R using the following Taylor expansion:

$$\alpha(R) = \alpha(R_0) + \left(\frac{\partial\alpha}{\partial r}\right)_{R=R_0}(R - R_0) = \alpha_0 + \alpha'(R_0)(R - R_0)$$

The deformation related to the normal mode of vibration with frequency Ω can be described as

$$R = R_0 + \rho cos(\Omega t)$$

as a consequence:

$$\alpha(t) = \alpha_0 + \alpha'(R_0)\rho cos(\Omega t) = \alpha_0 + \alpha_1 cos(\Omega t) \tag{1.18}$$

From equations 1.17 and 1.18 the expression of the induced dipole can be easily obtained

$$P_D(\omega) = \alpha_0 E_0 cos(\omega t) + \frac{\alpha_1 E_0}{2}[cos((\omega + \Omega)t) + cos((\omega - \Omega)t)]$$

The molecule vibration around the frequency Ω generates electromagnetic radiation, due to the oscillating dipole, not only with the same frequency of the incoming radiation (elastic diffusion or Rayleigh scattering) but also with different frequency[24] $\omega \pm \Omega$ (Raman scattering).

The semi-classical description of the Raman effect can be useful to understand the basic concepts associated to this process but it isn't enough to fully describe the Raman scattering. To deep understand the physics behind the phenomenum a quantum theory is needed [25], *e.g.* the classical description cannot explain the fact that, experimentally, the intensity of the Anti-Stokes features in the Raman spectra usually is lower respect the intensity of the Stokes peaks.

The starting point to describe the Raman scattering is the absorption of a photon of energy $h\nu$ with the transition of the molecule from the fundamental state to a *virtual* state (see figure 1.3). This state is a quantum state with very short life time, it cannot be measured directly and, as a consequence, the value of ΔE is very high due to the *Heisenberg uncertainty principle*[25].

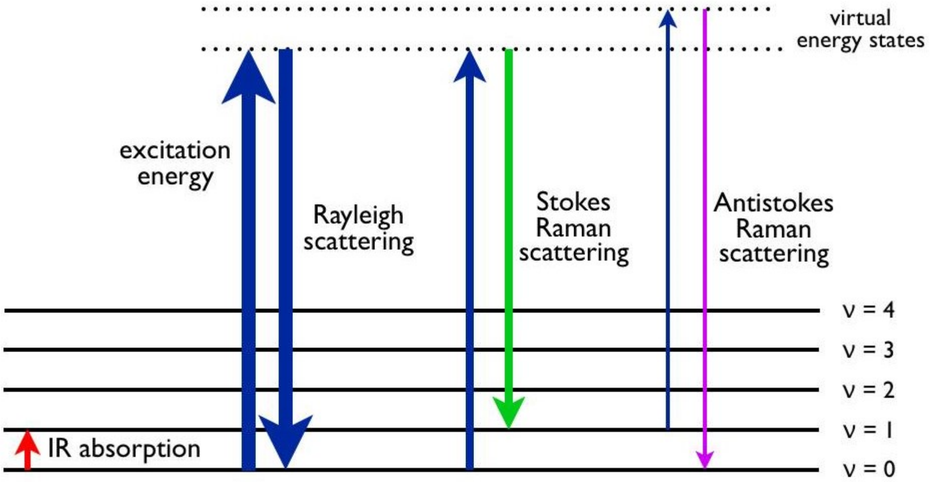

Figure 1.3: Schematic representation of allowed transitions between different vibrational energetic levels.

If the relaxation process leads the molecule in a vibrational excited state, the emitted photon has an energy $h(\nu - \nu_{vib}) < h\nu$ (*Stokes photon*) with

---

[24] Usually the natural frequency of a molecule is smaller respect to the vibrational frequency of the incoming field, as a consequence the anelastic features can be very close to the Rayleigh scattering peak in the Raman spectra. Moreover, the Raman peaks have a very low intensity respect the Rayleigh peak because $\alpha_1 << \alpha_0$.

[25] Using the virtual states the quantum description of the process does not involve the violation of the energy conservation law. The relaxation of the system follows immediately the excitation due to the absorption and the energy conservation is ensured.

$h\nu_{vib}$ energy difference between the initial and final vibrational states. On the other hand, if the initial state is an excited state and the final state is the fundamental state, the energy of the riemitted photon (*Anti-Stokes photon*) is higher than the incoming energy and equal to $h(\nu + \nu_{vib})$.

The quantize cross section that describe the Raman effect can be obtained assuming that the interaction between the molecule and the electromagnetic field is a small perturbation of the non-interacting system of molecule and e.m. radiation. Using the *minimal substitution*[26] and assuming that the system is not perturbated when $t \to \pm\infty$, the unperturbated Hamiltonian is equal to

$$\hat{H}_0 = \hat{H}_{rad} + \hat{H}_{mol}$$

where the molecular Hamiltonian is

$$\hat{H}_{mol} = \sum_i \frac{\mathbf{p}_i}{2m_i} + \phi(\{\mathbf{r}_i\})$$

and the Hamiltonian of the quantized electromagnetic field is describe by the equation 1.11 with the sum extended to all the possible polarizations of the photon. The diffusion process is described through the absorption of an incoming photon $(\mathbf{k}, \hat{\epsilon})$ with energy $\hbar\omega$ and the emission of a photon $(\mathbf{k}', \hat{\epsilon}')$ with energy $\hbar\omega'$. The molecule-field interaction Hamiltonian is described by the equation 1.13.

Now, by defining

$$\hat{H}_{int,1} = \sum_i \frac{q_i}{m_i c} \mathbf{p}_i \cdot \mathbf{A}_i$$

and

$$\hat{H}_{int,2} = \sum_i \frac{q_i}{2m_i c^2} \mathbf{A}_i^2$$

the interaction Hamiltonian is $\hat{H}_{int} = \hat{H}_{int,1} + \hat{H}_{int,2}$ with the potential vector operator

$$\mathbf{A}_i = \sum_{\mathbf{k},s} \sqrt{\frac{2\pi\hbar c^2}{\mathcal{V}\omega_{\mathbf{k}}}} (a_{\mathbf{k}s} e^{i\mathbf{k}\cdot\mathbf{r}} + a^{\dagger}_{\mathbf{k}s} e^{-i\mathbf{k}\cdot\mathbf{r}})$$

The initial and final states at $t \to \pm\infty$ are eingestates of the unperturbed Hamiltonian

$$\hat{H}_0 |i\rangle = E_i |i\rangle$$

---

[26] The "minimal substitution", used in the QFT (*Quantum Field Theory*) and in every book about the classical limit of relativistic equations, allows the introduction of the magnetic potential into the equation (*Schrödinger/Dirac/Klein-Gordon*) through:

$$\hat{p}^2 \to (\hat{p} - e\hat{A})^2$$

this is an approximation for small electromagnetic fields (or at least not strongly coupled).

$$\hat{H}_0|f\rangle = E_f|f\rangle$$

where the states $|i\rangle$ and $|f\rangle$ are the *tensor product* between the molecular system and e.m. field eingestates[27]:

$$|i\rangle = |1_{\mathbf{k}s}, 0_{\mathbf{k}'s'}\rangle|A\rangle$$

$$|f\rangle = |0_{\mathbf{k}s}, 1_{\mathbf{k}'s'}\rangle|B\rangle$$

Thus

$$E_i = E_A + \hbar\omega \quad ; \quad E_f = E_B + \hbar\omega'$$

As seen in the subsection above, the transition probability from the initial state $|i\rangle$ to the final state $|f\rangle$ is given by the *Fermi golden rule*[28]

$$W_{fi} = \frac{2\pi}{\hbar}|\langle f|\hat{H}|i\rangle|^2\delta(E_f - E_i) \tag{1.19}$$

where

$$\langle f|\hat{S}|i\rangle = \delta_{fi} + \langle f|\hat{H}_{int}|i\rangle + \sum_{l\neq i}\frac{\langle f|\hat{H}_{int}|l\rangle\langle l|\hat{H}_{int}|i\rangle}{E_i - E_l} + ...$$

The vector potential is a linear operator in the creation and destruction operators. Thus, when $\mathbf{A}$ is applied to an eingestate of the e.m. field, the result is a linear combination of states. These states can have only a single unit of a single occupation number $n_{\mathbf{k},s}$ that is different with respect the initial state. This means that in the diffusion process the matrix element

---

[27] The eingestates of molecule and field Hamiltonians are defined by the following relations:

$$\hat{H}_{mol}|A\rangle = E_A|A\rangle \quad ; \quad \hat{H}_{mol}|B\rangle = E_B|B\rangle$$
$$\hat{H}_{rad}|1_{\mathbf{k}s}, 0_{\mathbf{k}'s'}\rangle = \hbar\omega|1_{\mathbf{k}s}, 0_{\mathbf{k}'s'}\rangle \quad ; \quad \hat{H}_{rad}|0_{\mathbf{k}s}, 1_{\mathbf{k}'s'}\rangle = \hbar\omega|0_{\mathbf{k}s}, 1_{\mathbf{k}'s'}\rangle.$$

[28] As well-known, according to the Fermi golden rule the “one-to-many” transition probability per unit of time from the state $|i\rangle$ to a set of final states $|f\rangle$ is given, considering only the first order in the perturbation theory, by

$$W_{fi} \propto |\langle f|\hat{H}'|i\rangle|^2$$

where ρ is the density of final states (*i.e.* the number of continuum states per unit of energy) and $\langle f|\hat{H}'|i\rangle$ is the transition matrix element of the perturbation $\hat{H}'$ between the final and initial states. In general the Fermi golden rule can be applied to all the experiments in which the time of the measurement is much larger than the time needed for the transition.

associated to $\mathbf{A}$ is equal to zero because the initial and the final states are characterized by $n_{\mathbf{k}s}$ and $n_{\mathbf{k}'s'}$, respectively.

Now, the operator $\mathbf{A}^2$ is defined by

$$\mathbf{A}_i^2 = \frac{2\pi\hbar c^2}{\mathcal{V}} \sum_{\mathbf{k},s;\mathbf{k}',s'} \frac{1}{\sqrt{\omega_{\mathbf{k}}\omega_{\mathbf{k}'}}} (a_{\mathbf{k}'s'} a_{\mathbf{k}s} e^{i(\mathbf{k}+\mathbf{k}')\cdot\mathbf{r}_i} + a^\dagger_{\mathbf{k}'s'} a^\dagger_{\mathbf{k}s} e^{-i(\mathbf{k}+\mathbf{k}')\cdot\mathbf{r}_i} +$$

$$+ a_{\mathbf{k}'s'} a^\dagger_{\mathbf{k}s} e^{i(\mathbf{k}+\mathbf{k}')\cdot\mathbf{r}_i} + a^\dagger_{\mathbf{k}'s'} a_{\mathbf{k}s} e^{-i(\mathbf{k}+\mathbf{k}')\cdot\mathbf{r}_i}) \hat{\epsilon}^*_{\mathbf{k}'s'} \cdot \hat{\epsilon}_{\mathbf{k}s} \tag{1.20}$$

that gives transition matrix elements different from zero in the diffusion process.

Thus the transition matrix associated to the diffusion process is given by[29]

$$\langle f|\hat{H}_{int}|i\rangle = K^{(1)}(\mathbf{A}_i^2) + K^{(2)}(\mathbf{A}_i)$$

where

$$K^{(1)}(\mathbf{A}_i^2) = \langle f| \sum_i \frac{q_i^2}{2m_i c^2} \mathbf{A}_i^2 |i\rangle$$

and

$$K^{(2)}(\mathbf{A}_i) = \sum_{l\neq i} \frac{\langle f| \sum_i \frac{q_i}{m_i c} \mathbf{p}_i \cdot \mathbf{A}_i |l\rangle\langle l| \sum_i \frac{q_i}{m_i c} \mathbf{p}_i \cdot \mathbf{A}_i |i\rangle}{E_i - E_l}$$

Now, using the dipole approximation and the equation 1.20

$$K^{(1)}(\mathbf{A}_i^2) = \frac{\pi\hbar}{\mathcal{V}} \frac{1}{\sqrt{\omega_{\mathbf{k}}\omega_{\mathbf{k}'}}} \hat{\epsilon}^*_{\mathbf{k}'s'} \cdot \hat{\epsilon}_{\mathbf{k}s} \times$$

$$\sum_i \frac{q_i^2}{m_i} \langle B| \langle 0_{\mathbf{k}s}, 1_{\mathbf{k}'s'}| (a_{\mathbf{k}s} a^\dagger_{\mathbf{k}'s'} + a^\dagger_{\mathbf{k}'s'} a_{\mathbf{k}s}) e^{-i(\mathbf{k}-\mathbf{k}')\cdot\mathbf{r}_i} |1_{\mathbf{k}s}, 0_{\mathbf{k}'s'}\rangle |A\rangle$$

$$= \frac{\pi\hbar}{\mathcal{V}} \frac{1}{\sqrt{\omega_{\mathbf{k}}\omega_{\mathbf{k}'}}} \hat{\epsilon}^*_{\mathbf{k}'s'} \cdot \hat{\epsilon}_{\mathbf{k}s} \delta_{BA} \sum_i \frac{q_i^2}{m_i}$$

thus $K^{(1)}(\mathbf{A}_i^2) = 0$ if $|A\rangle \neq |B\rangle$ (Raman scattering).

Concerning the term $K^{(2)}(\mathbf{A}_i)$, the intermediate state $|l\rangle$ must be expressed as

$$|l\rangle = |0_{\mathbf{k}s}, 0_{\mathbf{k}'s'}\rangle |I\rangle$$

or

$$|l\rangle = |1_{\mathbf{k}s}, 1_{\mathbf{k}'s'}\rangle |I\rangle$$

---

[29] The diffusion process is described by a second order interaction term $K^{(1)}(\mathbf{A}_i^2)$ and a first order interaction term $K^{(2)}(\mathbf{A}_i)$, that is a second order term in the perturbation theory.

to give contribution different from zero (with $|I\rangle$ molecule intermediate state). As a consequence

$$K^{(2)}(\mathbf{A}_i) = \sum_i \frac{\langle B|\langle 0_{\mathbf{k}s}, 1_{\mathbf{k}'s'}|\hat{H}_{int,1}|0_{\mathbf{k}s}, 0_{\mathbf{k}'s'}\rangle|I\rangle\langle I|\langle 0_{\mathbf{k}s}, 0_{\mathbf{k}'s'}|\hat{H}_{int,1}|1_{\mathbf{k}s}, 0_{\mathbf{k}'s'}\rangle|A\rangle}{E_A + \hbar\omega - E_I} +$$

$$+\frac{\langle B|\langle 0_{\mathbf{k}s}, 1_{\mathbf{k}'s'}|\hat{H}_{int,1}|1_{\mathbf{k}s}, 1_{\mathbf{k}'s'}\rangle|I\rangle\langle I|\langle 1_{\mathbf{k}s}, 1_{\mathbf{k}'s'}|\hat{H}_{int,1}|1_{\mathbf{k}s}, 0_{\mathbf{k}'s'}\rangle|A\rangle}{E_A - E_I - \hbar\omega'}$$

that becomes (by applying the definition of $\hat{H}_{int,1}$)

$$K^{(2)}(\mathbf{A}_i) = \frac{2\pi\hbar\sqrt{\omega_{\mathbf{k}}\omega_{\mathbf{k}'}}}{\mathcal{V}}\hat{\epsilon}_{\mathbf{k}'s'} \cdot \mathbf{P}_{BA} \cdot \hat{\epsilon}_{\mathbf{k}s}$$

where $\mathbf{P}_{BA}$ is the *polarizability tensor*

$$\mathbf{P}_{BA} = \sum_I \frac{\boldsymbol{\mu}_{BI}\boldsymbol{\mu}_{IA}}{E_A + \hbar\omega - E_I} + \frac{\boldsymbol{\mu}_{IA}\boldsymbol{\mu}_{BI}}{E_A - E_I - \hbar\omega'} \qquad (1.21)$$

and $\boldsymbol{\mu}$ is the *dipole momentum operator*

$$\boldsymbol{\mu} = \sum_i q_i \cdot \mathbf{r}_i$$

Thus, from the equation 1.19, the transition probability per time unit is

$$W_{fi} = \frac{(2\pi)^3\hbar}{\mathcal{V}^2}\omega_{\mathbf{k}}\omega_{\mathbf{k}'}|\hat{\epsilon}_{\mathbf{k}'s'} \cdot \mathbf{P}_{BA} \cdot \hat{\epsilon}_{\mathbf{k}s}|^2\delta(E_f - E_i)$$

Now, by defining the density of the photon final states and the incident flux as, respectively

$$\rho(\mathbf{k}')d\mathbf{k}' = \frac{\mathcal{V}}{(2\pi)^3}\mathbf{k}'^2 d\mathbf{k}' d\Omega$$

$$\Phi_{inc} = \frac{c}{\mathcal{V}}$$

the cross section that describe the diffusion of a photon with a wavevector between $\mathbf{k}'$ and $\mathbf{k}' + \Delta\mathbf{k}'$ is given by

$$d\sigma = \frac{W_{fi}\rho(\mathbf{k}')d\mathbf{k}'}{\Phi_{inc}} = \hbar c\mathbf{k}\mathbf{k}'|\hat{\epsilon}_{\mathbf{k}'s'} \cdot \mathbf{P}_{BA} \cdot \hat{\epsilon}_{\mathbf{k}s}|^2\delta(E_f - E_i)d\mathbf{k}'d\Omega$$

and the *differential cross section* is equal to

$$\frac{d^2\sigma}{d\Omega dE} = \mathbf{k}\mathbf{k}'^3|\hat{\epsilon}_{\mathbf{k}'s'} \cdot \mathbf{P}_{BA} \cdot \hat{\epsilon}_{\mathbf{k}s}|^2\delta(E_f - E_i)$$

Finally, considering the sum over all the molecular states, the energy conservation[30] and a *Boltzmann probability distribution*[31] for the initial states

$$P(A) = \frac{e^{\frac{-E_A}{k_B T}}}{\sum_I e^{\frac{-E_I}{k_B T}}}$$

the cross section for the Raman scattering is

$$\frac{d^2\sigma}{d\Omega dE} = \mathbf{k}\mathbf{k}'^3 \sum_A P(A) \sum_B |\hat{\epsilon}_{\mathbf{k}'s'} \cdot \mathbf{P}_{BA} \cdot \hat{\epsilon}_{\mathbf{k}s}|^2 \delta(E_A - E_B - \hbar\Delta\omega) \qquad (1.22)$$

The expression 1.22 doesn't depend on the molecular states involved in the process. The Raman cross section is proportional to the fourth power of k and is related to the polarizability of the system. Thus the selection rules for the Raman effect are determined by the polarizability tensor as a function of the polarization of the incoming and collected radiation.

The theory here presented describes the diffusion process associated to a molecular system, however this theory can be easily applied to crystalline solids, taking into account the symmetry rules and the *Bloch theorem*, which imposes the reticular periodicity to all the excitations within a solid and therefore also to the collective vibrational modes responsible for the Raman scattering.

1.4 Surface Enhanced Raman Scattering

The SERS (*Surface Enhanced Raman Scattering*) phenomenon was detected for the first time in 1974 [26]. The main aim of the Raman experiments in those years was the development of new kinds of experimental techniques to measure the Raman signal of a single molecules layer adsorbed onto a well suited substrate, *i.e.* using a rough surface to increase the number of molecules lighted up by the radiation. However the Raman signal collected by Fleischmann et al., related to a pyridine monolayer adsorbed on a silver electrode, was higher (many orders of magnitude) than expected [27]. In the next years new experiments [28, 29, 30] demonstrate that the Raman spectrum enhancement was due to the coupling between the incident radiation and the sample and related to the substrate nature and morphology.

---

[30] The energy conservation is assured assuming that $E_B - E_A = \hbar(\omega - \omega')$.

[31] The Boltzmann distribution for the states population clarifies the intensity difference between Stokes and Anti-Stokes transitions at "finite temperature". Indeed, according to Boltzmann, at room temperature, the more populated states are those with lower energies, thus the Stokes transitions (where the energy of the initial state of the molecule is lower than the energy of the final state) are preferred.

In general the SERS phenomenon is due to a superposition of two different enhancement mechanisms. The most relevant contribution is the *electromagnetic enhancement* [31, 32], associated to the resonance between incident photons and collective excitations of the electrons gas in the metallic substrate[32]. Therefore, in a SERS experiment, the presence of a metallic rough substrate is mandatory. However the order of magnitude of the SERS enhancement (up to $10^9 - 10^{10}$ range) cannot be fully explained using only the electromagnetic mechanism (enhancement up to 10^6). The second contribution to the SERS effect is the so-called *chemical enhancement* related to changes in the electric charge distribution of the molecule due to the interaction with the metallic surface [33, 34].

1.4.1 The electromagnetic enhancement

When an electromagnetic wave interacts with a metallic surface, the fields at the surface are different than those observed in the far field. If the surface is rough, the wave may excite localized surface plasmons on the surface, resulting in amplification of the electromagnetic fields near the surface.

The amplification is due to the *Localized Surface Plasmon Resonance* (LSPR) that occurs when the collective oscillation of valence electrons in a metallic nanoparticle is in resonance with the frequency of incident light (see figure 1.4).

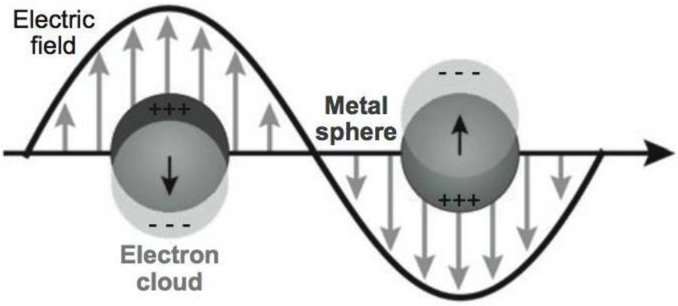

Figure 1.4: Plasmonic resonance effect on a metallic nanoparticle.

The electromagnetic enhancement related to the resonance between the incoming e.m. field and the surface plasmons of the metallic substrate occurs when the material has a high electronic mobility, as in the case of noble metal

---

[32] This collective excitation are the so-called *surface plasmons*. The plasmon is the coherent longitudinal oscillation quantum of the free electrons inside a solid system respect the positive ions of the crystalline reticulum. Thus the surface plasmon represents the coherent oscillation of the free surface electrons in a solid.

surfaces (*e.g.* Au and Ag nanoparticles). The electromagnetic enhancement associated to an incoming e.m. field that interacts with a molecule adsorbed on a metallic spherical particle can be described through the *average Raman enhancement factor*[33] g [35].

Thus the average amplitude of the field irradiated by the particle is

$$E_s = gE_0$$

where E_0 is the amplitude of the incoming field and E_s is the "local average" of the field amplitude[34] in the *near field* region. And the amplitude of the scattered field given by the Raman effect is

$$E_R \propto \alpha_R E_s \propto \alpha_R g E_0$$

with α_R appropriate components combination of the polarizability tensor. A further enhancement of the scattered field is due to the diffusion of the field E_R at frequency $\omega_R = \omega_0 \pm \omega_{phonon}$ by the metallic particle[35], with an enhancement factor[36] g' (as shown in figure 1.5).

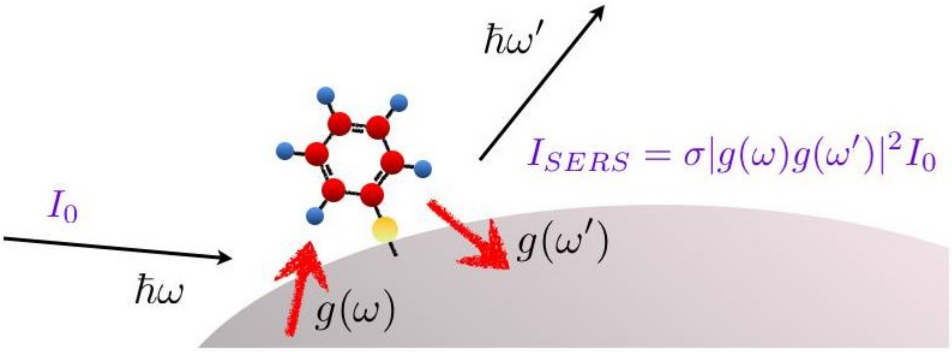

Figure 1.5: Mechanism of electromagnetic enhancement in SERS.

---

[33] This factor can be described as a function of the *dielectric costants* of metallic nanoparticle and environment:

$$g = \frac{\epsilon_{in} - \epsilon_{out}}{(\epsilon_{in} + 2\epsilon_{out})}$$

where ϵ_{in} is the dielectric constant of the nanoparticle and ϵ_{out} is the dielectric constant of the external environment.

[34] E_s is the field amplitude that excites the molecules adsorbed on the metallic surface during a SERS experiment.

[35] In condensed-matter physics a *phohon* is the unit of vibrational energy that arises from oscillating atoms within a crystal.

[36] This factor is different from g, because of the dependence between the plasmonic resonance and the frequency, thus the enhancement factor is different for ω_0 and ω_R.

As a consequence the scattered field associated to the SERS effect is given by

$$E_{SERS} \propto \alpha_R g g' E_0$$

and

$$I_{SERS} \propto |\alpha_R|^2 |gg'|^2 I_0$$

If the *Raman shift* from the excitation frequency is small $g' \simeq g$, the SERS intensity is proportional to $|g|^4$. In the case of high frequency SERS bands or more complicated systems, the intensity is proportional to the third power of the enhancement factor g. In first approximation the electromagnetic enhancement can be estimated through the *enhancement factor* EF:

$$EF = \frac{|E_s|^2 |E_R|^2}{|E_0|^4} = 4|g^2||g'|^2$$

this expression is known as the *theoretical SERS electromagnetic mechanism enhancement factor* [36].

It is noteworthy that the SERS effect is due to the presence of metallic particles and depends strongly by the shape and dimensions of this particles.

A more detailed discussion of the resonance phenomenon between the incoming radiation and the localized surface plasmons of metallic spherical particles is reported in [37, 38, 39].

Now, the polarizability α_R is the polarizability of the molecule-metal system. In general $\alpha_R \neq \alpha_0$, where α_0 is the polarizability of the isolated molecule. This means that the selection rules and the characteristic peaks frequency for the Raman scattering can be modified by the SERS effect, in particular in case of *charge transfer* between molecule and metal. This mechanism is related to the chemical enhancement that can be observed during SERS experiments.

For complex metallic systems, like nanoparticles aggregates, the coupling of the plasmonic resonance between nearby metallic structures ($\sim 10nm$) cannot be neglected [40]. This coupling depends strongly by the particle distance, as shown in figure 1.6.

1.4.2 The chemical enhancement

Another mechanism responsible for the SERS ehancement is the charge transfer (or chemical) mechanism that depends on the chemical nature of metal and molecule and is due to the presence of a chemical bond between the

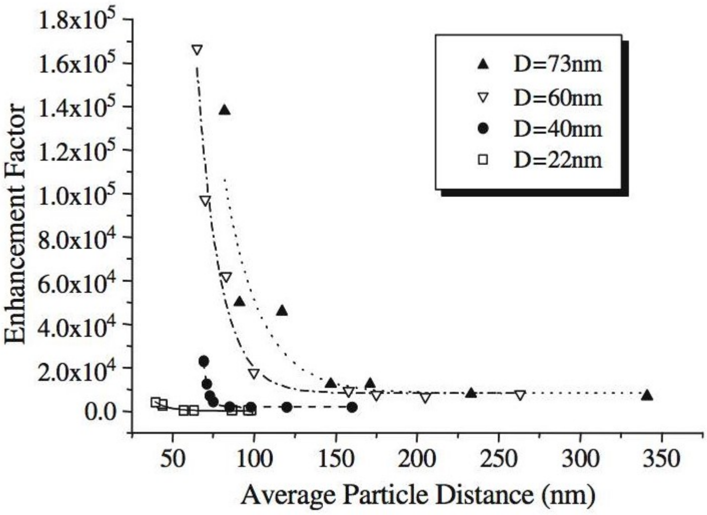

Figure 1.6: SERS enhancement factor for a homogeneous gold nanoparticles system as a function of the average particle distance, with different nanoparticles dimensions [41].

metallic substrate and the adsorbed molecule[37]. The main effect of the charge transfer mechanism is the band broadening and the shift of the characteristic frequency of the electronic levels in the Raman spectrum of the adsorbed molecule [42].

Assuming that the HOMO (*Higher Occupied Molecular Orbital*) and LUMO (*Lowest Unoccupied Molecular Orbital*) orbitals of the adsorbed molecule are symmetrical (concerning the energy) respect the Fermi level of the metal, the incoming photon ($\hbar\omega_L$) excites an electron from the conduction band of the metal, near to the Fermi level, to an excited energy level. The orbitals hybridization due to the metal-molecule interaction allows the excitation of the electron to a new vibrational level E_{CT} in the LUMO orbital. Another electron from the HOMO orbital can fill the hole in the Fermi level through the absorption of another photon with energy $\hbar\omega_L$. During the vibronic de-excitation, the first electron comes back to the HOMO from the level E_{CT} and a “Raman photon” with energy $\hbar(\omega_L - \omega_{vib})$ is emitted (as shown in figure 1.7).

Thus the chemical enhancement is due to a new resonance condition between the incoming radiation and the gap $|E_{Fermi} - E_{CT}|$. The broadening of

---

[37] The SERS enhancement is mainly due to the electromagnetic mechanism, however the charge transfer between molecule and substrate can contribute with an enhancement around $10 - 10^3$.

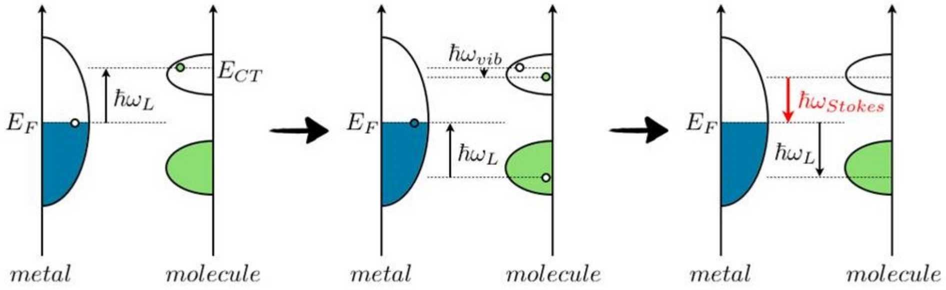

Figure 1.7: Mechanism of charge transfer enhancement in SERS.

the bands is related to the recombination energy between electron and hole that is different from the energy of a Raman emission.

Chapter 2

SR-XPS and SERS techniques

2.1 XPS spectroscopy

X-rays were discovered in November 1895 and less that twenty years later the first diffraction and spectroscopy experiments were done. Since then, X-rays have become an invaluable tool for investigating microscopic properties of matter.

The *PhotoElectron Spectroscopy* (PES) is an old experimental technique and has its origins in the investigations of the photoelectric effect using X-rays as the exciting photon source. The phenomenon of photoemission was detected by Hertz [43] in 1887 (see figure 2.1), in the following years his experiments were refined [44, 45] and in 1905 Einstein was able to explain their systematics by invoking the quantum nature of light [46].

The XPS (*X-ray Photoelectron Spectroscopy*) technique has been used only in the last forty years as a powerful method to study the electronic structure of atoms, molecules, solids and surfaces, based on high-resolution analysis of energy and direction of photoemitted electrons [47, 48, 49]. This delay is related to the development of *ultra-high vacuum* techniques and high resolution detectors and analyzers. It is noteworthy that the most important advancements have been originated by the availability of the new *synchrotron light sources.*

2.1.1 XPS technique: fundamental aspects

Figure 2.2 exhibits the ingredients of a modern *Photo Emission* (PE) experiment. The light source is either a gas-discharge lamp, an X-ray tube, or a synchrotron-radiation source. The incoming light, described by the vector potential **A**, impinges on the sample, which can be a gas as well as the surface of a solid, and the electrons excited by the photoelectric effect are

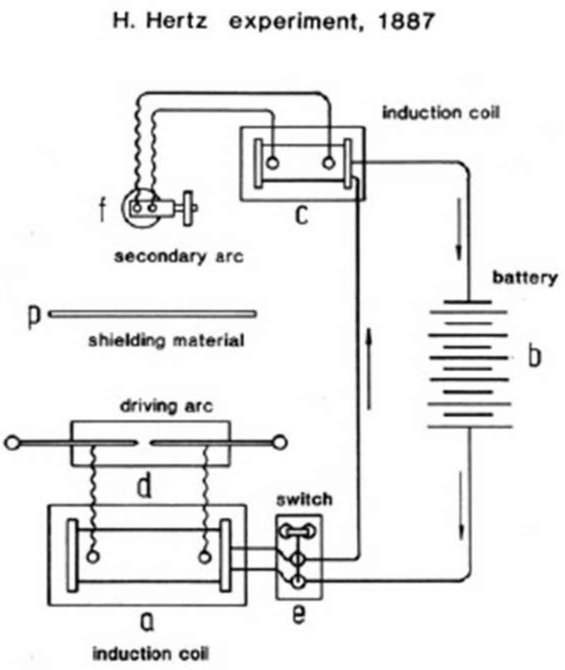

Figure 2.1: Experimental arrangement used by Hertz for his “discovery” of the photoelectric effect. An arc *d* emits light that can stimulate a second arc *j* ; *a* and *c* are coils that produce the voltages for the arcs. A switch *e* is used to activate the coils from the battery *b*, *p* indicates shielding material that was placed between arcs *d* and *j*.

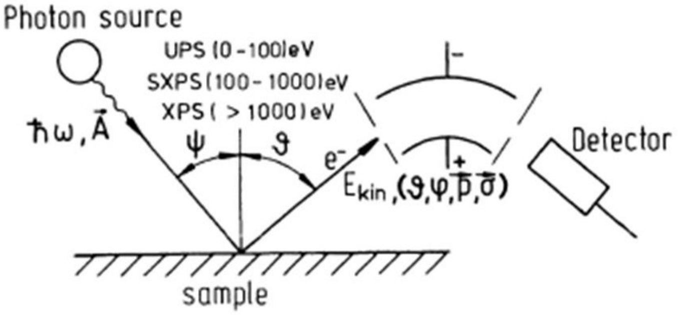

Figure 2.2: Schematic representation of a modern PES experimental setup. The light source can be a UV discharge lamp, an X-ray tube or a storage ring. The electrons are detected by an electrostatic analyzer.

then analyzed with respect to their kinetic energy E_{kin} and their momentum p. The polarization of the light is a useful property in an angle-resolved PE experiment. The important parameters to be measured are then the kinetic energy E_{kin} of the photoemitted electron, and its angle with respect to the impinging light $(\psi + \vartheta)$ and the surface (ϑ, φ). Knowing the energy of the light and the *work function*[1] of the system, it's possible to determine the *binding energy*[2] (BE) of the electrons in the sample from the following equation:

$$E_{kin} = \hbar\nu - \phi - |BE| \tag{2.1}$$

The momentum p of the outgoing electron is determined from its kinetic energy by

$$E_{kin} = \frac{p^2}{2m},$$
$$p = \sqrt{2mE_{kin}}$$

The direction of $p/\hbar$ is obtained from ϑ and φ which are the polar and azimuth angles respectively under which the electrons leave the surface.

In general the measured photoemitted electron current J_e is a function of many variables $J_e = f(h\nu, \epsilon, \theta, \phi; E_{kin}, \sigma, \theta_e, \phi_e)$, as shown in figure 2.3.

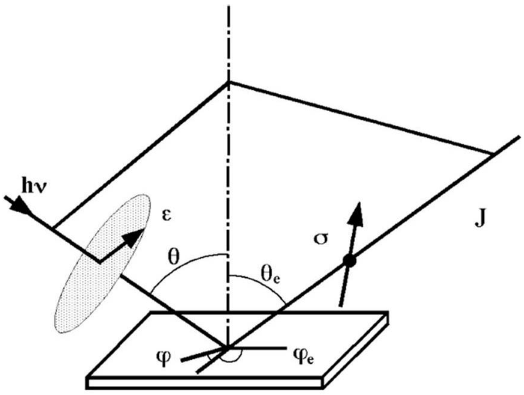

Figure 2.3: Schematic diagram of the photocurrent J_e with all the variables involved in a PE experiment.

In the EDC method, the current J_e is measured as a function of the photoelectron energy E_e while keeping the other variables fixed. J_e is directly

---

[1] The photoelectric work function corresponds to the minimum energy required to eject an electron from the solid surface, it depends from the system and the experimental setup of the PE experiment.

[2] The electron binding energy, also called *ionization potential*, is the energy required to remove an electron from an atom, a molecule, or an ion.

linked to the photoionization microscopic cross-section through the relation

$$J_e = \int_{\Delta\Omega} d\Omega \int_{\Delta E_e} dE_e I \rho_A \left(\frac{d\sigma}{d\Omega dE_e} \right) K_s$$

where $\Delta\Omega$ and ΔE_e are the electron spectrometer angle and energy acceptances, respectively, I is the incoming photon current, ρ_A is the sample areal density, K_s is the spectrometer efficiency and $\left(\frac{d\sigma}{d\Omega dE_e}\right)$ is the photoionization differential cross section.

The typical energy range of the photoemitted electrons is $5 \div 1500$ eV and their *escape depth*[3] is limited between few and few tens of Å (see figure 2.4).

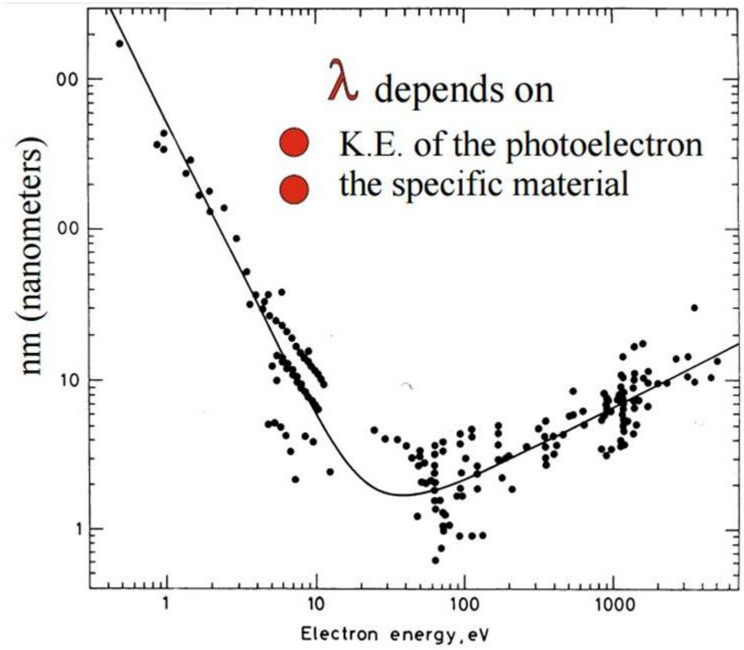

Figure 2.4: Electron mean free path for different materials as a function of the electron kinetic energy.

It is noteworthy that the strong interaction of electrons with matter affects the probability distributions of photoelectrons, thus is mandatory to perform PES experiments under vacuum (at least 10^{-7} mbar) to avoid the interaction with the background atmosphere surrounding the sample.

---

[3] The escape depth, that is directly proportional to the *mean free path* λ, determines the depth from which photoemitted electrons escape from the solid into vacuum without loosing energy. The escape depth minimum value, corresponding to the maximum surface sensitivity, lies in the $10 \div 50$ eV range.

Now, to highlight the information contained in the photoelectron current, is useful to consider the simplest many electron quantum system, *i.e.* the He atom. To achieve photoionization of He, one of the two electrons, bounded to the doubly charged nucleus, must be promoted to the continuum. Thus, the photoelectron spectrum measured should consist of a single peak (*main* or *adiabatic peak*) at the photoelectron energy $E_e = h\nu - BE_{1s}(24.6eV)$.

However, photoemission peaks appear in the He XPS spectrum labeled as n=2,3,... and a continuum distribution extending above the He^{++} threshold energy (as shown in figure 2.5). These so called *satellite structures* are related to the many-body properties of the systems and are observed for all the rare gases, becoming more relevant as the atomic number increases[4].

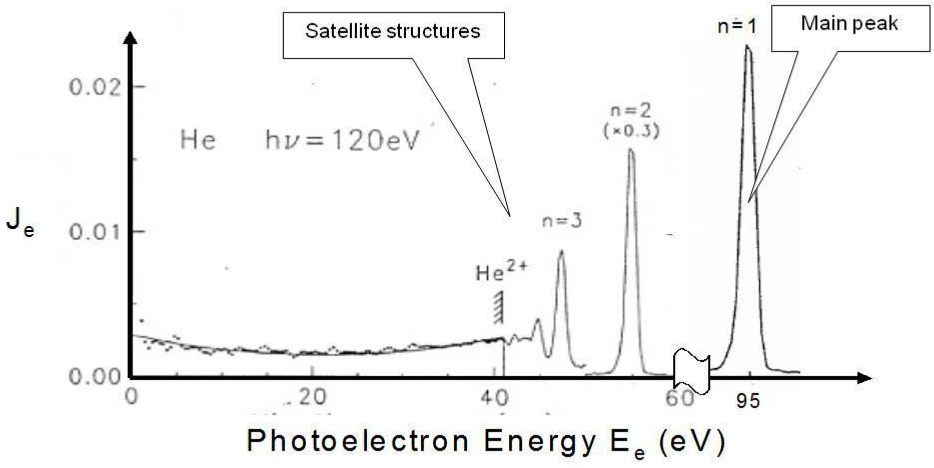

Figure 2.5: High resolution XPS spectrum of helium. The main peak, labeled n=1 (principal quantum number), corresponds to the transition $h\nu + He(1s^2) \rightarrow He^+(1s^1) + \epsilon_{l=1}$ promoting one electron from the initial state ($n = 1$, $l = 0$, $m = 0$, $s = \pm 1/2$) to the continuum [50].

Satellite structures

The manifold of discrete transitions at larger BE followed by a continuum above the double ionization threshold in the XPS spectrum is due to the presence of many possible final ionic states associated with removal of an identical single particle spin orbital (see figure 2.6). This manifold of different final states implies excitation of further electron(s) of the sample both

---

[4] The photoelectron spectrum becomes more and more complex for samples of increased complexity (*e.g.* heavy atoms, molecules, clusters, solids and so on).

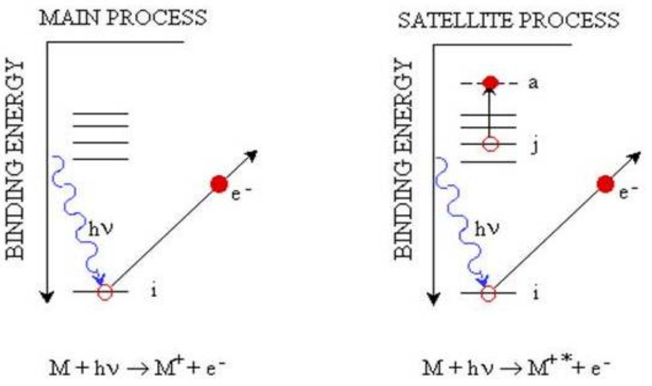

(a) Primary photoionization processes

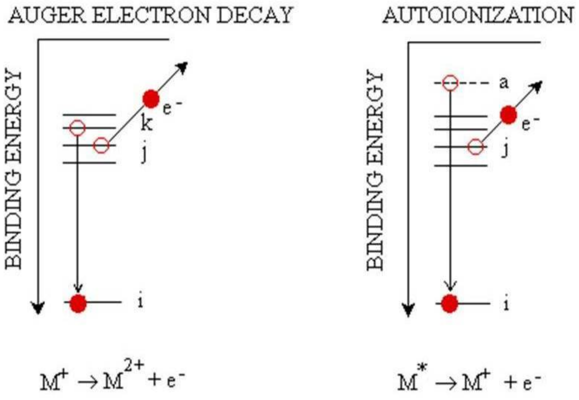

(b) Secondary processes

Figure 2.6: In figure are shown the mechanisms responsible for generation of the main peak and satellite structures (a) and the secondary processes after the ionization of the system (b).

to discrete and continuum empty states (*shake-up* and *shake-off* satellites, respectively).

As seen before, assuming the validity of the Koopman theorem, the Hamiltonians of initial and final states are identical (*i.e.* the atom electronic structure stays frozen under creation of the hole state). However, to explain the satellite structures the condition $H_0 = H_0'$ must be relaxed, thus allowing for a spectrum of many possible final ionic states related to each individual single particle hole state. The richness of satellites structures is directly linked to the degree of electron correlation that affects the initial bound state involved in the photoionization process.

Spin-orbit splitting

Another interesting feature in the XPS spectrum, besides the satellites structures, is the splitting of the photoemission peak due to the spin-orbit coupling. Hence, the so called *spin-orbit splitting* is associated to hole states with quantum number l different from zero. As a consequence, holes in p ($l = 1$), d ($l = 2$) and f ($l = 3$) generate doublets of final states characterized by quantum number j (where $j = l + s$) equal to 1/2 - 3/2, 3/2 - 5/2 and 5/2 - 7/2, respectively.

It is noteworthy that the value of spin-orbit splitting and peak area ratios of a core level of an element in different compounds are nearly the same (see figure 2.7), allowing the element identification in the sample.

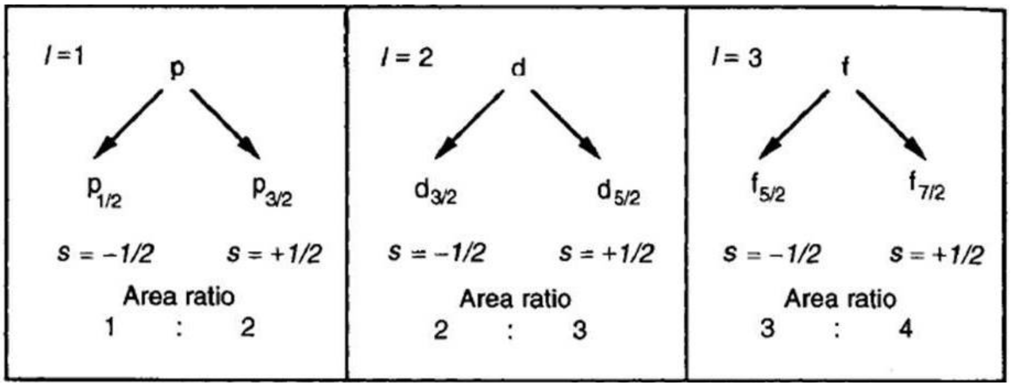

Figure 2.7: Spin-orbit labelling and area ratio for orbitals p, d and f.

Multiplet splitting and vibrational overtones

Considering open shell system, *i.e.*quantum systems in which orbitals are partially occupied, the so called *multiplet splitting* (not ascribable to spin-orbit interaction) is observed. This splitting arises from spin coupling between residual core electrons and valence electrons unpaired spins. The multiplet splittings are common ingredients in *Auger electron spectra*[5], because are related to the core hole relaxation processes[6].

Another phenomenon, that concerns the *molecular photoelectron spectroscopy*, is the splitting due to molecular vibrations (*vibrational overtones*)

---

[5] The Auger effect is a process by which electrons with characteristic energies are ejected from atoms in response to a downward transition by another electron in the atom. Thus, the energy distribution of Auger electrons is independent from the photon and photoelectron energies.

[6] If the final states contain two vacancies, they may couple in several different ways, giving rise to states with different energy.

associated to the generation of ionized molecules in excited vibrational states. The energy resolution of *Ultraviolet Photoelectron Spectroscopy* (UPS) is of about 0.015 eV, sufficient to investigate the vibrational fine structure but not enough to resolve the rotational fine structure. However, the vibrational overtones are not usually clearly visible using XPS (in which the energy resolution is around 1 eV) and thus, can be neglected in the data analysis.

Chemical shift

The precise measurement of core hole BE allows to investigate the electrostatic interaction between photoelectrons and nucleus as well as the electrostatic shielding from all other electrons. Changes in the chemical bonding of an element are related to removal or addition of valence electrons and correspond to changes in the photoelectron BE. The measure of the core hole electron binding energies *chemical shift* provides significant information concerning the chemical environment within which the atom is bound (as shown in figure 2.8).

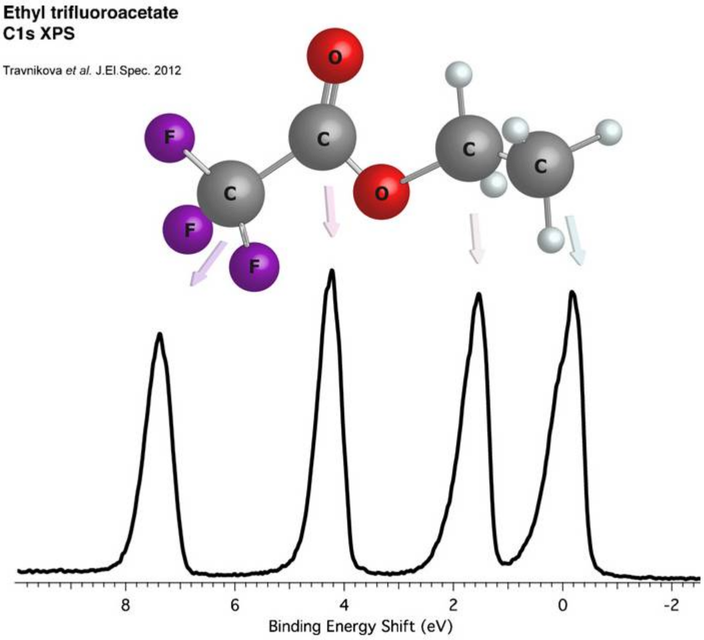

Figure 2.8: The C1s photoelectron spectrum of *ethyl trifluoroacetate* recorded at a photon energy of 340 eV at the PLEIADES beamline at the SOLEIL synchrotron laboratory [51].

Moreover, core energy shift is associated to changes in coordination number of the same atom in a given aggregate (*e.g.* cluster surface atoms experience a different chemical bond from bulk atoms). Thus, the chemical shift is a useful tool to investigate oxidation states, molecular environment, lattice sites and cluster behaviour inside the sample.

Photoelectron angular distributions

Assuming the validity of the *frozen core approximation*[7], the system can be described as formed by N interacting electrons with the N-particle wave function written by a *Slater determinant*[8] of one electron spin-orbitals

$$|\psi_A^{(N)}\rangle = \hat{A}(\phi_j(\vec{r}_j, \sigma_j); \psi_R^{(N-1)})$$

(where $\hat{A}$ is an antisymmetrization operator assuring the validity of the *Pauli principle*[9] and ϕ_j is the jth single particle spin orbital of the initial state).

Furthermore, assuming the aforementioned *sudden approximation*, the photoelectron in the continuum state $|\epsilon_l\rangle$ (with E_e and $\vec{K}_e$) is fully decoupled from the residual N-1 particles ion and the final N-particle state can be expressed as

$$|\psi_B^{(N)}\rangle = \hat{A}(\epsilon_l; |\psi_B^{(N-1)}\rangle)$$

Thus, the photoemission cross section at fixed photon energy and differential in the photoelectron energy and emission angle is equal to

$$\frac{d\sigma}{d\Omega dE_e} \propto \sum_B |\hat{\epsilon} \cdot \langle\epsilon_l|\vec{r}_j|\phi_j(\vec{r}_j, \sigma_j)\rangle\langle\psi_B^{(N-1)}|\psi_R^{(N-1)}\rangle|^2 \cdot \delta(E_e + E_B^{(N-1)} - E_A^N - h\nu) \tag{2.2}$$

Now, starting from the equation 2.2, it can be shown that, for linearly polarized light and for fixed photon and photoelectron energies (that satisfy

---

[7] According to the frozen core approximation, the relaxation of the sample is upon creation of a hole-state and electron-electron correlation are neglected.

[8] In quantum mechanics, to describe the wave function of a multi-fermionic system that satisfies anti-symmetry requirements, a general method consists in using the complete antisymmetry property of determinants. Thus, the Slater determinant is an expression allowing to construct electron wavefunctions which are completely antisymmetric in all cases.

[9] The *Pauli Exclusion Principle* states that, in an atom or molecule, no two electrons can have the same four electronic quantum numbers (as an orbital can contain a maximum of only two electrons, the two electrons must have opposing spins). This principle is part of one of the most basic observations of nature: particles of half-integer spin (*fermions*) must have antisymmetric wavefunctions, and particles of integer spin (*bosons*) must have symmetric wavefunctions.

the energy conservation δ function), the photoemission cross section becomes

$$\frac{d\sigma}{d\Omega} \propto \sum_{B} |\hat{\epsilon} \cdot \langle \epsilon_l | \vec{r}_j | \phi_j(\vec{r}_j, \sigma_j) \rangle \langle \psi_B^{(N-1)} | \psi_R^{(N-1)} \rangle|^2$$

Considering that all molecular and atomic orbitals have a characteristic angular distribution of electrons, the photoelectron current is expected to depend upon direction under which the photoelectron is detected, with respect to polarization vector (see figure 2.9), and characteristics of the single particle orbitals involved, both bound and continuum ones.

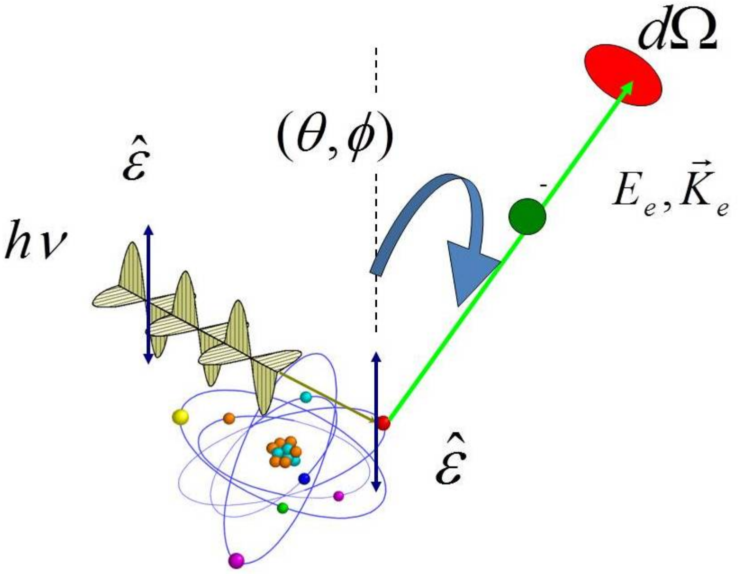

Figure 2.9: Schematics of an angle resolved photoemission experiment (θ and ϕ are polar and azimuthal angles, respectively).

Thus, the measured intensity of all final states in a spectrum will have a certain angular dependence. The angular distribution of the emitted photoelectrons can be described using one single *asymmetry parameter*[10] β [52] (*i.e.* the photoelectrons are symmetrically distribuited about the polarization direction):

$$\frac{d\sigma}{d\Omega} \propto \frac{\sigma}{4\Pi}[1 + \beta P_2 cos(\theta)]$$

with P_2 second order *Legendre polynomial.*

---

[10] This parameter spans from -1 to 2 and depends on the initial and final state orbitals involved in the ionization process.

Looking at figure 2.10, there are four directions in which photocurrents are expected to be independent from β values and correspond to the so called *magic angle*[11] (54.74°).

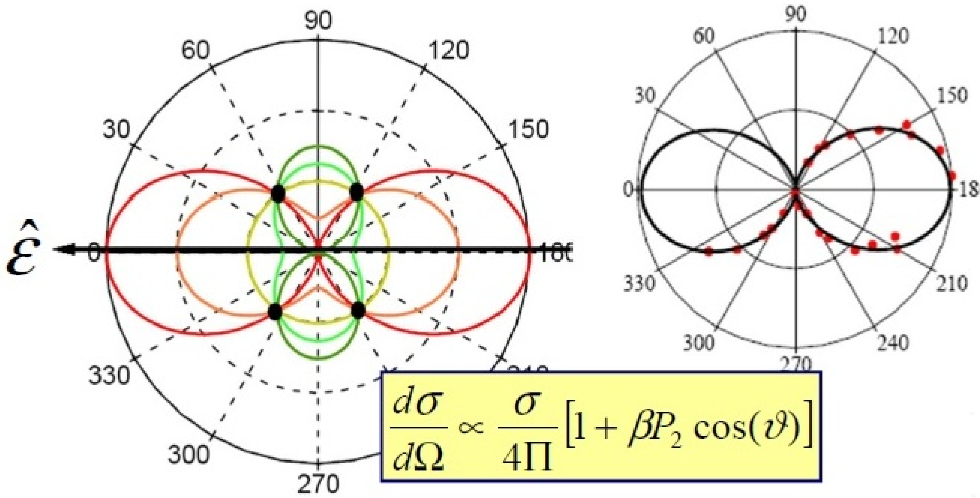

Figure 2.10: Angular distribution of photoionization in polar coordinates experimental (right panel) and calculated (left panel) are reported for selected β values. The polarization vector ϵ is reported as a *black bold arrow*, while magic angle has been indicated by a *black point*. Experimental results are relative to He and the best fit to the data is obtained for $\beta = 2$.

In case of molecules, clusters and solids (*i.e.* the atom from which the photoelectron is generated is surrounded by neighboring ones), the photoelectron wavefunction gets scattered from each individual atom. Thus, the measured photoelectron current is a coherent superposition of source photoelectron wavefunction and point scattered wavefunctions[12].

The photoelectron angular distribution is relevant to highlight fine details of photoionization dynamics and provides the basis for various spectroscopies based on the *photoelectron diffraction*[13].

---

[11] At this angle the photocurrent depends only on the total cross section σ and not on the light polarization neither on the angular momenta of the photoelectron wavefunction or the symmetry of the initial state.

[12] It can be demonstrated that the collected photoelectron current becomes proportional to the square modulus of the coherent sum of the unperturbed and scattered photoelectron wavefunctions.

[13] This technique aims to study the local geometrical order in molecules, clusters and solids, through the investigation of the photoelectron diffraction from surrounding atoms.

The three-step model

In a solid the photoemitted electrons must travel towards the surface and escape into vacuum to be detected by the photoelectron analyzer. During its travel, the photoelectron can undergo extrinsic scattering processes with other electrons and intrinsic processes related to the relaxation of the system. Considering that the escaping photoelectron energy must be equal to the sum of the initial level energy and the photon energy and assuming the conservation of the momentum component parallel to the surface (while $\mathbf{k}_\perp$ is not conserved), this multi-particle process can be described through a *three-step model* [53].

In a solid, the measured spectral photoelectron current (EDC) can be correlated to the spectral density of initial valence band states, considering three independent contribution:

1. a photon with energy $h\nu$ promotes an electron from an initially occupied state to a final state of free-electron out of the crystal;

2. the electron travels through the solid (taking into account also inelastic scattering with other electrons);

3. the photoelectrons overcoming the surface and escaping into the vacuum must have the normal component of their momentum different from zero.

In the first step, the photon promotes an electron from an initially occupied *Bloch state*[14] Φ_i to a final *Bloch state* Φ_f of free-electron out of the crystal, with energy and momentum conservation.

Concerning the transmission of the electron through the bulk solid (second step), the traveling photoelectrons can be grouped into two classes: *primary electrons* which reach the solid surface without encountering any scattering (they keep the physical information from within the crystal) and *secondary electrons* which undergo multiple inelastic scattering, mainly due to electron-electron scattering.

Finally, the *trasmission function* that describes the photoemission process in the solid must take into account that for the primary electrons escaping from the surface, by travelling from the semi-infinite crystal to the vacuum

---

[14] A Bloch function combines a plane wave with a periodic sequence of atomic orbitals:

$$\Phi_{Bloch}(\mathbf{r}, t) = u_k(\mathbf{r}) \cdot e^{[i(\mathbf{k}\cdot\mathbf{r}-\omega t)]}$$

where $u_k(\mathbf{r})$ is a periodic function (for atomic orbitals) and $e^{[i(\mathbf{k}\cdot\mathbf{r}-\omega t)]}$ is a plane wave (for free electrons).

(third step), only the momentum component parallel to the surface is conserved between the internal and external momentum, because of symmetry considerations.

Thus, the photoemission current can be expressed as the product of these three independent contribution A (first step), B (second step) and C (third step): $J_e \propto A \cdot B \cdot C$.

2.1.2 Synchrotron Radiation induced X-Ray Photoelectron Spectroscopy

Relativistic charged particles forced to move along curved trajectories by applied magnetic fields emit electromagnetic radiation called *Synchrotron Radiation* (SR) with peculiar characteristics [54], such as

- high intensity, *brightness*[15] and beam stability;
- natural narrow angular collimation;
- wide spectral range (from infrared to hard X-rays);
- pulsed time structure;
- high degree of polarization.

Thus synchrotron sources are very versatile facilities that can be actually used for many research domains. In particular, synchrotron radiation induced spectroscopy is one of the most powerful tools for investigating the properties of matter in many different fields (like molecular and atomic physics, cell biology, medical applications, environmental science, nanotechnology, catalysis and cultural heritage). Nowadays there are many SR implants (among them *Elettra Sincrotrone Trieste* in Italy, see figure 2.11) dedicated to exploit the special characteristics of the generated light to continuously improve the brightness, the tunability and the collimation of the synchrotron radiation.

Thanks to the peculiar properties of synchrotron sources the SR-XPS (*Synchrotron Radiation induced X-ray Photoelectron Spectroscopy*) technique shows many advantages respect the conventional XPS, such as improvement in surface sensitivity, higher number of photons per bandwidht, faster measurements and in general a better quality of the spectra (see figure 2.12).

---

[15] The brightness is equal to the number of photons per second and per unit source size and divergence in a given bandwidth.

Figure 2.11: Elettra Synchrotron Facility.

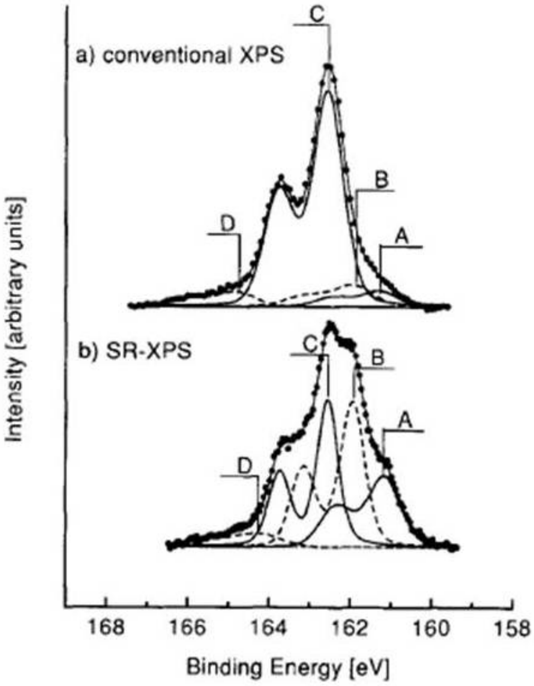

Figure 2.12: Sulphur 2p photoelectron spectra measured with conventional XPS using AlK$_\alpha$ (1486.6 eV) excitation (a) and with SR excitation at energy 209 eV (b) [55].

2.2 Surface-Enhanced Raman Spectroscopy

The ability to control size, shape, and chemical composition of a surface has been the key for the development of the surface-enhanced Raman spectroscopy. As seen before, the excitation of the LSPR of a nanostructured surface or nanoparticle lies at the heart of SERS (electromagnetic enhancement). As a consequence, the ability to reliably control the surface characteristics has taken SERS from an interesting surface phenomenon to a rapidly developing analytical tool for the sensitive and selective detection of molecules adsorbed on noble metal nanostructures. In particular SERS has great potential for chemical and biological sensing applications because it is selective and sensitive and gives little interference from water.

2.2.1 Raman spectroscopy

The diffusion process is a second order process in the matter-radiation interaction, thus the transition matrix element related to absorption and emission processes usually is higher than the one related to the Raman effect[16]. As a consequence, in a classical Raman spectroscopy experiment (the typical experimental setup is shown in figure 2.13), the system is excited using an electromagnetic radiation in the spectral range of visible light.

The Raman signature clearly identifies molecules and a careful data analysis can lead to the assignment of main peaks to molecular vibrational modes.

The Raman spectroscopy, as well as the *Infrared spectroscopy*, studies the fundamental vibrations of molecules. However, in contrast to IR-spectroscopy, no absorption effects are observed. Thus, one of the advantages in using the Raman spectroscopy technique is to overcome the problem of the water absorption. As a consequence, this technique is the method of choice for studying aqueous solutions compared to IR-spectroscopy, being very suitable for biological and medical research (*e.g.* analysis of the impact of drugs on biological cells).

What is more, the Raman spectroscopy is in general a non-destructive technique depending on the intensity of the laser and duration of the experiment.

In Raman spectra, the intensity is measured as a function of the *Raman shift* (in cm^{-1}), which is defined as the frequency difference between

---

[16] In particular in the spectral region of characteristic transition energies (electronic, vibrational or rotational) of the system, the probability to observe inelastic scattering is substantially equal to zero.

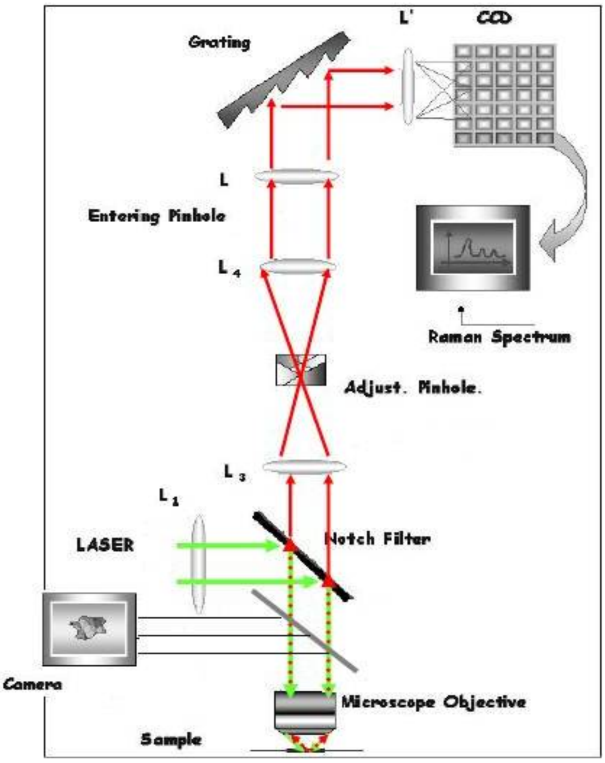

(a) Raman Setup

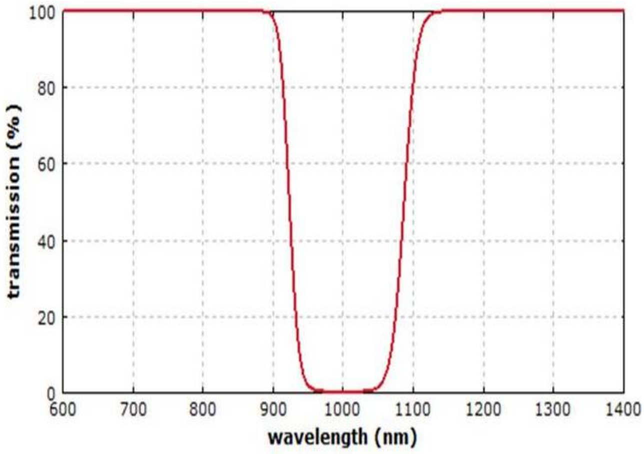

(b) Notch Transmission

Figure 2.13: The laser wavelength can range from the Ultraviolet to the visible and near-Infrared range, depending on the application. A "band-stop filter", as the *Notch filter*, is mandatory to attenuate the Rayleigh scattering and to measure only the Raman intensities.

the scattered light and the incident beam. Therefore the spectrum doesn't dependent on the wavelength of the light source.

The Raman spectrum analysis allows to obtain many useful information about the sample:

- chemical/structural acknowledgement;
- solvent-solute interactions;
- disorder measurements, related to the peaks *full width at half maximum* (FWHM);
- amounts of material;
- crystal symmetry and orientation.

2.2.2 SERS technique

As seen before, the high local optical fields, which occur due to resonances between excitation and scattered field and surface plasmons, provide the main mechanism for the SERS effect (*electromagnetic mechanism*). In addition, a second, so-called *chemical enhancement mechanism*, based on interaction of the molecule with the metallic nanostructures, can increase the Raman cross-section of the adsorbed molecule. The result is a Raman signal enhancement of many orders of magnitude (up to 10^{10}). This strong enhancement (see figure 2.14) of the inelastic scattering (Raman) process observed when molecules reside in close proximity to plasmonic (typically gold or silver) nanostructures makes SERS a powerful vibrational spectroscopy technique that allows for highly sensitive structural detection of low concentration analytes. A very important requirement for quantitative SERS application is a uniform SERS-enhancing substrates providing reliable and reproducible spectral signature of the studied analyte [56]. It is noteworthy that SERS sensing is based on the local field enhancement at the surface of a plasmonic nanostructure, thus the technique is expected to be more sensitive to the first molecular layer covering the metallic substrate.

SERS spectra of organic molecules bound to plasmonic NPs are typically characterized by clear modifications with respect to their conventional Raman counterparts. The most evident feature of SERS data is a redistribution of the spectral weight among the different vibrational bands, and the appearance of new spectral structures, that might be hindered in the conventional Raman spectrum: this is caused by the relaxation of Raman selection rules and the modification to the molecular electronic polarizability occurring upon

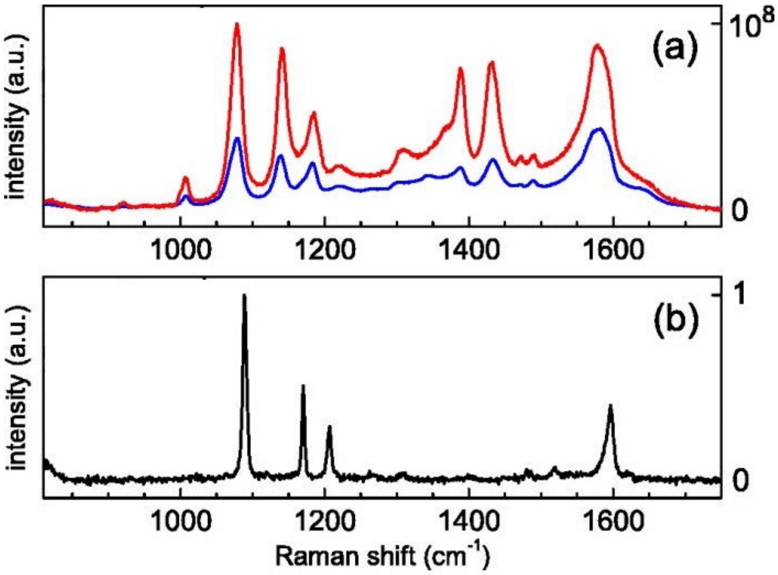

Figure 2.14: (a) SERS spectra from differently sized clusters made of silver nanoparticles functionalized with 4-ATP; (b) Raman spectrum of bulk 4-ATP. SERS and Raman spectra are normalized to single molecule contribution. Note the 10^8 scale factor for SERS spectra in panel (a) [57].

binding the molecule to a metal surface. For the same reason, peaks typically show larger width and can result *red-* or *blue-shifted* in the SERS case.

SERS has progressed from studies of model systems on roughened electrodes to highly sophisticated studies, such as single molecule spectroscopy. The power of SERS lies in its ability to identify chemical species and obtain structural information in a wide variety of fields including polymer and materials science, biochemistry, catalysis and electrochemistry [58]. SERS is a highly sensitive and selective technique for use in the detection of biological samples, *e.g.* SERS probes have the potential to play a primary role in the next-generation sensor technology for monitoring cells and tissues [59].

Chapter 3

Nanomaterials

It has been observed that the properties of certain materials can be modified, improved or adapted in specific ways if, during the fabrication process, their components can be made much smaller. This effect is one of the main reasons behind the physical and engineering interest that had lead in recent years to the development of many kind of *nanostructured materials*. These systems are characterized by at least one dimension in the nanometer range (1 nm = 10^{-9} m). The considerable increase in *surface-to-volume ratio* associated with the reduction in material size to the nanoscale, often have a prominent effect on material performance. Thus, on nanoscale ($1 \div 100$ nm), some physical and chemical material properties can differ significantly from those of the bulk structured materials of the same composition [60, 61]. Nanomaterials can be distinguished in *zero-* (quantum dots and nanoparticles), *one-* (nanowires and nanorods) and *two-dimensional nanostructures* (thin films). In figure 3.1 are shown some examples of nanomaterials, with different composition and shape, from 0D to 3D.

During the past years new nanomaterials with outstanding electrical, optical, magnetic and mechanical properties have been developed for use in information technology, bioengineering and environmental applications. Today these materials can be synthesized and modified with various chemical functional groups which allow them to be conjugated with antibodies, ligands and drugs on demand and, thus, opening a wide range of potential applications in biotechnology, magnetic separation, targeted drug delivery and diagnostic imaging.

Characterization of nanomaterials includes the determination not only of size, shape, surface properties, composition, purity and stability, but also of the atomic and electronic structures. Thus, an employment of specialized techniques is required to characterize the structure and properties of nanomaterials using sophisticated characterization tools such as *high reso-*

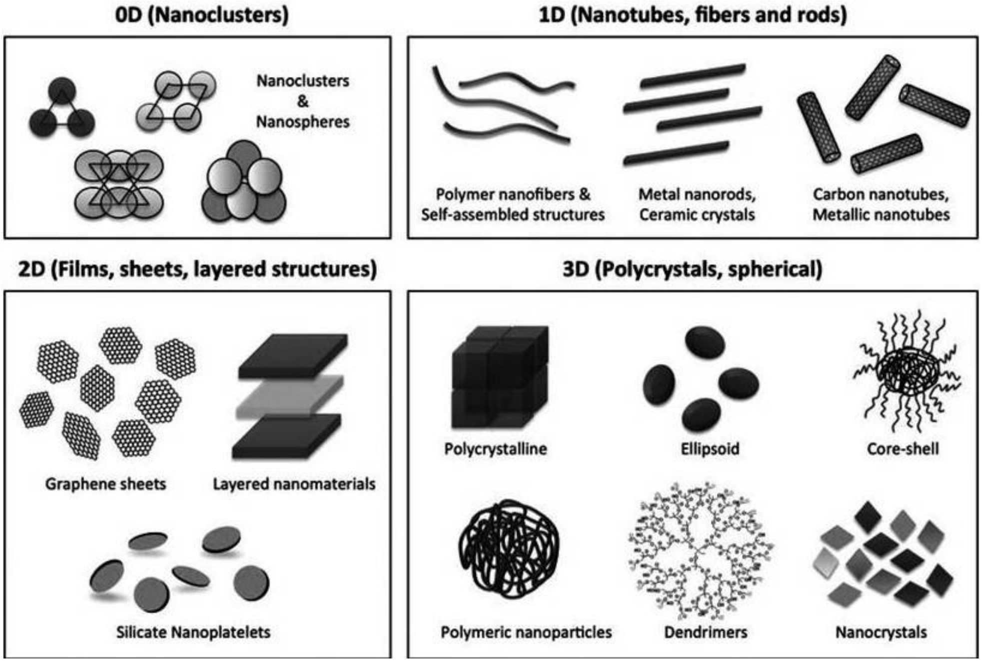

Figure 3.1: Examples of different nanomaterials from 0D to 3D [62].

lution scanning microscopy, *transmission electron microscopy*, *atomic force microscopy*, *scanning tunneling microscopy*, *circular dichroism*, *magnetic resonance*, *mass spectrometry*, *X-ray diffraction*, *neutron diffraction*, *etc...*

3.1 Nanoparticles

Nanoparticles (NPs) are nanosized structures having length and/or width and/or thickness in the nanometers size range. One of the reasons why NPs are attractive for medical and optoelectronic applications is based on their important and unique features, such as their surface to bulk ratio that is much larger than that of other particles, their quantum properties and their ability to adsorb and carry other compounds. Prerequisite for every possible application is the proper surface functionalization of such nanoparticles, which determines their interaction with the environment.

NPs can have many different shapes and compositions (some of them are shown in figure 3.2): solid lipid, polymeric, ceramic, hydrogel, copolymerized peptide, nanocrystals and nanosuspensions, nanotubes and nanowires, noble metal nanoparticles, nanocapsules, *etc...*

NPs, depending on the material they consist of, can possess a number of different properties such as high electron density and strong optical absor-

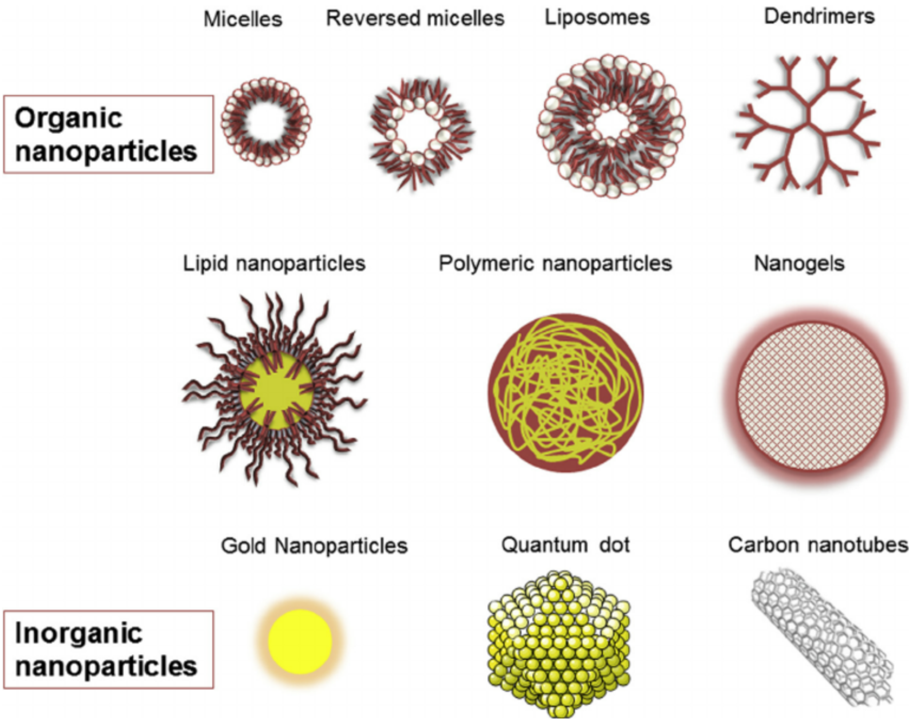

Figure 3.2: Some examples of organic and inorganic nanoparticles [63].

ption (*e.g.* metal particles, in particular Au and Ag), photoluminescence in the form of fluorescence (semiconductor quantum dots), phosphorescence (doped oxide materials) or magnetic moment (*e.g.* iron oxide or cobalt nanoparticles). What is more, NPs have a relatively large (functional) surface which can be exploited to bind, adsorb and carry other compounds such as drugs, probes and proteins. Thus, among the different nano-sized materials, *functionalized nanoparticles* are specially used for biological and nanomedical purposes. NPs surface modification and functionalization can affect the colloidal stability of the particles, and may yield to a controlled assembly or to the selective delivery of nanoparticles to a target, *e.g.* by "capping" the particle surface with appropriate functional molecules.

3.1.1 Metallic nanoparticles

Metallic nanoparticles (MNPs) can show peculiar electric, magnetic, acoustic, optic and superconducting properties, since the number of surface atoms becomes a significant fraction of the total number of atoms. Shape and dimensions can have dramatic influence on optical properties of MNPs. Moreover these properties depend also on surface characteristics and interactions with the surrounding environment or other nanostructures.

In figure 3.3 are shown some TEM (*Transmission Electron Microscopy*) images of gold nanoparticles with different shape and dimension.

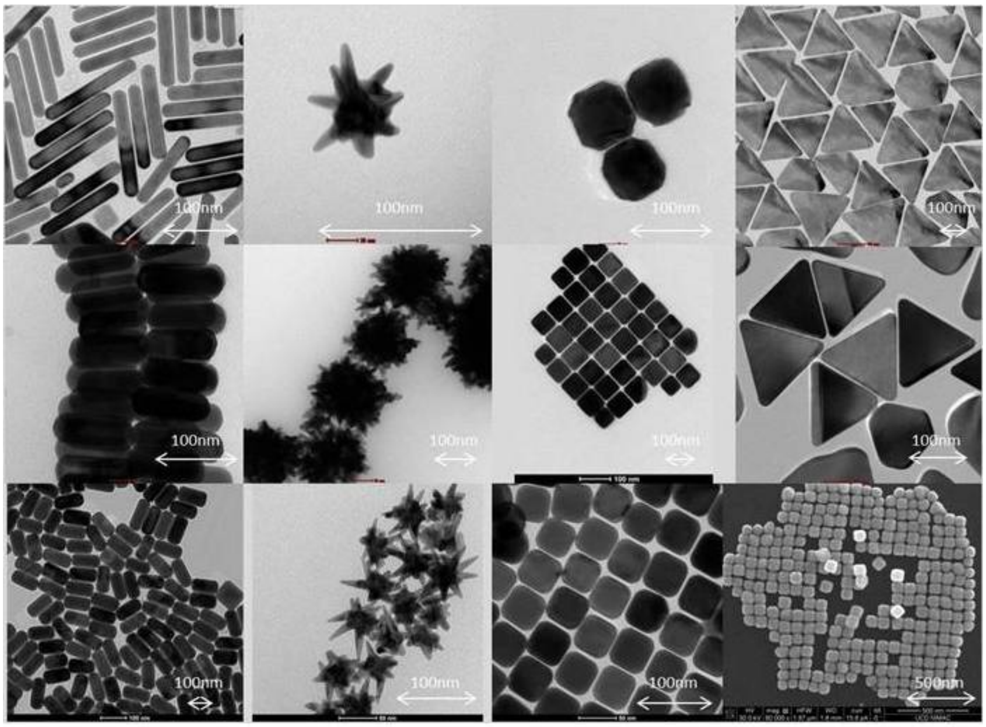

Figure 3.3: TEM micrographs of gold nanoparticles with different shape and dimension [64].

Some chemical and physical properties that are different in MNPs with respect to bulk metals are summarized below:

1. the characteristic absorption wavelength of AuNPs and AgNPs changes by changing size and shape of the particle (as shown in figure 3.4);

2. the reaction efficiency can be enhanced due to the high surface-to-volume ratio (hyperactive catalyst with high selectivity can be made);

3. if the particle diameter is very small (< 10 nm), the melting point is lower than that of bulk metal;

4. the superconductivity transition temperature rises when the NPs dimension is ≤ 1 nm (hightemperature superconductivity material);

5. the mechanical characteristics can be improved and the mechanical strength can be sharply raised (*e.g.* by mixing metals and ceramics to obtain metal matrix composites reinforced with nano-particles [65]);
6. the attractive force of a magnetic metal increases if the particle size decreases (soft-magnetic materials can be made in the form of nanoparticles alloy).

The optical properties of gold and silver nanoparticles are due to their unique interaction with light. The free electrons of the MNPs undergo an oscillation with respect to the metal lattice due to the interaction with the incoming radiation. As seen in Chapter 1, this process is resonant at a particular frequency of the light and is called LSPR. After absorption, the surface plasmon decays radiatively resulting in light scattering or non-radiatively by converting the absorbed light into heat. Thus for example AuNPs with dimension of about 10 nm have a characteristic absorption peak around 520 nm in aqueous solution due to their LSPR [66]. Further MNPs show a stokes shift increasing the size due to the electromagnetic retardation in larger particles.

Concerning AgNPs, it is noteworthy that, while frequently described as being "silver" nanoparticles, some of them are composed of a large percentage of silver oxide due to their large ratio of surface to bulk Ag atoms.

Noble metal nanoparticles of different sizes and shapes combined with conjugated functional polymers give rise to advanced core shell hybrids with interesting physical characteristics and potential applications in sensors or cancer therapy [67].

3.1.2 Stability and biocompatibility

The key to the development of suitable nanosystems is the achievement of a well defined synthesis procedure that enables to control the NPs properties. These properties can be tuned by means of chemical functionalization of the NPs surface.

It is noteworthy that a high quality synthesis protocol must first of all provide a fine control over particle size and shape. Further, the surface functionalization is a mandatory request to prevent the particle aggregation and to control the NPs in liquid and dry forma, as well as to increase the biocompatibility and to load drug onto the NPs surface[1].

---

[1] In general nanoparticles can be administered by parenteral, oral, nasal and ocular routes and by attaching specific ligands onto their surfaces, NPs can be used for directing the drugs to specific target cells. Further the drug targetting can be achieved by manipulating the size and surface characteristics of NPs.

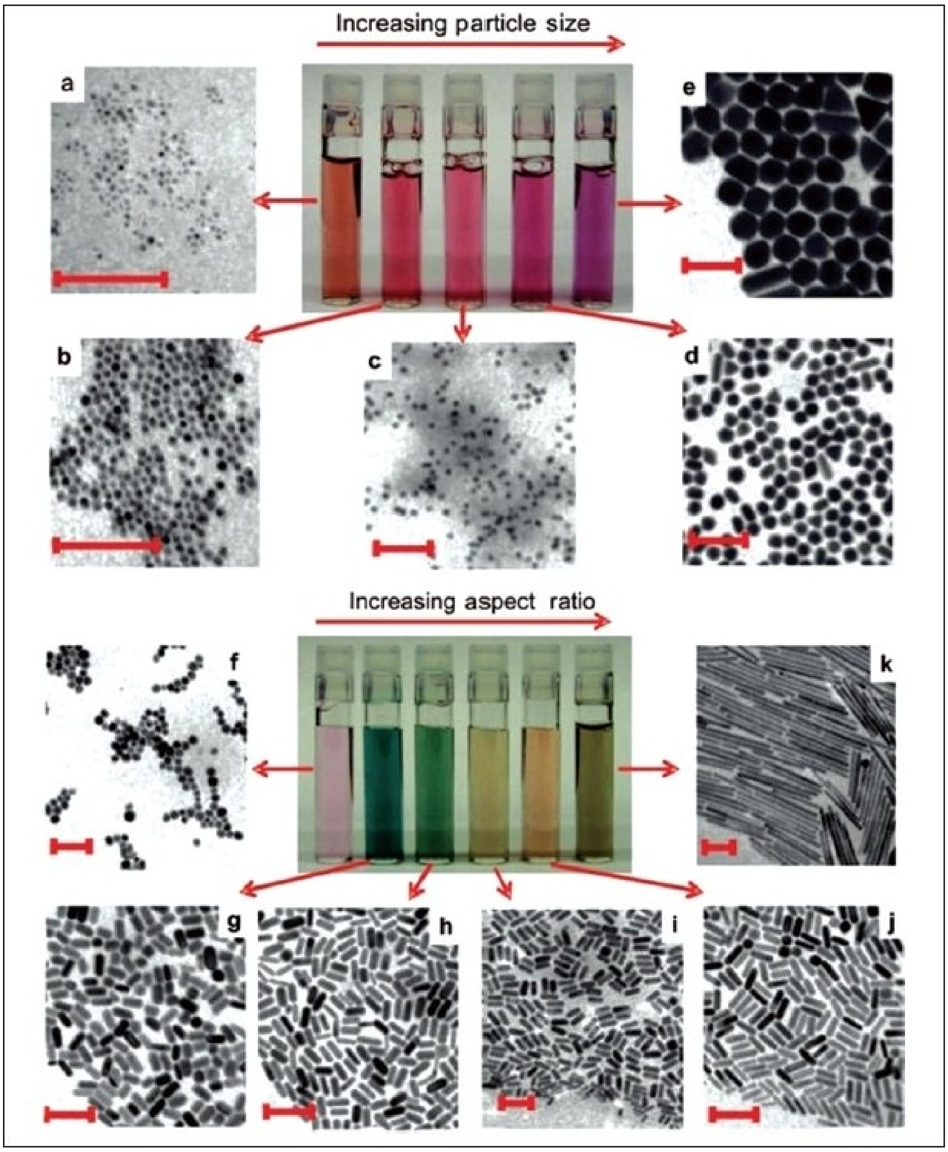

Figure 3.4: Photographs of aqueous solutions of AuNPs (upper panels) and Au nanorods (lower panels) as a function of increasing dimensions. Corresponding TEM (*Transmission Electron Microscopy*) images of the nanoparticles are shown (all scale bars 100 nm). The NPs size varies from 4 to 40 nm (TEMs a-e), whereas for rods, the aspect ratio varies from 1.3 to 5 for short rods (TEMs f-j) and 20 (TEM k) for long rods [68].

One of the synthesis methods to obtain functionalized MNPs is the so-called *Molecule-Capping Method*, in which the metallic clusters are capped with appropriate organic ligands. This method allows to control some of the most important properties related to biomedical applications, such as:

1. size;
2. aqueous solubility and stability;
3. surface charge and permeability;
4. degree of biodegradability;
5. biocompatibility and toxicity.

It is noteworthy that the ligand molecules bound to the nanoparticle surface not only control the growth of the particles during synthesis, but also prevent the aggregation of the nanoparticles. When properly stabilized by a shell of ligands such as thiols, amines, ammonium salts and polymers, noble metal nanoparticles display excellent stability toward aggregation, which enables attempts to achieve nanoparticles with different sizes and shapes.

3.1.3 Applications: overview

The unique properties of nanoscale materials have given rise to tremendous research activity directed towards nanoparticles fabrication, characterization and applications.

The peculiar chemical, physical, and mechanical properties of NPs, as well as the possibility to control their properties by means of surface chemical functionalization, make them a very interesting material. Metal NPs, metal oxide NPs, magnetic NPs and quantum dots are a versatile class of materials for biomedical sciences and engineering. In particular, as seen before, size reduction can lead to a whole range of new physicochemical properties that make MNPs excellent candidates for biomedical applications as variety of biological processes occur at nanometer scales. The development of metallic NPs has become the centre of attraction in the modern era of nanomaterials due to their unique intrinsic properties such as excellent optical, electrical, catalytic and magnetic behaviour, chemical and mechanical stability, ease of surface modification, large surface area for reactions, *etc...*

The variations in size, shape and surface chemistry of metal NPs affect their properties to a great extent which in turn have an influence on their biological behaviour. Few metal NPs offer unique optical properties while others possess paramagnetic behaviour and quantum size effect which make them suitable in bio-imaging diagnostic techniques. Some metallic NPs play a role in tissue engineering and other therapeutic applications due to their ease of surface modifications, large surface area to volume ratio, unique electrical and anti-microbial activities.

Today these materials can be synthesized and modified with various chemical functional groups which allow them to be conjugated with antibodies, ligands and drugs of interest, thus opening a wide range of potential applications (some of them are summarized in figure 3.5) in the fields of nanomedicine [69, 70] (*e.g* for immunology, diagnosis, tissue engineering and therapy) and optoelectronics (*e.g.* for laser applications, optical detectors, sensors, solar cells, photoelectrochemistry).

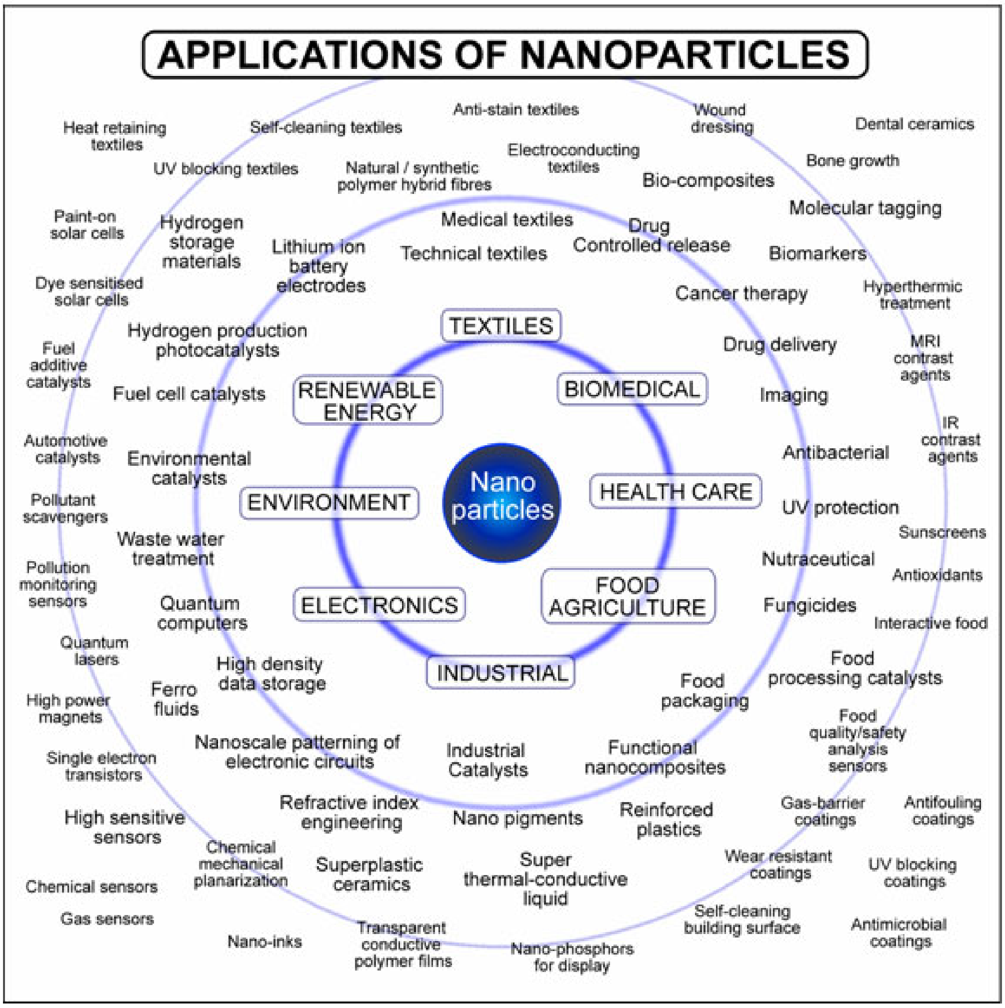

Figure 3.5: Array of nanoparticles applications [71].

Moreover, due to their attractive physicochemical properties, silver NPs have received considerable attention in biomedical imaging using SERS [72], because of the surface plasmon resonance and large effective scattering cross-section of individual AgNPs that make them ideal candidates for molecular labeling.

Consequently, with such wide range of applications available, these particles have potential to make a significant impact to the society.

Chapter 4

Materials and Methods

This chapter contains the description of synthesis and preliminary characterizations of the here investigated nanosystems. The synthesis procedure and preliminary measurements were carried out at the *Department of Chemistry* (University of Rome “Sapienza”, Italy).

In the following section the synthesis procedure to obtain an innovative nano-sized system, composed by gold and silver NPs functionalized by *sodium 3-mercapto-1-propansulfonate* (3MPS) and *2-diethylaminoethanethiol hydrochloride* (DEA), chosen on purpose for the biomedical applications, will be briefly described.

The MNPs were synthesized with different thiols molar ratios with the aim to modulate the properties of the functionalized metal nanoparticles. Reference samples, *i.e.* single-thiol functionalized MNPs (*AuNPs/3MPS*; *AuNPs/DEA*; *AgNPs/3MPS*; *AgNPs/DEA*), were also synthesized. Finally, to obtain a better understanding of the system, thiol thick films were prepared and their synthesis procedure will be reported.

In section 4.2 an overview on the preliminary characterization techniques will be shown and the measurements results will be presented and briefly discussed. Finally, in the last section of this chapter, the experimental setup for SR-XPS and SERS measurements will be described.

4.1 Synthesis procedure

For the functionalized nanoparticles (see figure 4.1 (b)) synthesis, two organic thiols were used: the sodium *3-mercapto-1-propansulfonate* (3MPS) and the *2-diethylaminoethanethiol hydrochloride* (DEA), their structural formulas are shown in figure 4.1 (a). 3MPS gives stability and enhances the water solubility of the system [73] (a mandatory condition in view of MNPs

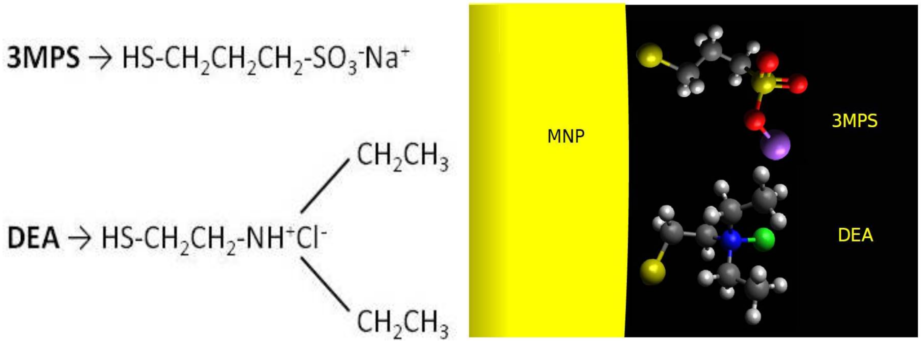

(a) 3MPS and DEA structural formulas (b) Functionalized MNPs

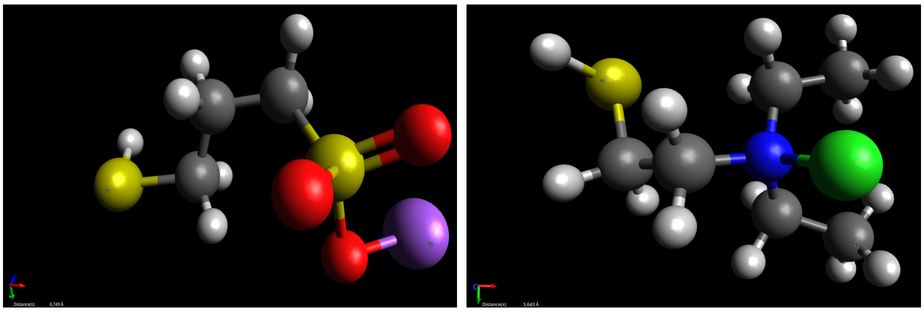

(c) 3MPS thiol (d) DEA thiol

Figure 4.1: Structural formulas of 3MPS and DEA thiols (a); schematic representation of the functionalized MNPs (b); 3MPS (c) and DEA (d) thiols. Reference: open source cross-platform molecular editor *Avogadro 1.1.1*.

subministration to cells), while DEA can improve the uptake in cell and the conjugation of drugs or other specific agents.

As seen before, the chemical functionalization allows to obtain a stable and biocompatible system, suitable for *ad hoc* further functionalization as required for several applications in biotechnology. What is more, the capping molecules play a double role: on one hand, they protect and stabilize the MNPs, preventing their aggregation; on the other, they can be opportunely selected to functionalize the metal cluster, thus making the resulting hybrid system better suited for the application of interest [74, 75].

Functionalization of metallic NPs with organic ligands by means of *molecule-capping method* [76, 77], is a synthesis route specifically addressed to the massive NPs production, thus providing a reliable control of particle composition, shape, size, monodispersity, stability and solubility in aqueous solution[1],

---

[1] The ability to prepare metal nanoparticles with such properties is a mandatory prerequisite for applications in nano-biotechnology.

with low preparation costs.

The synthesis of Au and AgNPs stabilized with 3MPS (or DEA) was performed through reduction reaction in aqueous phase, according to literature reports [78, 79, 80, 81], starting from *Hydrogen Tetrachloroaurate (III) Trihydrate* ($HAuCl_4 \cdot 3H_2O$, Aldrich, 99.9%), or *Silver Nitrate* ($AgNO_3$ Aldrich, 99%), as metallic precursors and 3MPS and DEA as thiolic ligands. *Sodium Borohydride* ($NaBH_4$, Aldrich, 99%) was used as a reducing agent in molar ratio metal/reductant 1/10 (figure 4.2). The reaction mixtures were allowed to react for about 2h. Deionized water (electrical conductivity less than 1 μmho/cm at room temperature) was obtained from a Millipore Milli-Q water purification system. Argon flux was allowed to flow through the reaction solvents for deoxygenating the reactions, which were further performed under controlled argon atmosphere. The silver and gold NPs were prepared at room temperature in a two phase system, following a procedure reported elsewhere [82]. Deionized water, obtained from Zeener Power I Scholar-UV (electrical resistivity 18.2MΩ) instrument, was maintained under argon and vigorous stirring for 10 min at room temperature, for both silver and gold NPs [83]. The purification was obtained by means of centrifugation with deionized water (15 min, 5000 rpm) and dialysis. Stable colloidal suspensions were recovered and purified in cellulose ester dialysis membrane (molecular weight cutoff (MWCO) = 12 kDa) for 3 days, recharging with deionized water every 12 h to remove the excess of ions and free thiols. Lyophilization of the suspensions gave rise to stable NP precipitates that can be easily resuspended in water.

Concerning the 3MPS (or DEA) thick film preparation, gold-coated silica wafers prepared by growing Au film 4000 Å thick onto Si(111) substrates were cut into slices (ca. 3 mm thickness and 1 cm^2 surface) and washed with acetone, ethanol and chloroform, and then blown dry with nitrogen. An aqueous solution of 3MPS (or DEA) at concentration 1 mg/mL in deionized water, and a freshly washed gold substrate was dipped into the solution for about 8h.

The "mixed-ligands functionalization" of gold and silver nanoparticles (samples *AuNPs/3MPS/DEA* and *AgNPs/3MPS/DEA*) was performed using the well assessed synthetic procedure described before: reduction reaction of *Tetrachloroauric Acid* (or *Silver Nitrate*) to metallic atoms by means of *Sodium Borohydride* as reducing agent, in the presence of 3MPS and DEA as functionalizing thiols. In table 4.1 are reported all the here studied samples with their metal/thiols synthesis stoichiometric ratios.

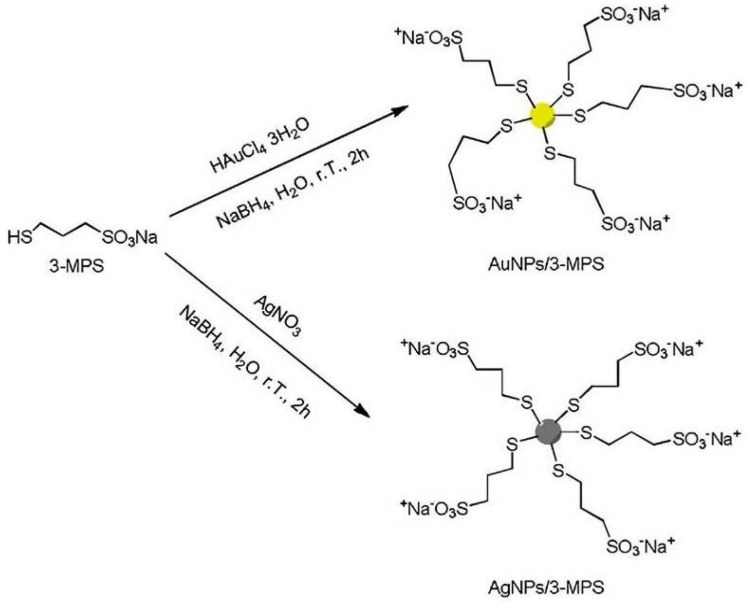

(a) *NPs/3MPs* synthesis scheme

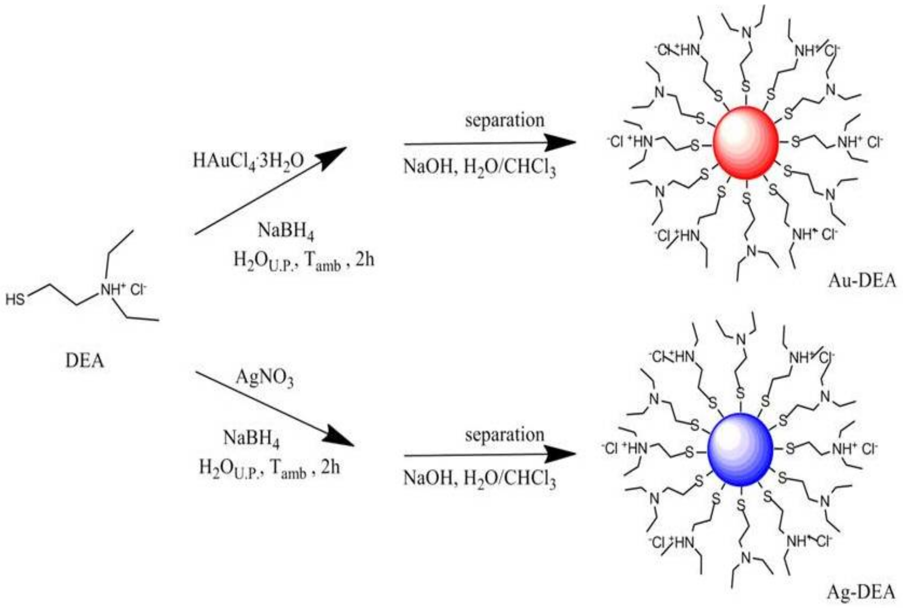

(b) *NPs/DEA* synthesis scheme

Figure 4.2: Synthesis procedure scheme to obtain gold and silver NPs functionalized by 3MPS or DEA.

Sample Name	**X Au**	**X Ag**	**X 3MPS**	**X DEA**
AuNPs/3MPS	1	-	4	-
AuNPs/DEA	1	-	-	10
AgNPs/3MPS	-	1	4	-
AgNPs/DEA	-	1	-	10
AuNPs/3MPS/DEA (1)	1	-	10	1
AuNPs/3MPS/DEA (2)	1	-	10	2
AgNPs/3MPS/DEA (1)	-	1	10	1.25
AgNPs/3MPS/DEA (2)	-	1	10	2.5

Table 4.1: Stoichiometric molar ratios of synthesized samples.

4.2 Preliminary characterization methods

After purification, the preliminary characterization was carried out by means of *UV-vis Absorption* technique, *Dynamic Light Scattering* (DLS), ζ *Potential* and *Nuclear Magnetic Resonance* (NMR) measurements. *Field Emission Scanning Electron Microscopy* (FESEM) images were also collected on all the samples.

4.2.1 UV-vis Absorption

The formation of functionalized MNPs recovered from the reaction mixture was confirmed using UV-visible spectral analysis. NPs can show emission intensity maxima at different wavelengths of excitation and emission, these wavelength values are influenced by the NPs mean size, as well as by their shape, as predicted in the literature [84].

UV-vis spectra were run in deionized water or $CHCl_3$ solutions by using quartz cells with a Varian Cary 100 scan spectrophotometer. FTIR, FIR, and ATR transmission infrared spectra have been acquired by a Bruker Vertex 70 spectrophotometer in the spectral range $4000 \div 400$ and $600 \div 200$ cm^{-1} on cast-deposited films from chloroform or water solutions using KRS-5 cells.

The UV-vis spectrum, see figure 4.3, shows the typical surface plasmon resonance band[2], at about 520 nm and 420 nm (for AuNPs and AgNPs, respectively) in agreement to literature reports [36].

All measured optical properties and, in particular, the plasmon absorp-

---

[2] It is noteworthy that the nanoparticle absorption wavelength can shift accordingly to the NP composition, dimension, shape and surface modifications.

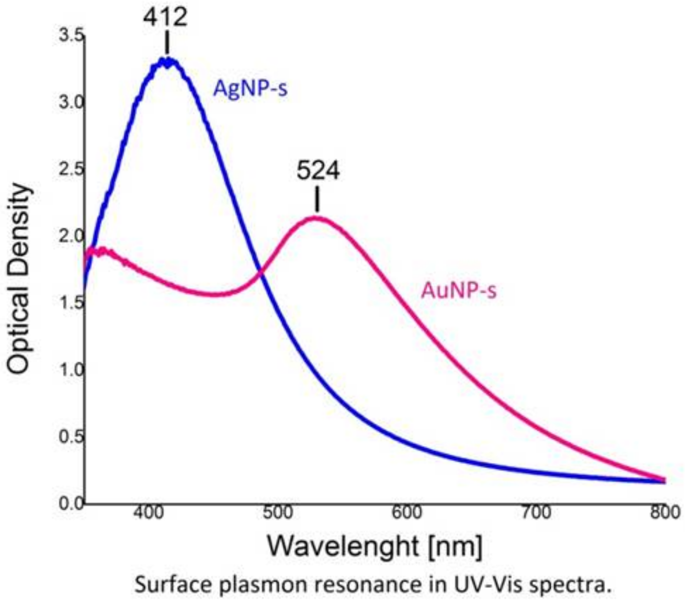

Figure 4.3: Uv-visible spectra of reference samples *AuNPs/DEA* and *AgNPs/DEA* are reported as example.

tion, were stable in time and reproducible. This indicates that the capped nanoparticles are stable towards aggregation, *i.e.* the optical characterization results were not affected by aggregation.

4.2.2 DLS and ζ Potential

The samples have been investigated by DLS and ζ Potential to asses size and stability.

The DLS (*Dynamic Light Scattering*), also called PCS (*Photon Correlation Spectroscopy*), technique is based on the elastic scattering related the coupling between the electromagnetic field and the scattering centers inside the sample. This technique allows to measure the *Hydrodynamic Radius*[3] of the particles inside a solution in a wide range, from few nanometers up to micron, and is well suited to investigate systems such as emulsions, colloids, micelles, proteins, polymers and biological macromolecules in solution.

Zeta Potential measurements have been used to obtain the MNPs surface charge and to investigate the stability of the functionalized NPs in solution.

---

[3] It is noteworthy that this radius is not equal to the effective radius of the particle. The hydrodynamic radius is the radius of an hypothetical particle that is moving inside the solution with the same *diffusion coefficient* measured during the DLS experiment and usually is higher than the real particle radius.

ζ Potential was measured using the *laser Doppler velocimetry* technique and particle velocity was expressed per unit field strength as the electrophoretic mobility[4] [85].

The size distribution and the ζ Potential of the nanoparticles in aqueous solution have been investigated using a Zetasizer Nanoseries Malvern (see figure 4.4) equipped with a 4 mW He-Ne laser at a 632.8 nm and at a temperature of 25.0±0.2 °C.

(a) Zetasizer Nano ZS (b) Dip cell

Figure 4.4: Malvern DLS instrumentation: (a) Zetasizer Nano ZS, (b) *Dip cell* with palladium electrodes for ζ Potential measurements.

The DLS measurements, see figure 4.5, evidence the presence of nanoparticles with a hydrodynamic diameter < 10 nm for all the here presented samples, with a narrow size distribution (see figure 4.5 and table 4.2). The measured values of hydrodynamic radius and Zeta potential are reported in table 4.2, the negatively charged surface of the functionalized MNPs prevents the aggregation in water solution.

4.2.3 FESEM

Compared with convention *Scanning Electron Microscopy* (SEM), *Field Emission SEM* (FESEM) produces clearer, less electrostatically distorted images with spatial resolution down to 1 nanometer, providing useful topographical and elemental information. Some advantages of this technique are the abilities to examine small-area contamination spots, to reduce the penetration of low-kinetic-energy electrons probes closer to the immediate material surface and to obtain high-quality low-voltage images with negligible electrical

---

[4] The ζ Potential can be obtained from electrophoretic mobility measurements by means of the *Smoluchowski equation*:

$$U_E = \frac{\epsilon\zeta}{\eta}$$

where U_E is the electrophoretic mobility, ϵ is the solution dielectric constant and η is the solution viscosity.

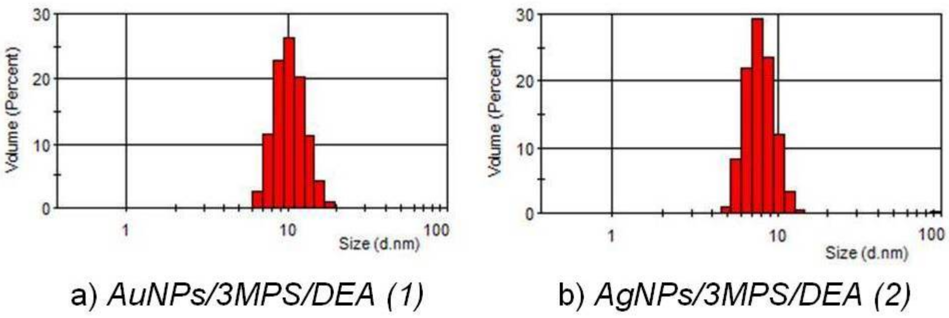

Figure 4.5: DLS size distributions of *AuNPs/3MPS/DEA* (a) and *AgNPs/3MPS/DEA* (b) samples are reported as example.

charging of samples (accelerating voltages ranging from 0.5 to 30 kilovolts) with essentially no need for placing conducting coatings on insulating materials. A field-emission cathode in the electron gun of a scanning electron microscope provides narrower probing beams at low as well as high electron energy, resulting in both improved spatial resolution and minimized sample charging and damage.

FESEM images have been obtained using a Zeiss Auriga 405 (figure 4.6), adopting a voltage level of 7.5 keV and a working distance of 2.5 mm, on freshly prepared films drop casted from deionized water solutions (c=1 mg/mL) directly on the metallic sample holder.

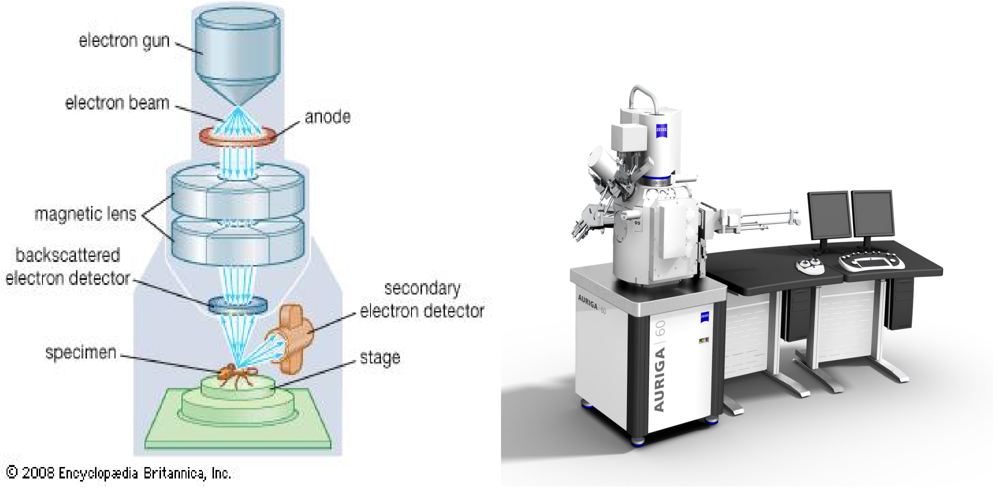

(a) SEM setup (b) Auriga workstation

Figure 4.6: FESEM experimental setup: (a) SEM block diagram, (b) Auriga workstation for FESEM measurements.

In figure 4.7 are reported as example two FESEM images of mixed-thiols functionalized MNPs.

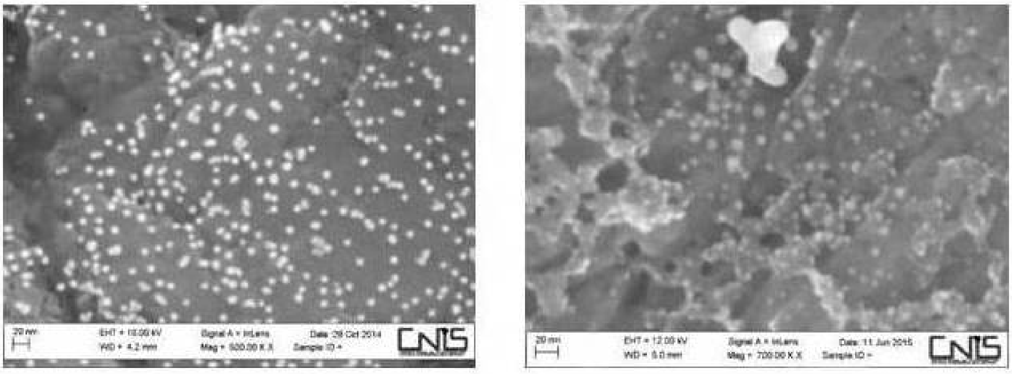

a) *AuNPs/3MPS/DEA (2)* b) *AgNPs/3MPS/DEA (1)*

Figure 4.7: FESEM images of *AuNPs/3MPS/DEA* (a) and *AgNPs/3MPS/DEA* (b) samples are reported as example.

In table 4.2 are reported the ζ Potential, DLS and FESEM measurements for all the here presented samples.

Sample	**ζ Potential**	**DLS**	**FESEM**
AuNPs/3MPS	-41±3 mV	37 nm	7 nm
AuNPs/DEA	30±5 mV	10 nm	5 nm
AgNPs/3MPS	-38±5 mV	15 nm	5 nm
AgNPs/DEA	40±5 mV	18 nm	3 nm
AuNPs/3MPS/DEA (1)	-26±10 mV	10 nm	7 nm
AuNPs/3MPS/DEA (2)	-30±3 mV	8 nm	5 nm
AgNPs/3MPS/DEA (1)	-35±5 mV	8 nm	6 nm
AgNPs/3MPS/DEA (2)	-20±10 mV	7 nm	6 nm

Table 4.2: ζ Potential, DLS and FESEM measurements.

4.2.4 NMR

Nuclear magnetic resonance (NMR) studies allowed to assess the presence of chemisorbed and physisorbed thiol molecules, confirming the binding of 3MPS (and/or DEA) with Au (or Ag) on the nanoparticle surface and thus, the effectiveness of the functionalization process.

NMR spectroscopy is a powerful technique for nanoparticle analysis. It is able to identify the species bound to the nanoparticle surface by monodimensional ^{1}H spectra.

To evaluate the binding of 3MPS and/or DEA on MNPs, preliminary studies of reference samples (*AuNPs/DEA*; *AuNPs/3MPS*; *AgNPs/DEA*; *AgNPs/3MPS*) was carried out through monodimensional ^{1}H NMR, as well (see figure 4.8).

4.3 Experimental setup of SR-XPS and SERS

4.3.1 SR-XPS

High resolution XPS experiments (HR-XPS) were carried out at the BACH (*Beamline for Advanced DiCHroism*) line at the ELETTRA synchrotron facility in Trieste [86], to probe the nature of the interactions at the metal/organic ligands interface as well as the stability of the functionalized systems and capping molecules.

Elettra is a third generation synchrotron facility located in Basovizza (Trieste) optimized for the VUV and soft X-ray energy range. The electrons, which are produced in bunches by thermoionic emission are extracted by an electric field of 80 kV and accelerated through a straight section (*linear accelerator*, LINAC) by two radio-frequency structures. Then the electrons are injected into a booster ring where they reach the operating energy (2 or 2.4 GeV) and delivered to the storage ring through a series of deflection and focusing magnets. Inside the ring, the electrons are maintained on a circular orbit by different types of magnets (bending magnets, quadrupoles and sextupoles), and the energy they lose by emission of synchrotron radiation is reintegrated by four radio-frequency cavities. The storage ring includes straight sections which host insertion devices, in particular undulators at the beginning of the beamlines. An undulator is formed by two periodic arrays of magnetic poles which force the incoming electrons on a wiggling trajectory, inducing the emission of a collimated, high brilliance beam.

Synchrotron radiation has many advantages compared to conventional XPS sources, such as the tunability of the photon energy and the light polarization, which can be accessed by properly adjusting the undulator gap and the monochromator. These properties enable optimizing the cross section of the electronic levels and varying the escape depth of emitted electrons, and could allow a better understanding on the molecular orbital orientation and/or the magnetic properties of the elements (*i.e* the orbital and spin magnetic moments). The possibility to change the photon energy is also

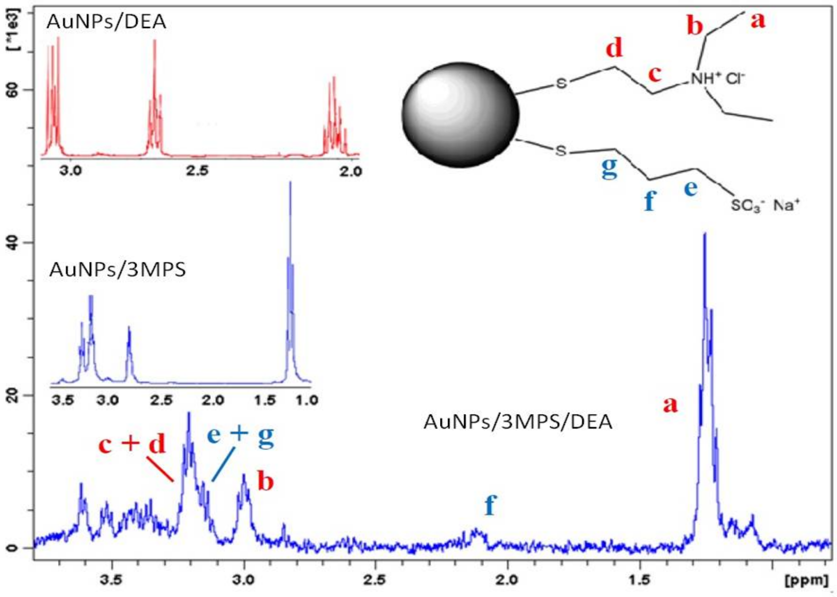

(a) NMR spectrum of functionalized AuNPs

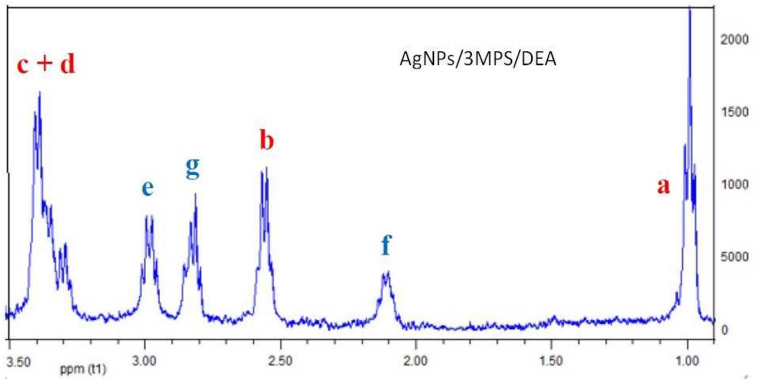

(b) NMR spectrum of functionalized AgNPs

Figure 4.8: NMR spectra of reference samples and *AuNPs/3MPS/DEA (2)* are reported in (a), NMR spectrum of *AgNPs/3MPS/DEA (2)* sample is reported in (b).

fundamental for the acquisition of *X-Rays Absorbtion* spectra (XAS), which provides chemical characteristics based on the X-ray induced resonant electronic transitions from the core levels into unfilled electronic states, and gives information about local charge state, and coordination of atoms.

BACH beamline. BACH delivers a photon beam with high intensity and brilliance in the soft X-rays energy range (35-1650 eV) with the full control of the polarization of the light. The following techniques are implemented: XPS (*X-ray Photoelectron Spectroscopy*), UPS (*Ultraviolet Photoelectron Spectroscopy*), XAS (*X-ray Absorption Spectroscopy*), XMCD (*X-ray Magnetic Circular Dichroism*), XMLD (*X-ray Magnetic Linear Dichroism*).

The beamline is provided by two APPLE-II elliptical undulators that are used alternatively in order to optimize the flux. The photon dispersion system is based on a VASGM dispersion system (*Variable Angle Spherical Grating Monochromator*) and it includes four different interchangeable spherical gratings.

The flux in the experimental chamber, measured with the high resolution gratings for linearly polarized light at the best achievable resolution, ranges between $1.2 \cdot 10^{12}$ photons/s at 125 eV and $6 \cdot 10^{10}$ photons/s between 900 eV and 1250 eV.

The beamline offers a multi-technique approach for the investigation of the electronic, chemical, structural, magnetic and dynamical properties of materials. For this purpose BACH hosts three separate branches which are independent experimental chambers (branches A, B and C, which cannot however be used simultaneously). The beam can be directed on the different experimental end-stations by adjusting the corresponding refocusing sections with plane-elliptical mirrors in a Kirkpatrick-Baez configuration, providing free spots on the samples.

The experimental setup of the BACH beamline is shown in figure 4.9.

End-station A allows to perform a multi-spectroscopy investigation with high resolution XPS, ARPES, XAS (*total electron yield*, TEY; *partial electron yield*, PEY; *total fluorescence yield*, TFY), and X-ray magnetic circular dichroism (XMCD) in remanence. A sputter gun, a *low energy electron diffraction* (LEED) and several electron beam evaporators are available for the *in situ* preparation of the samples. Different materials (metals, inorganic and organic molecules) can be deposited on the sample surface at different temperatures (40K-700K). The experimental setup of the BRANCH A can also combine Laser and Synchrotron Radiation in order to study the dynamics of the photo-induced excited states of electronic and magnetic systems with pump-probe time-resolved XAS spectroscopy to investigate dynamic processes in the time between 70 ps up to 0.5 μs.

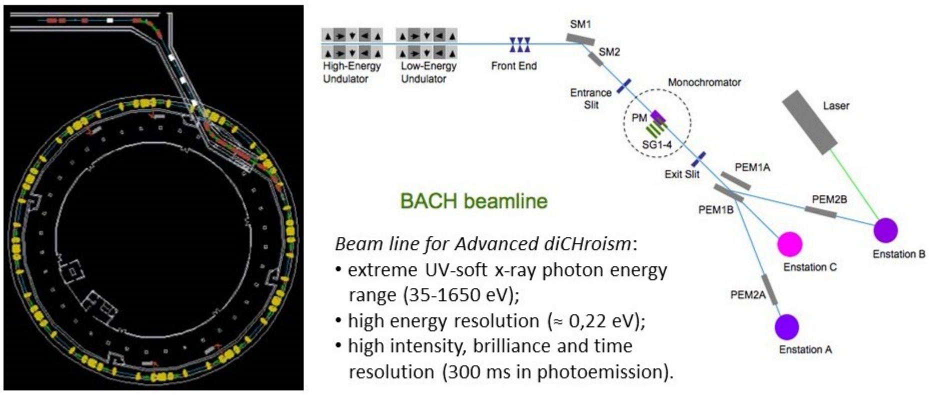

Beam line for Advanced diCHroism:
- extreme UV-soft x-ray photon energy range (35-1650 eV);
- high energy resolution (≈ 0,22 eV);
- high intensity, brilliance and time resolution (300 ms in photoemission).

General layout of the ELETTRA accelerator complex showing the position of the linac, transfer line and storage ring.

Figure 4.9: SR-XPS experimental setup of BACH beamline at Elettra facility.

End-station B hosts a cryomagnet and it is dedicated to XMCD measurements in high magnetic fields (± 6.5 Tesla) along the beam and variable temperature from 1.9 K to 340 K on the sample in a base pressure of $4{\cdot}10^{-11}$ mbar.

End-station C is also available for the installation of user end-stations for long term projects. It will be dedicated to *in situ* and *in operando* soft-X-rays XAS measurements in environmental conditions for unravelling the electronic properties at the solid-liquid interfaces by using suitable UHV compatible cells provided of Si_3N_4 and/or graphene windows to seal the liquid.

High-resolution XPS data were collected by means of a VG-Scienta R3000 hemispherical electron energy analyser. A scheme of the XPS set-up in the main chamber of end station A at BACH beamline is shown in Figure 4.10.

XPS data were collected in angular mode (A21, pass energy = 50 eV). *Photon energies* (PE) of 380 eV were used for C1s, S2p, Na1s, Cl2p, Au4f spectral regions, and PE of 596 eV was selected to acquire O1s, N1s and Ag3d core levels spectra, with energy resolution $\Delta E = 0.22$ eV. The Au Fermi energy, the aliphatic C1s signal and metallic Ag3d$_{5/2}$ and Au4f$_{7/2}$ signals were used for the energy scale calibration. XPS data analysis was performed via curve-fitting of S2p, Ag3d and Au4f experimental spectra, by using a combination of Voigt shaped peaks, after subtraction of a Shirley background. The S2p$_{3/2}$-S2p$_{1/2}$, Ag3d$_{5/2}$-Ag3d$_{3/2}$ and Au4f$_{7/2}$-Au4f$_{5/2}$ doublets were fitted by using the same FWHM (*full width half maximum*) for the two spin-orbit components of the same signal, a spin-orbit splitting of

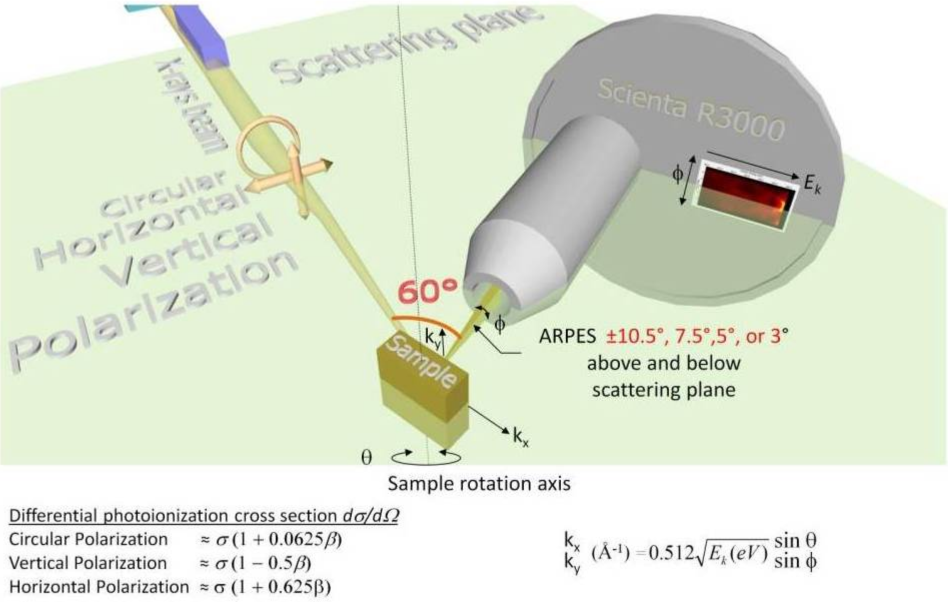

Figure 4.10: Scheme of the XPS set-up in the main chamber of end station A at BACH beamline (from BACH webpage).

1.2 eV for S2p, 6.0 eV for Ag3d and 3.3 eV for Au4f, and branching ratios $S2p_{3/2}/S2p_{1/2}=2$, $Ag3d_{5/2}/Ag3d_{3/2}=3/2$, $Au4f_{7/2}/Au4f_{5/2}=4/3$ respectively have been detected. In case of identifying presence of many chemically different species of the same element, the same FWHM value was used for all individual photoemission bands in order to reduce the number of refinement parameters then improving the reliability of the results.

All the samples were deposited, by means of a drop casting procedure, on a silicon wafer substrate ($TiO_2/Si(111)$).

4.3.2 SERS

Raman and SERS spectra were acquired by employing a Horiba HR-Evolution microspectrometer (shown in figure 4.11), equipped with a 25 mW He-Ne laser (632.8 nm wavelength) and a set of neutral power attenuating filters.

The exciting power was kept below 0.5 mW for SERS measurements. The spectrometer is coupled with a confocal microscope equipped with a set of objectives at different magnifications (100 x -0.8 NA was used for this experiment). A 600 lines per mm diffraction grating ensured a spectral resolution better than 3 cm^{-1}. The sample can be moved with a software controlled mapping stage with sub-micrometric precision for collecting automatized spectroscopic mapping. SERS spectra were acquired on the con-

Figure 4.11: Horiba HR-Evolution microspectrometer.

jugated nanoparticle systems after inducing their self-assembly into clusters on a clean glass substrate.

In order to calculate an average SERS signal several spectra were collected from different points, 2 μm spaced points, typically over a 12 x 12 μm^2 sample surface. It was noticed that measurements from distinct points did not differ in spectral shape but basically by an overall intensity factor as expected from a self-assembled SERS substrate. All the spectra are presented after a polynomial baseline subtraction performed using LabSpec software. The frequency of the Raman and SERS vibrational bands was determined by a careful fitting procedure using Lorentzian/Gaussian lineshapes.

Chapter 5

Data analysis

In this section, SR-XPS and SERS data analysis on silver and gold NPs stabilized by the negatively charged hydrophilic organic thiol *Sodium 3-mercapto-1-propanesulfonate* (3MPS) and *2-diethylaminoethanethiol hydrochloride* (DEA) will be presented and discussed. Thick films of pure 3MPS or DEA deposited onto a polycrystalline gold surface (Au/Si(111) wafer) and "single-thiol" functionalized Au and AgNPs, were also measured as reference for the SR-XPS data analysis of NPs functionalized with "mixed ligands"; for analogous purpose, pure 3MPS and DEA Raman spectra were acquired and analyzed and the results were compared with the SERS spectra of functionalized Au and AgNPs.

The "mixed-thiols" functionalized Au and AgNPs have been prepared with different metal/thiols stoichiometric ratios and have been carefully purified to control their size and monodispersity, through the synthesis procedure described in Chapter 4.

In the last section a new system formed by palladium NPs stabilized and interconnected through rod-like bifunctional organometallic thiols containing square-planar Pt(II) centres, *i.e.* *trans, trans*-$[(HS)Pt(PBu_3)_2(C{\equiv}C\text{-}C_6H_4\text{-}C_6H_4\text{-}C{\equiv}C)(PBu_3)_2Pt(SH)]$ (Pt-DEBP), will be presented and characterized by means of SR-XPS. A comparison with analogous networks formed by Au and AgNPs, through trinuclear Au(or Ag)-S-Pt bridges, will be reported and discussed as well.

5.1 Reference samples

The main characterizations, through SR-XPS and SERS measurements, of 3MPS and DEA thiols thick films and *AuNPs/3MPS*, *AgNPs/3MPS*, *AuNPs/DEA* and *AgNPs/DEA* products are reported in this section.

5.1.1 3MPS thick film, *AuNPs/3MPS* and *AgNPs/3MPS*

SR-XPS Measurements. Ag3d and Au4f core levels SR-XPS data and best fits for the nanoparticles samples are shown in figure 5.1; the main quantitative results are summarized in table 5.1.

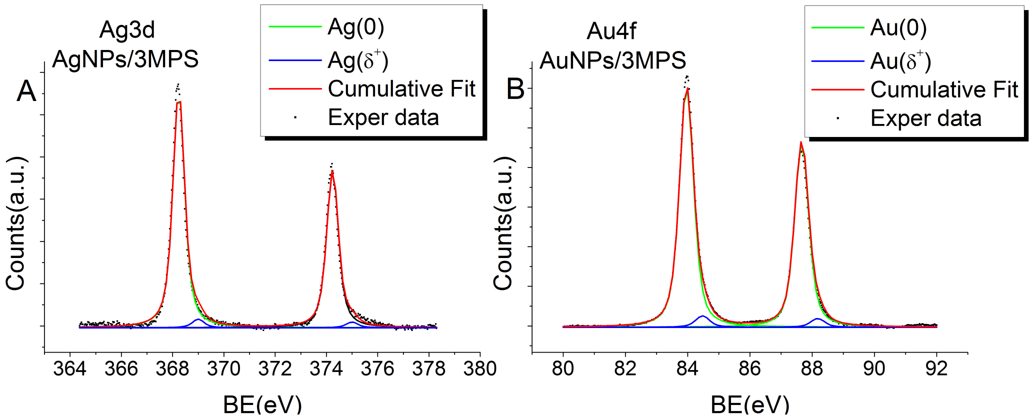

Figure 5.1: Ag3d and Au4f core levels spectra of silver nanoparticles (panel A) and gold nanoparticles (panel B).

Sample	Signal	BE	FWHM	*I ratio	Assignments
AgNPs/3MPS	Ag3d$_{5/2}$	368.24	0.55	97%	Ag(0)
	Ag3d$_{5/2}$	369.00	“	3%	Ag(δ^+)
AuNPs/3MPS	Au4f$_{7/2}$	83.96	0.54	95%	Au(0)
	Au4f$_{7/2}$	84.48	“	5%	Au(δ^+)

*I ratios=I_{peak}/I_{tot} signal for a selected element

Table 5.1: SR-XPS Ag3d$_{5/2}$ and Au4f$_{7/2}$ metals core levels data collected on silver and gold NPs stabilized by 3MPS (BE, FWHM, atomic ratio and assignments).

Following a curve fitting procedure, two spin-orbit pairs of components were individuated in the Ag3d SR-XPS spectrum (see figure 5.1, panel A). The main Ag3d$_{5/2}$ component is centred at 368.24 eV *Binding Energy* (BE) value and corresponds to metallic silver atoms in the nanoparticles core, as expected and well reported in literature for functionalized Ag nanoparticles [87, 88]. The second spin-orbit pair of small intensity at higher BE values (Ag3d$_{5/2}$ at 369.00 eV) is attributed to the more oxidized surface Ag bonded with an organic structure, as suggested in the literature for analogous systems [89].

The fitting procedure on the Au4f spectrum (figure 5.1, panel B), collected on *AuNPs/3MPS* sample, allowed identifying the presence of two spin-orbit pairs as well. The first Au4f$_{7/2}$ component was found at 83.96 eV BE value, as expected for metallic gold atoms in the bulk of nanoparticles. The second Au4f$_{7/2}$ component (84.48 eV BE) is associated to the surface gold atoms that are chemically bonded to the 3MPS molecule sulphur [80]. The small amount detected for the metal associated to the covalent bond with sulphur (see table 5.1) is consistent with the nanoparticles dimension. Indeed, the percent of metal atoms located on the nanoparticle surface suggests a small surface to volume ratio, as expected in case of particles with dimensions higher than 5 nm.

To probe the chemical environment at the interface between NPs and 3MPS thiol, SR-XPS S2p core levels signals were collected and analyzed. The spectra and complete BE, FWHM (full width at half maximum), atomic ratio and assignments for the functionalized nanoparticles are shown in figure 5.2 (panels B and C) and table 5.2, respectively. The S2p core level of a thick film of pure pristine 3MPS deposited onto a polycrystalline gold surface (Au/Si(111) wafer) was also studied for comparison, as reported in panel A of figure 5.2.

The S2p SR-XPS data collected on thick film of pure pristine 3MPS were used as a reference, thus allowing the identification and assignment of RS-H signal (physisorbed thiol) for functionalized NPs samples. It is noteworthy the absence of the spin-orbit pair at lower BE values, associated to chemisorbed molecules (see table 5.2), indicating the presence of a thick 3MPS molecular overlayer deposited onto the gold substrate, as expected for the preparation method. S2p spectra analysis on *AgNPs/3MPS* and *AuNPs/3MPS* points out four distinct chemical states for S: the spin orbit doublets at lower BE values (BE S2p$_{3/2}$ components at about 161.8 eV, green line) can be associated to RS-M chemical state (where M is the metal, silver or gold, according to the considered sample) [90, 91]; the S2p$_{3/2}$ signal occurring at nearly 163.7 eV BE (blue line) is due to sulphur atoms of the thiol moiety of physisorbed 3MPS molecules; conversely, the spin-orbit pairs at higher BE values (S2p$_{3/2}$ components BE close to 167 and 168.5 eV, magenta and cyan lines, respectively) are related to S in sulfonates functional groups (-SO$_3$-).

The FWHM for XPS S2p signals was always found to be between 1.1 and 1.5 eV, consistently with literature reports on analogous systems [12, 92]. The fraction of S atoms chemisorbed and physisorbed with respect to the sulfonate groups is 1.3:1 for *AgNPs/3MPS* sample and 1:1 for *AuNPs/3MPS* sample, the atomic ratio between the RS-H signal and the sulfonates signals

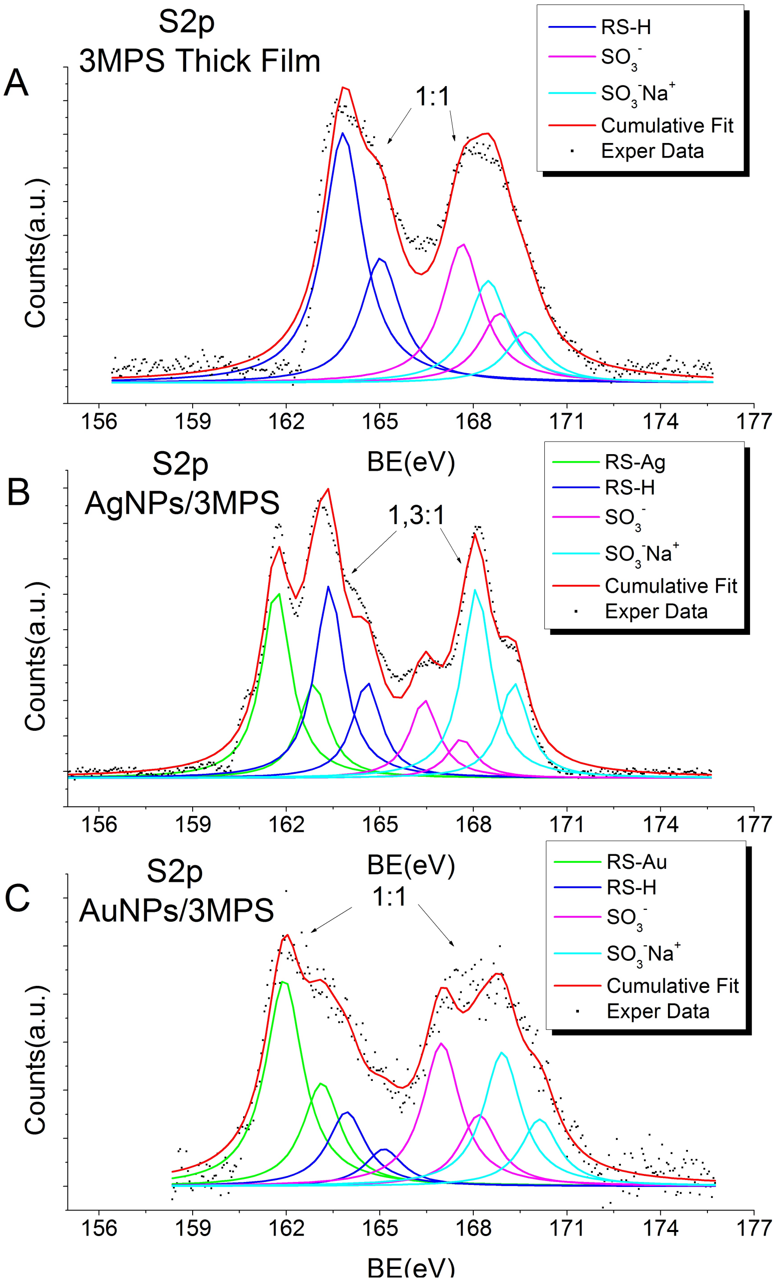

Figure 5.2: S2p core levels spectra of thick film of 3MPS, *AgNPs/3MPS* and *AuNPs/3MPS*.

Sample	**Signal**	**BE**	**FWHM**	***I ratio**	**Assignments**
3MPS thick film	S2p$_{3/2}$	163.82	1.53	51%	RS-H
	S2p$_{3/2}$	167.64	"	28%	SO_3^-
	S2p$_{3/2}$	168.47	"	21%	$SO_3^-Na^+$
AgNPs/3MPS	S2p$_{3/2}$	161.68	1.11	29%	RS-Ag
	S2p$_{3/2}$	163.38	"	30%	RS-H
	S2p$_{3/2}$	166.42	"	12%	SO_3^-
	S2p$_{3/2}$	168.10	"	29%	$SO_3^-Na^+$
AuNPs/3MPS	S2p$_{3/2}$	161.93	1.45	37%	RS-Au
	S2p$_{3/2}$	163.93	"	13%	RS-H
	S2p$_{3/2}$	166.98	"	26%	SO_3^-
	S2p$_{3/2}$	168.92	"	24%	$SO_3^-Na^+$

*I ratios=I_{peak}/I_{tot} signal for a selected element

Table 5.2: SR-XPS S2p core levels data collected on thick film of pure pristine 3MPS and on silver and gold NPs stabilized by 3MPS (BE, FWHM, atomic ratio and assignments).

is 1:1 for thick film of pure pristine 3MPS as well. Taking into account a 5% error on the XPS signal intensity, the observed experimental atomic ratios are in good agreement with the theoretical ones, based on the 3MPS chemical structure, confirming the molecule integrity for all the samples.

Raman and SERS Measurements. The Raman spectrum of bulk 3MPS (in the form of powder) in the region of the vibrational fingerprint and of the characteristic CH_n stretching modes is reported in figure 5.3 (panel A). The Raman signature clearly identifies the molecule and a careful data analysis can lead to the assignment of the main peaks to the molecular vibrational modes [93]. The full Raman bands assignments are reported in table A.1 in Appendix. Among the intense Raman bands (see table A.1 in Appendix) the S=O stretching is clearly recognizable around 1070 cm^{-1}.

The spectra obtained from self-assembled 3MPS conjugated Au and AgNPs are reported in panel B of figure 5.3 (red and blue spectrum, respectively). SERS spectra of organic molecules bound to plasmonic NPs are typically characterized by clear modifications with respect to their conventional Raman counterparts. The most evident feature of SERS data is a redistribution of the spectral weight among the different vibrational bands, and the appearance of new spectral structures, that might be hindered in the conventional Raman spectrum: this is caused by the relaxation of Raman se-

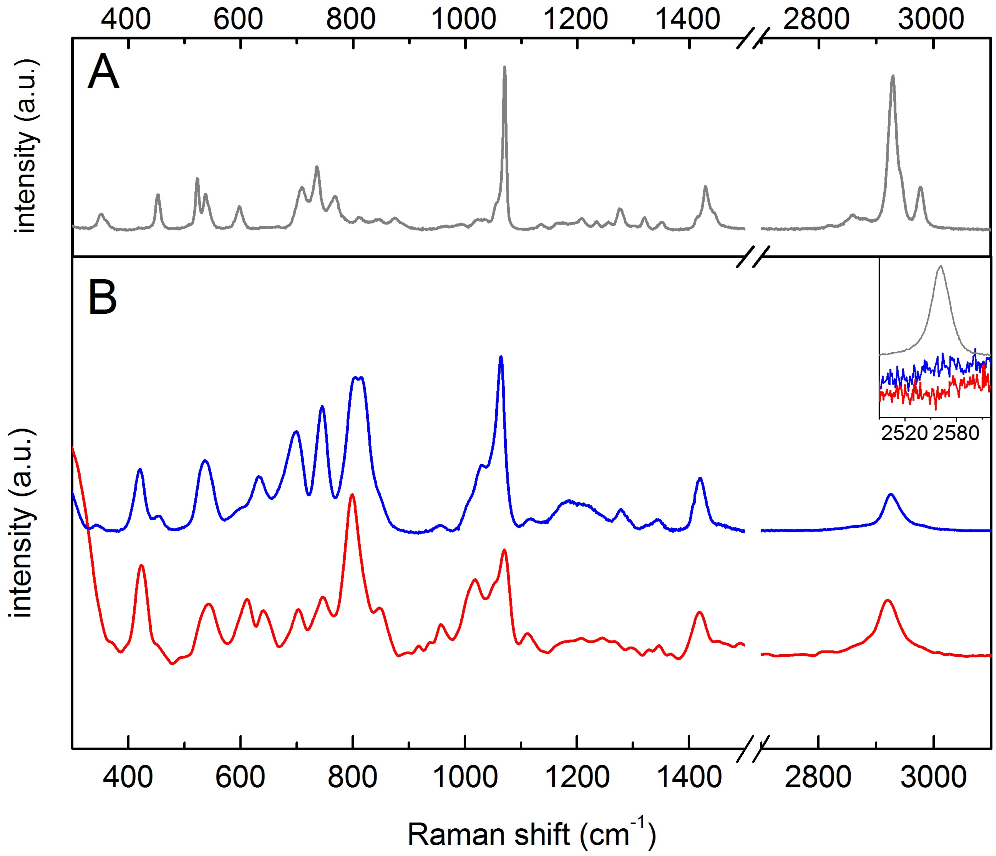

Figure 5.3: Panel A- Raman spectrum of 3MPS; panel B- SERS spectra of *AgNPs/3MPS* (blue) and *AuNPs/3MPS* (red), normalized to the intensity of the CS stretching mode of the sulfonate group (around 540 cm^{-1}, chosen for normalization because isolated and well defined). Spectra are here vertically shifted for clarity. Inset: comparison between 3MPS Raman and SERS spectra in the region of the SH stretching mode (same colour legend). The disappearance of the SH band in the Au and AgNPs samples witnesses the chemical conjugation with 3MPS. Tentative assignment of the main bands in agreement with literature [93, 94] is reported in table A.1 in Appendix.

lection rules and the modification to the molecular electronic polarizability occurring upon binding the molecule to a metal surface [57]. For the same reason, peaks typically show larger width and can result red- or blue-shifted in the SERS case. Based on these considerations, by comparing the results presented in figure 5.3 and table A.1 in Appendix, it is possible to clearly identify the spectra in panel B of figure 5.3 as SERS spectra, which brings further support to the idea of a successful chemical functionalization.

It is worth noting that SERS spectra acquired on gold and silver NPs are in very good agreement. In facts, the main difference observed in the response of the two samples is the overall spectral intensity, which is significantly lower in the case of AuNPs. The low signal enhancement provided by gold is not surprising, as it known that gold substrates typically show lower plasmonic efficiency with respect to silver ones [57, 95].

The assignment of the main SERS bands was performed according to literature [94, 96, 97]. Notice the disappearance of the Raman band centered at $\sim$2560 cm^{-1}, ascribed to the thiol SH stretching mode of 3MPS (see also table A.1 in Appendix), in SERS spectra. As SERS sensing is based on the local field enhancement at the surface of a plasmonic nanostructure, we expect the technique to be more sensitive to the first molecular layer covering the NPs. The disappearance of the SH stretching band suggests the first layer covering the NPs to be composed of chemisorbed molecules. Nevertheless, this does not exclude the presence of exceeding layers of physisorbed molecular species, as observed by SR-XPS measurements.

All the here presented results have been published in the paper *"Comparison between Silver and Gold Nanoparticles Stabilized with Negatively Charged Hydrophilic Thiols: SR-XPS and SERS as Probes for Structural Differences and Similarities"* [78].

5.1.2 DEA thick film, *AuNPs/DEA* and *AgNPs/DEA*

The SR-XPS and SERS analysis carried out on silver and gold NPs stabilized by the *2-diethylaminoethanethiol hydrochloride* (DEA) leaded to analogous results, proving the presence of DEA in the molecular overlayer. The measurements confirmed that the thiol was chemically bonded to the metal surface and the absence of sulfonates SR-XPS signals assessed the effectiveness of the chemical functionalization without molecule degradation.

S2p spectra collected on DEA thick film, *AuNPs/DEA* and *AgNPs/DEA* are reported in the following figure (see figure 5.4) in panel A, B and C, respectively.

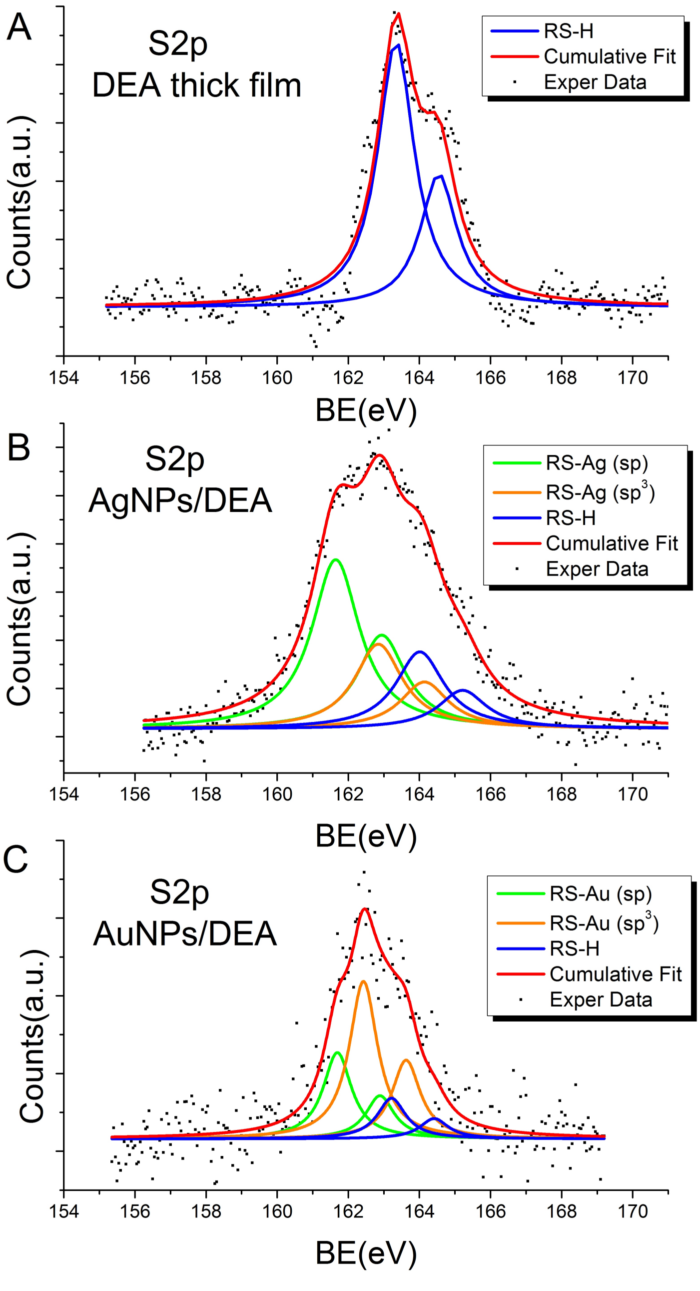

Figure 5.4: S2p core levels spectra of thick film of DEA (panel A), *Ag-NPs/DEA* (panel B) and *AuNPs/DEA* (panel C).

$S2p_{3/2}$, $Au4f_{7/2}$ and $Ag3d_{5/2}$ peaks positions expressed as BEs, FWHM values, and relative intensities are collected in table 5.3 and table 5.4.

Sample	Signal	BE	FWHM	*I ratio	Assignments
DEA thick film	$S2p_{3/2}$	163.34	1.24	1	RS-H
AgNPs/DEA	$S2p_{3/2}$	161.65	1.64	50%	RS-Ag (sp)
	$S2p_{3/2}$	162.94	“	27%	RS-Ag (sp^3)
	$S2p_{3/2}$	164.01	“	23%	RS-H
AuNPs/DEA	$S2p_{3/2}$	161.69	0.97	31%	RS-Au (sp)
	$S2p_{3/2}$	162.43	“	55%	RS-Au (sp^3)
	$S2p_{3/2}$	163.22	“	14%	RS-H

*I ratios=I_{peak}/I_{tot} signal for a selected element

Table 5.3: SR-XPS S2p core levels data collected on thick film of pure DEA and on silver and gold NPs stabilized by DEA (BE, FWHM, atomic ratio and assignments).

Sample	Signal	BE	FWHM	*I ratio	Assignments
AgNPs/DEA	$Ag3d_{5/2}$	368.10	1.22	66%	Ag(0)
	$Ag3d_{5/2}$	369.00	“	34%	Ag(δ^+)
AuNPs/DEA	$Au4f_{7/2}$	83.94	0.45	95%	Au(0)
	$Au4f_{7/2}$	84.34	“	5%	Au(δ^+)

*I ratios=I_{peak}/I_{tot} signal for a selected element

Table 5.4: SR-XPS $Ag3d_{5/2}$ and $Au4f_{7/2}$ metals core levels data collected on silver and gold NPs stabilized by DEA (BE, FWHM, atomic ratio and assignments).

As reported in figure 5.4, the NPs S2p spectra are resolved in six peaks, attributed to three spin-orbit doublets, indicative for three different sulfur species. The S2p signal at higher BE (163-164 eV) corresponds to the physisorbed thiols (see table 5.3), while the presence of two signals observable at lower BE values needs some more detailed discussions.

One reasonable explanation of these spectral features is ascribable to the hybridization (*sp* or sp^3) of the sulphur in the chemical bond with the NPs surface. Despite the fact that the sp^3 configuration is more stable, as a result of an *ab-initio* calculation [98], both the configurations can be present, according to the reaction time and temperature during the synthesis. Leavitt and Beebe found that the S2p binding energy of the sp^3 sulfur is about 1.0 eV higher than that of the sp sulfur [99]. Therefore, assuming that the S2p$_{3/2}$ binding energy of sp^3 exhibits 162.7±0.2 eV which corresponds to the second species peak of bound sulfur, the binding energy of *sp* sulfur is estimated to be about 161.7±0.2 eV, which agrees with the first species peak binding energy in figure 5.4 (panel B and C) [100, 101].

The high surface to volume ratio underlined by the presence of about 34% of metal atoms located on the nanoparticle surface of *AgNPs/DEA* sample (see table 5.4) is a consequence of the NPs size that is < 5 nm for this sample (as shown by the FESEM measurements).

It is noteworthy that these reference XPS spectra can show a noisier and more irregular background than the ones shown in the subsection above (*i.e.* Subsection 5.1.1), this is due to the "DEA single-thiol" functionalization that can lead to more unstable systems (see also the Ag3d$_{5/2}$ FWHM in table 5.4).

Raman and SERS Measurements. The Raman spectrum of bulk DEA in the region of the vibrational fingerprint and of the characteristic CH$_n$ stretching modes is reported in figure 5.5 (panel A). As in the case of 3MPS, we can identify the molecule from the shape of its Raman spectrum by comparing the results with reference data available in the literature [102]. The band assignment of DEA can be performed according to literature studies on similar molecules [103, 104]. The task is more complex than in the case of 3MPS due to the different conformation and protonation condition that the DEA molecule can acquire as a function of environmental pH [105]. Tentative band assignment is reported in table A.2 in Appendix.

The spectra obtained from self-assembled DEA conjugated Au and AgNPs are reported in figure 5.5 (panel B, red and blue spectrum, respectively). As discussed in the case of 3MPS (see section above), SERS spectra present typical modifications with respect to the conventional Raman ones. Apart from the higher intensity per single molecule, which enables the investigation of molecules at the monolayer level, SERS features changes in the spectral shape, which are explained considering the effect of molecule-metal chemical interaction on the molecular electronic polarizability. For this reason, it is possible to state that the spectra shown in panel B of figure 5.5 are the characteristic SERS signature of DEA chemically bonded to Ag or Au nanostructured surfaces. It is not surprising that, as in the case of 3MPS, SERS signal is amplified more efficiently by the silver nanostructured substrate.

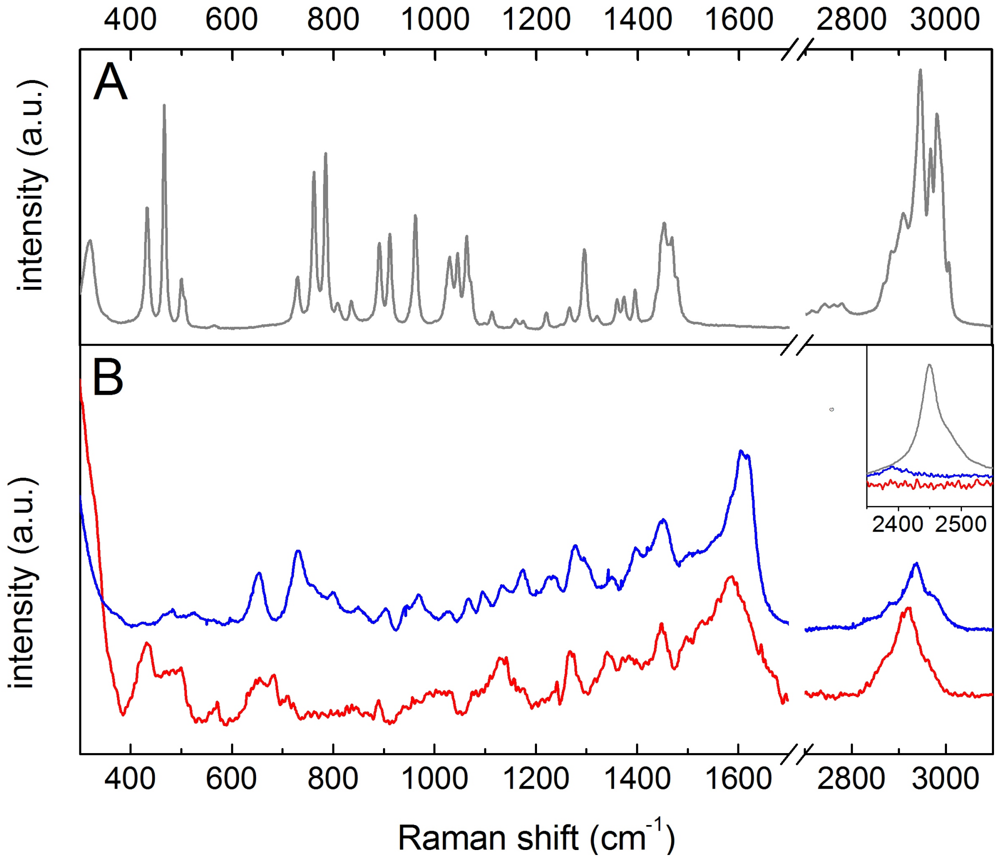

Figure 5.5: Panel A- Raman spectrum of DEA; panel B- SERS spectra of *AgNPs/DEA* (blue) and *AuNPs/DEA* (red), normalized to the intensity of the CH_2 twisting mode (around 1295 cm^{-1} for the Raman spectrum, 1270 cm^{-1} in the SERS spectrum). Spectra are here vertically shifted for clarity. Inset: comparison between DEA Raman and SERS spectra in the region of the SH stretching mode (same colour legend). The strong attenuation of the SH band in the Au and AgNPs samples witnesses the chemical conjugation with DEA. In the case of AgNPs we can recognize a weak spectral feature red-shifted with the Raman band, compatible with the SH stretching assignment, probably coming from a physisorbed molecular layer. Tentative assignment of the main bands in agreement with literature [102, 103, 104, 105, 106] is reported in table A.2 in Appendix.

5.2 Mixed ligands

In this section the "mixed-thiols" functionalized gold and silver NPs systems will be presented and the main measurements results will be shown and discussed.

The chemical functionalization by both 3MPS and DEA thiols leads to more stable systems in aqueous phase (see DLS measurements in table 4.2).

The pure metal Au4f and Ag3d SR-XPS signals were always found at about 83.9 eV and 368.2 eV, respectively (Au4f and Ag3d spectra collected on *AuNPs/3MPS/DEA (1)* and *AgNPs/3MPS/DEA (2)* are reported as an example in figure 5.6). The surface atoms component in the SR-XPS spectra is not visible, due to the samples dimensions[1].

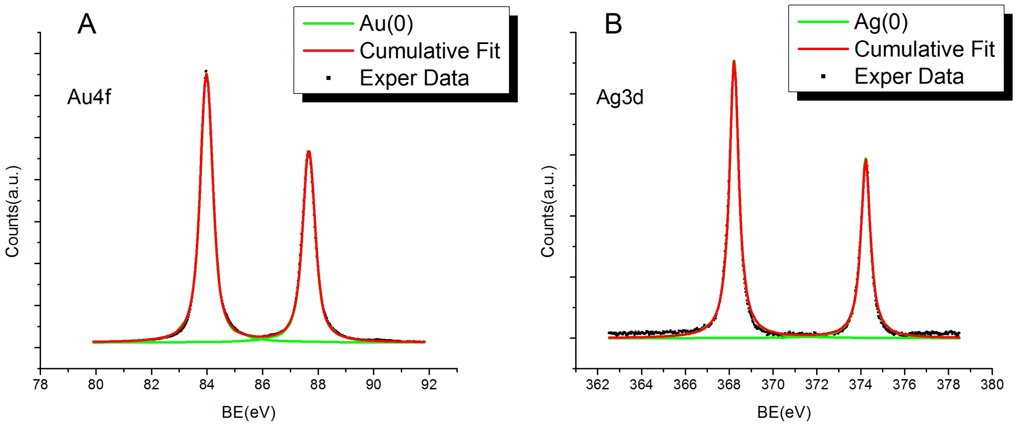

Figure 5.6: Au4f and Ag3d core levels spectra of gold nanoparticles (panel A) and silver nanoparticles (panel B) functionalized with 3MPS and DEA thiols. Metals XPS signals of *AuNPs/3MPS/DEA (1)* and *AgNPs/3MPS/DEA (1)* samples are reported as examples.

Concerning the sulfur SR-XPS signals, the presence of SO_3^- and $SO_3^-Na^+$ components in the S2p spectra of the functionalized AuNPs, assuming that there is no degradation of the molecules, points out the presence of 3MPS thiol in the molecular overlayer. As shown in figure 5.7, the sulfonates atomic percent decreases, as the DEA concentration is increased in the synthesis stoichiometric ratio. Indeed, the intensity of the sulfonates signals for the *AuNPs/3MPS/DEA (1)* sample is $\sim$ 38%, while is about 22% for *AuNPs/3MPS/DEA (2)* sample (as reported in table 5.5).

---

[1] The metals SR-XPS spectra analysis collected on the "mixed-thiols" functionalized nanoparticles points out a small surface to volume atomic percent ratio, as a consequence of the NPs size ($\geq$ 5 nm).

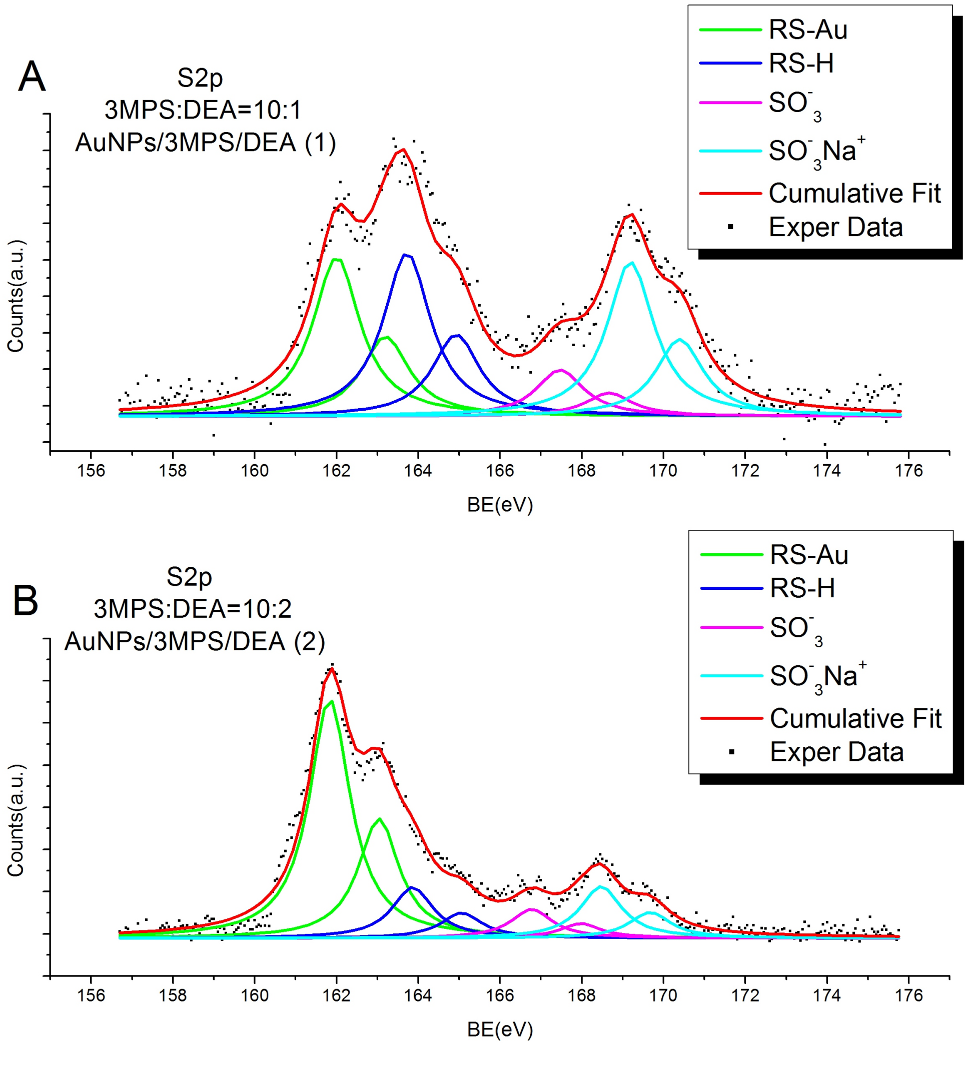

Figure 5.7: Panel A- S2p spectra of *Au/3MPS/DEA (1)*; palen B- S2p spectra of *Au/3MPS/DEA (2)*.

The relative percent of DEA (with respect the 3MPS) can be qualitatively estimated by confronting the atomic percent of sulfonates with respect the chemisorbed and physisorbed sulfur signals. As expected, for *AuNPs/3MPS/DEA (2)* sample the DEA percent is about twice the DEA percent calculated for *AuNPs/3MPS/DEA (1)* sample.

Sample	**Signal**	**BE**	**FWHM**	***I Ratio**	**Assignments**
AuNPs/3MPS/DEA (1)	$S2p_{3/2}$	162.00	1.40	30%	RS-Au
	$S2p_{3/2}$	163.72	"	31%	RS-H
	$S2p_{3/2}$	167.47	"	9%	SO_3^-
	$S2p_{3/2}$	169.19	"	30%	$SO_3^-Na^+$
AuNPs/3MPS/DEA (2)	$S2p_{3/2}$	161.83	1.21	64%	RS-Au
	$S2p_{3/2}$	163.86	"	14%	RS-H
	$S2p_{3/2}$	166.77	"	8%	SO_3^-
	$S2p_{3/2}$	168.47	"	14%	$SO_3^-Na^+$

*I ratios=I_{peak}/I_{tot} signal for a selected element

Table 5.5: SR-XPS S2p core levels data collected on *AuNPs/3MPS/DEA (1)* and *AuNPs/3MPS/DEA (2)* samples (BE, FWHM, atomic ratio and assignments).

Conversely, for AgNPs the intensity of sulfonate signals increases from about 9% to 38% by increasing the DEA amount in the synthesis (*i.e.*, going from 10:1.25 to 10:2.5 in the 3MPS:DEA stoichiometry), as shown in figure 5.8 and table 5.6. At the same time, the relative percent of DEA detected by SR-XPS decreases considerably with respect to 3MPS. This surprising behaviour will be discussed in detail after the presentation of the complementary SERS data results.

It is noteworthy that the discrepancy related to the BE value of physisorbed thiols in the *AgNPs/3MPS/DEA (2)* sample ($S2p_{3/2}$ BE $\approx$ 164.5 eV) and the high ΔBE between the two chemisorbed signals can be explained considering that the S2p XPS spectrum of this sample shows a low signal to noise ratio; for the same reason a BE shift is observed for the sulfonates signals (see the FWHM in table 5.6). The same effect is observed for the $S2p_{3/2}$ SR-XPS signals related to the sulfonates in samples *AuNPs/3MPS/DEA (1)* (see table 5.5) and *AuNPs/3MPS* (see table 5.2) that show a large FWHM. This signal broadening could be due to the samples ageing producing mixed oxidized sulphate-like species.

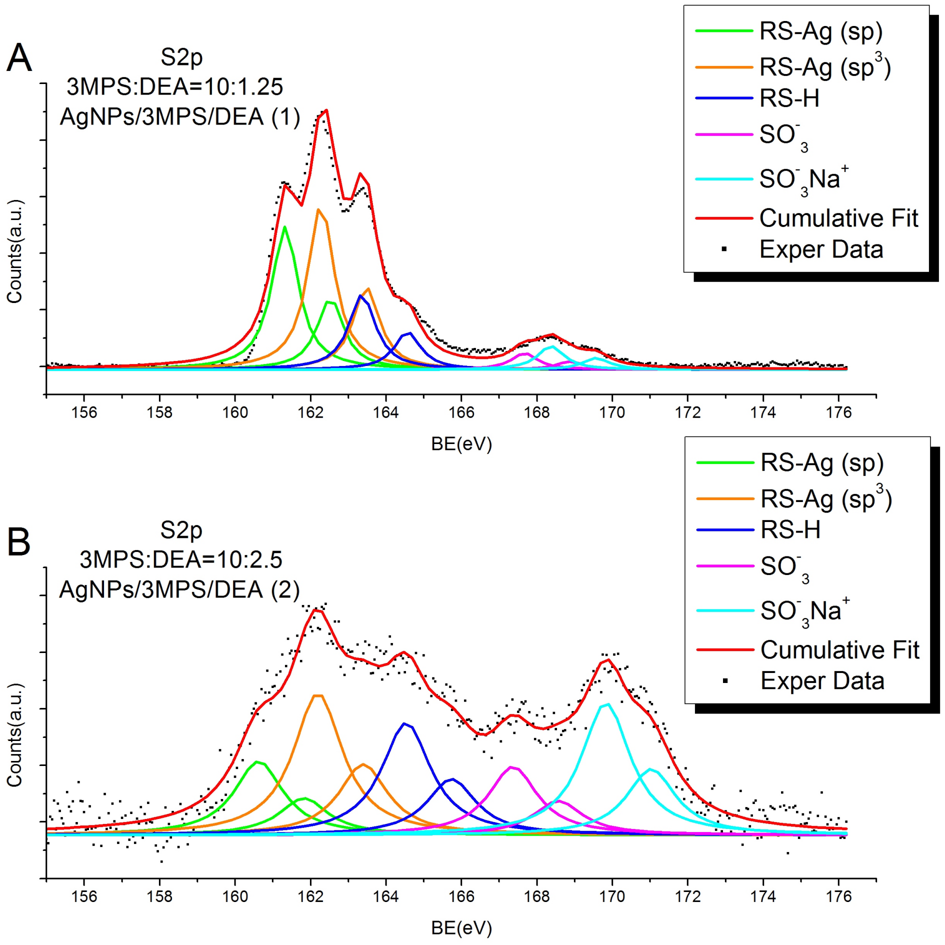

Figure 5.8: Panel A- S2p spectra of *Ag/3MPS/DEA (1)*; panel B- S2p spectra of *Ag/3MPS/DEA (2)*.

Sample	Signal	BE	FWHM	*I Ratio	Assignments
AgNPs/3MPS/DEA (1)	S2p$_{3/2}$	161.32	1.00	34%	RS-Ag (*sp*)
	S2p$_{3/2}$	162.27	"	39%	RS-Ag (sp^3)
	S2p$_{3/2}$	163.36	"	18%	RS-H
	S2p$_{3/2}$	167.66	"	4%	SO_3^-
	S2p$_{3/2}$	168.37	"	5%	$SO_3^-Na^+$
AgNPs/3MPS/DEA (2)	S2p$_{3/2}$	160.62	1.58	14%	RS-Ag (*sp*)
	S2p$_{3/2}$	162.19	"	27%	RS-Ag (sp^3)
	S2p$_{3/2}$	164.53	"	21%	RS-H
	S2p$_{3/2}$	167.36	"	13%	SO_3^-
	S2p$_{3/2}$	169.82	"	25%	$SO_3^-Na^+$

*I ratios=I_{peak}/I_{tot} signal for a selected element

Table 5.6: SR-XPS S2p core levels data collected on *AgNPs/3MPS/DEA (1)* and *AgNPs/3MPS/DEA (2)* samples (BE, FWHM, atomic ratio and assignments).

Raman and SERS Measurements. In figure 5.9, the spectra of AgNPs prepared in presence of different relative concentrations of DEA and 3MPS ligands are plotted and compared to the reference *Ag/DEA* and *Ag/3MPS* spectra.

The organization of different types of molecules in a closed packed structure can cause relevant modification to the Raman/SERS spectra of the *ensamble*, due to the spectral contribution of intermolecular vibrational modes (especially in the low frequency region). Nevertheless, if we consider the SERS spectra of *Ag/3MPS/DEA* samples, it is clearly possible to identify spectral features ascribable to the DEA or 3MPS molecular component (see in figure 5.9 the peaks marks with blue/red arrows, respectively). From a qualitative observation it is straightforward that the characteristic peaks of DEA are more intense in the spectrum of NPs prepared at higher DEA relative concentration. Therefore, it seems that increasing the amount of DEA during preparation results in a more efficient DEA incorporation within the chemisorbed shell around the NP. It is noteworthy that, as already discussed in Subsection 5.1, SERS measurements are almost exclusively sensitive to the first molecular layer around the nanoparticle, due to the local nature of both mechanisms of SERS amplification [36].

In figure 5.10, the spectra of AuNPs functionalized with mixed thiols (at different stoichiometric ratios) are compared to the *Au/DEA* and *Au/3MPS*

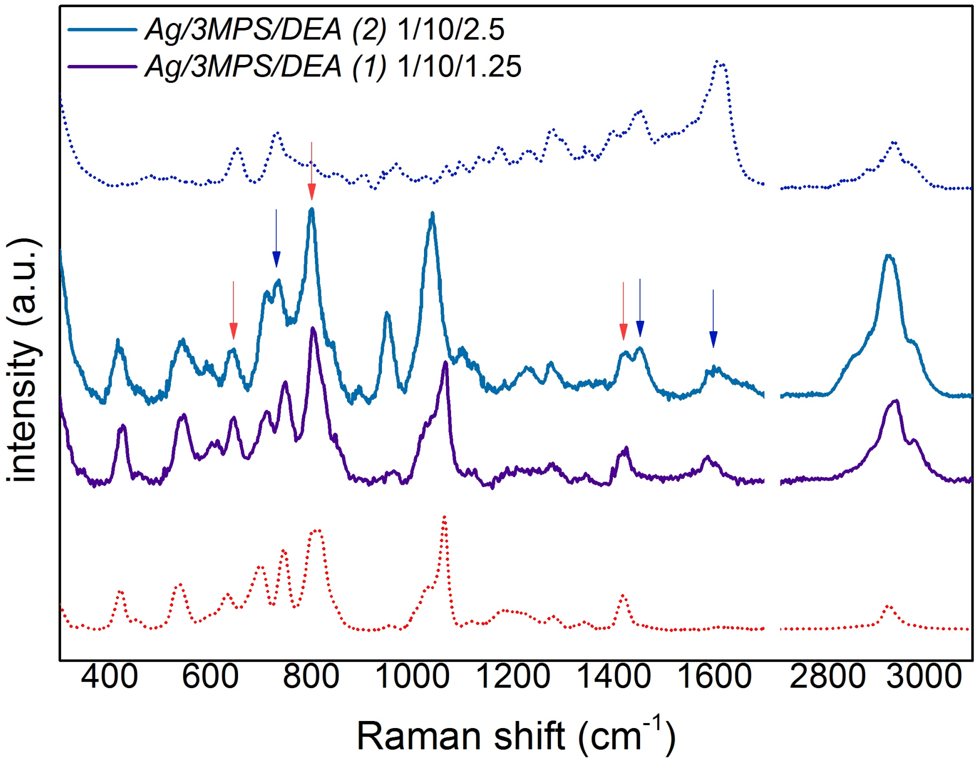

Figure 5.9: Spectra obtained from *AgNPs/3MPS/DEA (2)* (light blue) and *AgNPs/3MPS/DEA (1)* (violet) samples are compared to the SERS references from AgNPs conjugated with DEA (dotted, blue) and 3MPS (dotted, red). Arrows mark characteristic SERS peaks of DEA (blue) and 3MPS (red).

reference SERS spectra.

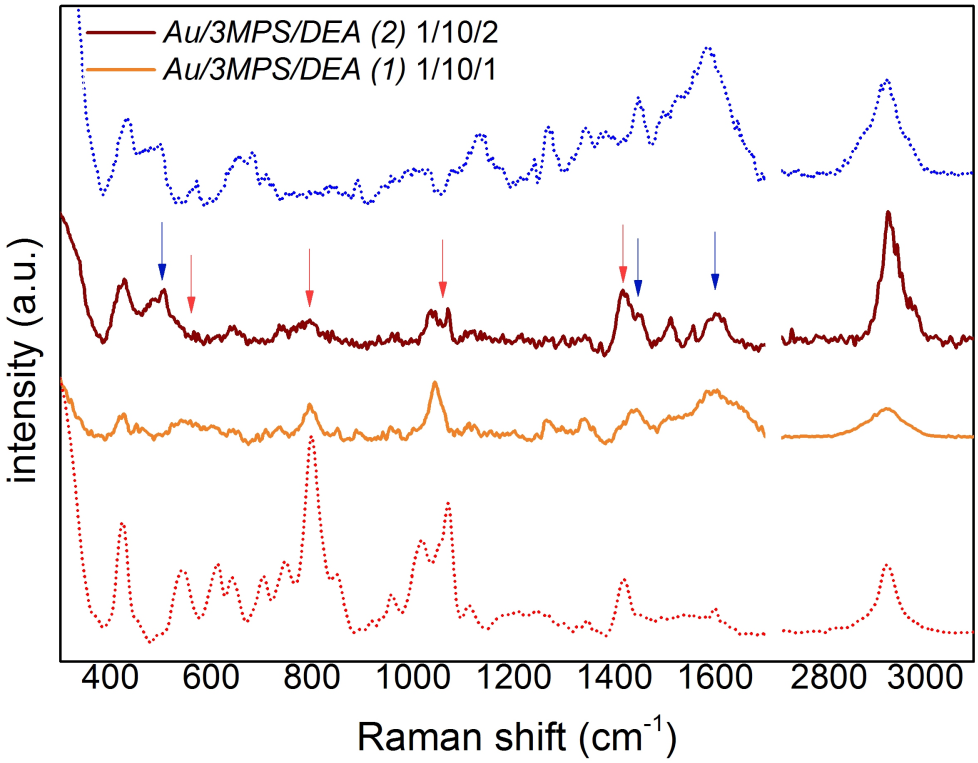

Figure 5.10: Spectra obtained from *AuNPs/3MPS/DEA (2)* (wine) and *AuNPs/3MPS/DEA (1)* (orange) samples are compared to the SERS references from AuNPs conjugated with DEA (dotted, blue) and 3MPS (dotted, red). Arrows mark characteristic SERS peaks of DEA (blue) and 3MPS (red).

In the case of mixed thiol functionalized AuNPs, SERS signal-to-noise ratio is rather weak respect the case of silver NPs (see figure 5.11), and it is therefore really difficult to derive direct information on the conjugation outcome from the shape of the spectra. Indeed, by observing the low wavenumber region (400-600 cm^{-1}) of the mixed thiol SERS spectra, a trend similar to the one discussed for AgNPs can be inferred, but the same argument does not hold for the spectral window between 1400 and 1600 cm^{-1}. It seems there that the spectrum of the sample prepared at higher DEA concentration rather show a predominance of 3MPS spectral features. Despite a quantitative analysis of the spectra is hardly achievable, is it possible to clearly observe on both samples SERS features ascribable to both molecular species, confirming the success of the mixed thiol conjugation.

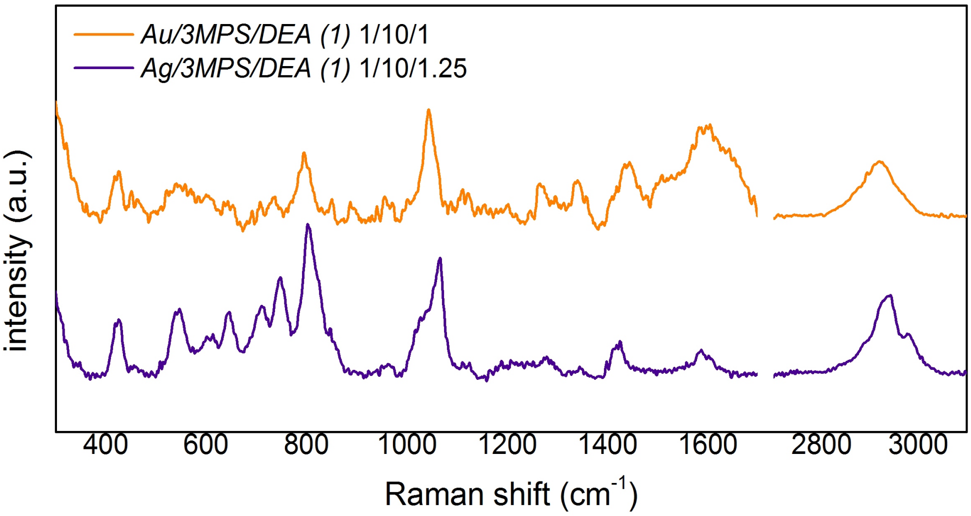

(a) SERS spectra of *AuNPs/3MPS/DEA (1)* and *AgNPs/3MPS/DEA (1)*

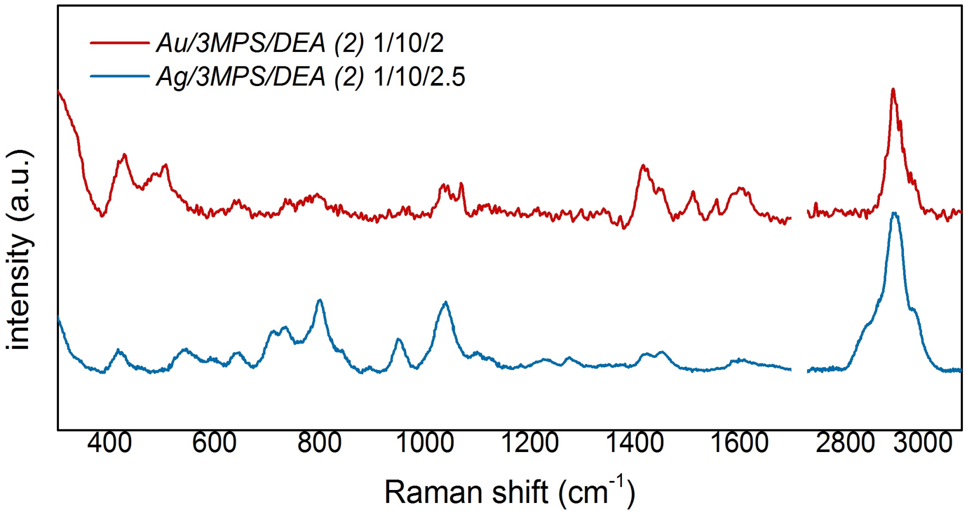

(b) SERS spectra of *AuNPs/3MPS/DEA (2)* and *AgNPs/3MPS/DEA (2)*

Figure 5.11: Comparison between SERS spectra of *AuNPs/3MPS/DEA (1)* (orange) and *AgNPs/3MPS/DEA (1)* (violet) samples (a). Comparison between SERS spectra of *AuNPs/3MPS/DEA (2)* (red) and *AgNPs/3MPS/DEA (2)* (light blue) samples (b).

5.3 Results and Discussions

Concluding, both SERS and SR-XPS analysis proved the effectiveness of the "mixed-thiols" functionalization, confirming the 3MPS and DEA molecular structure integrity. Therefore the presence of sulfonates in the S2p SR-XPS signals can be ascribed to the presence in the molecular overlayer of 3MPS moieties, which can be chemisorbed as well as physisorbed. The SR-XPS experimental results are consistent with the *AuNPs/3MPS*, *AgNPs/3MPS*, *AuNPs/DEA* and mixed-thiols functionalized NPs size ($\geq$ 5 nm), while for the sample *AgNPs/DEA* ($\sim$ 3 nm) the results evidences a higher surface to volume atomic ratio (see table 5.4). Furthermore, SR-XPS allowed us to recognize different chemical states of S, which could not be distinguished by SERS analysis, *i.e.* chemisorbed and physisorbed molecules moieties. Despite the different SERS efficiency of gold and silver nanoparticles, the spectra acquired on the two samples are in good agreement. SERS measurements confirmed the successful functionalization of both AuNPs and AgNPs with 3MPS and DEA ligand, and witnessed the high purity of the system and its stability upon optical excitation.

It is noteworthy that to understand the SR-XPS and SERS data results, some deep considerations about the reaction kinetic should be taken into account. First of all, it is well known that the dynamics of interaction between AgNPs and thiols during the synthesis process is far from being fully elucidated. Indeed, the high AgNPs surface reactivity can influence the thiols adsorption with the formation of a *core-shell* system, resulting in metallic Ag cores surrounded by Ag_2S-like phase and then by an external thiols layer (as shown in figure 5.12). Unfortunately, the BE shift related to the Ag_2S formation leads to an Ag(0)-Ag_2S peak separation too small to be appreciated by means of SR-XPS however, the Ag_2S shell formation in thiols-stabilized AgNPs can be assessed by other techniques, as for example *XAS* [81]. Moreover, the hypothesis that the thiols have different reaction kinetics with the MNPs, according to the surface metallic composition, can be assumed for such complex systems. What is more, the synthesis stoichiometric molar ratio, that plays a key role in the functionalized NPs stability, could lead to overlayers with different molecular ratios depending on the synthesis reaction time and on the molecule steric hindrance.

The discrepancy observed between the trends evidenced by SR-XPS and SERS measurements when increasing the DEA concentration in the synthesis stoichiometric molar ratio can be associated to the different sensitivity of these techniques. The systems dimension and the penetration depth (considering the here used incoming photon energies, *i.e.* 380 eV for S2p core level) of SR-XPS spectroscopy probably lead to a higher sensitivity to the

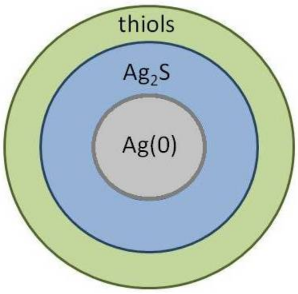

Figure 5.12: Scheme of core-shell configuration for functionalized AgNPs.

physisorbed layer, on the contrary SERS is almost exclusively sensitive to the first molecular layer around the nanoparticle, so to the molecules chemically bonded to metal atoms at the metal NP-thiol interface.

If we hypothesize that the DEA shows a higher reactivity with metals, then the first molecules chemisorbed on the NP surface are the DEA thiols. The steric hindrance of DEA leads to a fast saturation of DEA molecules on the first shell around the metal (see figure 5.13). For AuNPs, several gold sites at the NP surface will be still available for chemical bonds with thiol groups, then the 3MPS can intercalate between DEA chains chemically bonding the AuNP surface. Thus, increasing the DEA amount, an external shell of physisorbed DEA is observed. Therefore, the SR-XPS measurements point out a decrease in the sulfonates intensity (that corresponds to a higher amount of physisorbed DEA respect to 3MPS) associated to an increase of the DEA concentration in the synthesis stoichiometric molar ratio, while SERS analysis indicates a higher amount of 3MPS chemisorbed.

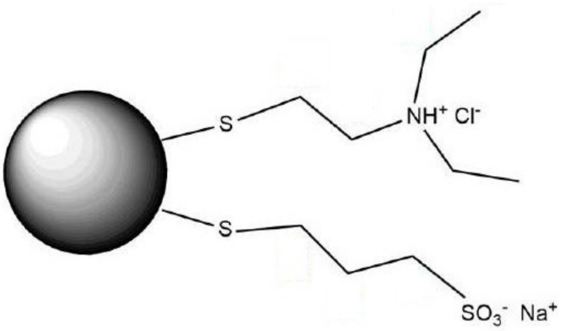

Figure 5.13: The different steric hindrance of 3MPS and DEA thiols can affect the dynamic of their adsorption on the MNP surface.

Concerning the functionalized AgNPs, probably the “quickly reactive” DEA molecules are involved in the Ag_2S shell formation and/or chemically bonded to the surface. As a consequence, increasing the DEA concentration during the synthesis, a higher amount of DEA is chemisorbed on the surface (as indicated by the SERS results), thus only a few metallic silver atoms remains available to form the chemical bond with the 3MPS, which is mostly physisorbed as shown by the increase in the intensity of the S2p SR-XPS signals related to sulfonates.

This hypothesis, based on the complementary information achieved by SR-XPS and SERS, opens interesting perspectives for further studies that will be carried on on the mixed-thiols functionalized NPs. In particular, *Quick-EXAFS* measurements during the synthesis procedure have been planned, and will be performed in the prosecution of this research work.

5.4 Networks of noble metal nanoparticles (Au, Ag, Pd) stabilized by rod-like π-conjugated dithiols

In this section a new system formed by palladium NPs stabilized and interconnected through rod-like bifunctional organometallic thiols containing square-planar Pt(II) centres, *i.e. trans, trans-*$[(HS)Pt(PBu_3)_2(C{\equiv}C\text{-}C_6H_4\text{-}C_6H_4\text{-}C{\equiv}C)(PBu_3)_2Pt(SH)]$ (Pt-DEBP), will be presented and characterized.

Thiol-protected nanoparticles based on palladium are expected to show extremely interesting properties, that makes them suitable for applications in the field of electron transfer processes and in photochemical and electronic devices. The here reported research aims to compare the link of the bifunctional organometallic thiolate complex, which is able to directly link Pt(II) to Pd nanoparticles through a trinuclear Pd-S-Pt bridge, to the analogous Au and Ag-based nanosystems.

The PdNPs, AuNPs and AgNPs show a direct linkage between Pt(II) and the noble metal nanocluster surface through a single S bridge (see figure 5.14).

These nanostructured systems have been characterized by means of SR-XPS, with the aim to probe the molecular and electronic structure of the nanomaterials. The SR-XPS technique allowed to probe the intermolecular interaction occurring between adjacent rod-like dithiols, involving Pt(II) centers and phenyl rings and considerably stabilizing the organic moieties arrangement. All noble metal NPs show diameters ≤ 5 nm, which can be controlled by carefully modulating the synthesis parameters. For all three metals, the nanoparticles inter-linkage, leading to a network of regularly spaced

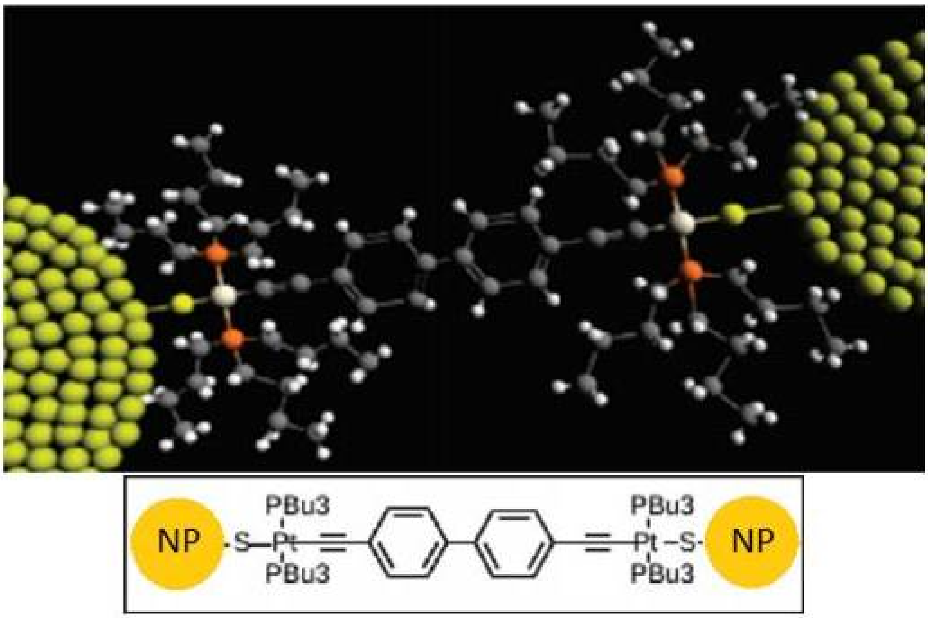

Figure 5.14: Schematic representation of the dithiol bridge between two noble metal nanoparticles.

NPs, can be envisaged with the formation of dyads, as supported by SR-XPS data. This behavior, previously hypothesised for the silver-based nanosystem [20], is here extended to all the investigated noble metals. Furthermore, the comparison between SR-XPS data collected on MNPs and *Self Assembling Monolayers* (SAM) and *Multilayers* (MUL) of the pristine rod-like dithiols deposited onto "flat" polycrystalline gold surfaces leads to ascertain that an electronic interaction occurs between the Pt(II) centres and the biphenyl moieties of adjacent ligands, stabilizing the organic part of the network.

Experimental

SR-XPS experiments were performed at ELETTRA storage ring using the BACH beamline. Photoelectron spectroscopy was performed in the fixed analyser transmission mode with the pass energy set to 50 eV. Photons of 376 eV have been used for C1s, S2p, P2p, Pt4f and Au4f spectral regions; photon energy of 596 eV was chosen to acquire data at the Ag3d and Pd3d core-levels. Both monochromator entrance and exit slits were fixed at 30 μm. Calibration of the energy scale was made by referencing all the gold-containing spectra to the gold Fermi edge, and the Au4f$_{7/2}$ signal was always found at about 83.90 eV.

For samples that did not contain gold, (AgNPs, PdNPs), the signal arising by the noble metal metallic atoms at NPs bulk was used, and a check was also made by with the aliphatic C1s component expected at 285.00 eV. The achieved resolving power was of 0.22 eV. Curve-fitting analysis of the C1s, P2p, Pt4f, S2p, Au4f, Pd3d and Ag3d spectra was performed using Voigt curves as fitting functions, after Shirley's background subtraction. $S2p_{3/2,1/2}$, $Ag3d_{5/2,3/2}$, $Pd3d_{5/2,3/2}$, $Au4f_{7/2,5/2}$ and $Pt4f_{7/2,5/2}$ doublets were fitted by using the same full width at half-maximum (FWHM) for each pair of components of the same core level, a spin-orbit splitting of, respectively, 1.2 eV, 6.0 eV, 5.3 eV, 3.7 eV and 3.3 eV and branching ratios $S2p_{3/2}/S2p_{1/2}=2/1$, $Ag3d_{5/2}/Ag3d_{3/2}=3/2$, $Pd3d_{5/2}/Pd3d_{3/2}=3/2$, $Au4f_{7/2}/Au4f_{5/2}=4/3$ and $Pt4f_{7/2}/Pt4f_{5/2}=4/3$.

When several different species were individuated in a spectrum, the same FWHM value was used for all individual photoemission bands.

Preparation of SAMs and MULs of rod-like Pt(II) dithiol on polycrystalline gold surface

In order to prepare the self assembled monolayer (SAM), the terminal thiol compound *trans, trans-[(HS)-Pt(PBu*$_3$*)*$_2$*-C≡C-C*$_6$*H*$_4$*-C*$_6$*H*$_4$*-C≡C-Pt(PBu*$_3$*)*$_2$ *(SH)]* (Pt-DEBP) was *in situ* obtained by a deacetylation procedure carried out from the precursor thiolate and allowed to self assemble on polycrystalline gold surfaces (Au/Si(111) wafers surfaces). In a typical procedure, the thiolate (30 mg, 0.019 mmol) was dissolved in 20 mL of THF and 260 μL of NH_4OH (30%) was added. Gold coated silica wafers prepared by growing Au film 4000 Å thick onto Si(111) substrates were cut into slides (ca. 1 cm^2) and washed with several organic solvents, *i.e.* acetone, ethanol, chloroform and blown dry with nitrogen. The thiol solution was stirred at 30°C for 2 h, filtered on celite and freshly washed gold substrates were dipped into the solution for 4 hours to achieve the anchoring. The obtained multilayer (MUL) was rinsed with different solvents (ethanol, THF and acetone) in order to achieve the formation of a film in the monolayer thickness regime (namely SAM). The same procedure, without the final washing step, was applied to obtain MUL sample.

SR-XPS investigation

With the aim to probe the chemical and electronic interaction at the interface between noble metal NPs and rod-like ligand, high resolution SR-XPS measurements were carried out at C1s, P2p, S2p, Pt4f and Au4f or Pd3d or

Ag3d core levels for all the considered samples (for complete BE, FWHM, atomic ratio values and assignments, see table A.3 in Appendix). Data collected on SAM and MUL of the same molecules anchored on polycrystalline gold substrates (Au/Si(111) wafers) were also analyzed for comparison; in particular, the S2p signal analysis performed for SAM and MUL samples was used as reference for the interpretation of the sulfur spectra collected on the stabilized NPs.

For all samples, P2p$_{3/2}$ and Pt4f$_{7/2}$ BEs were found at about 131.3 eV and 72.6 eV, respectively, as expected for binuclear compounds of PtDEBPn-likePt(II) dimers, evidencing that the organometallic molecules are all surface associated and that Pt-S bond cleavage and/or phospines oxidation and degradation is not occurring, thus allowing to assess the ligands molecular structure stability. Furthermore, SR-XPS measurements allowed to assess the anchoring of the organometallic thiols onto gold substrates as well as to gold, silver and palladium nanoparticles surfaces. To characterize the chemical structure of ligands monolayer and multilayer on gold substrates, the metal and sulfur core level spectra were collected. For SAM, a single pair of spin-orbit components is detected in the Au4f signal with the main Au4f$_{7/2}$ component at 83.89 eV BE related to metallic gold atoms, as expected for a polycrystalline gold substrate covered by a very thin molecular substrate (monolayer). In multilayer sample, Au4f signal intensity is very low, due to the attenuation of the thick overlayer.

Concerning the stabilized NPs, metal core-level signals (*i.e.* Pd3d, Au4f and Ag3d) were collected and analyzed. By means of the curve-fitting analysis, two spin-orbit pairs can be always observed as associated to metal atoms involved in different chemical environments. Characteristically, the signal at lower BE values is attributed to metallic atoms in NPs bulk; on the other hand, the spectral component that occurs at a higher BE value is associated with metal sites coordinating the electron acceptor thiol ligands [14]. More in detail, in Au4f spectrum of AuNPs (see figure 5.15 (a)) a main spin-orbit pair is found at BE values expected for the metallic gold signal (Au4f$_{7/2}$ BE=83.87 eV), and a less intense couple of components at higher BE (Au4f$_{7/2}$ BE=84.47 eV) coherently with positively charged Au atoms belonging to the NP surface and chemically interacting with sulfur (about 46% in the gold atomic percent); for the Ag3d SR-XPS spectrum of AgNPs (shown in figure 5.15 (b)) two doublets can be observed: a main spin-orbit pair at 368.19 eV, as expected for metallic silver, related to the core NPs atoms and a second component at about 368.79 eV, associated to the surface metallic atoms involved in Ag-S-R bridges [21] and corresponding to a 44% in the atomic percent. Likewise, to probe the electronic interaction at PdNP/thiol interface, the Pd3d core level was measured (as shown in figure 5.15 (c)).

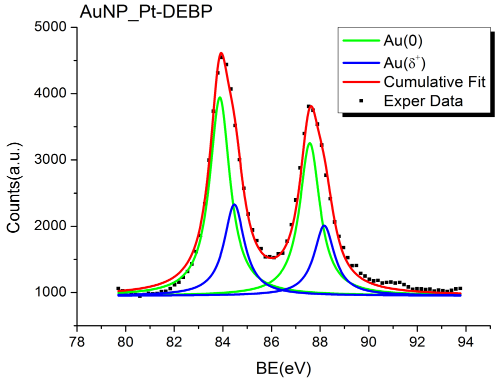

(a) Au4f XPS signal

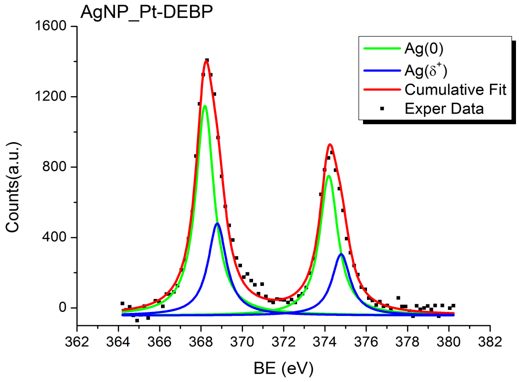

(b) Ag3d XPS signal

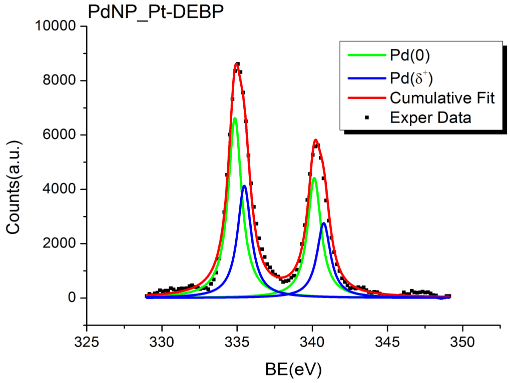

(c) Pd3d XPS signal

Figure 5.15: SR-XPS Au4f (a), Ag3d (b) and Pd3d (c) of respectively gold, silver and palladium NPs stabilized by PtDEBP(SH) dithiols.

The peak fitting procedure allows for individuating two pairs of spin-orbit doublets: the spin-orbit pair at lower BEs, Pd3d$_{5/2}$ BE=334.85 eV, is due to the metallic palladium signal. The signal at higher BE (335.48 eV) is associated with palladium atoms that are partially positively charged because of the chemical bond with the thiol. The surface palladium atoms involved in the Pd-S bond correspond to a 62% in the atomic percent.

S2p spectra collected on SAM and multilayer provided useful references for the interpretation of NPs data, as reported in the following.

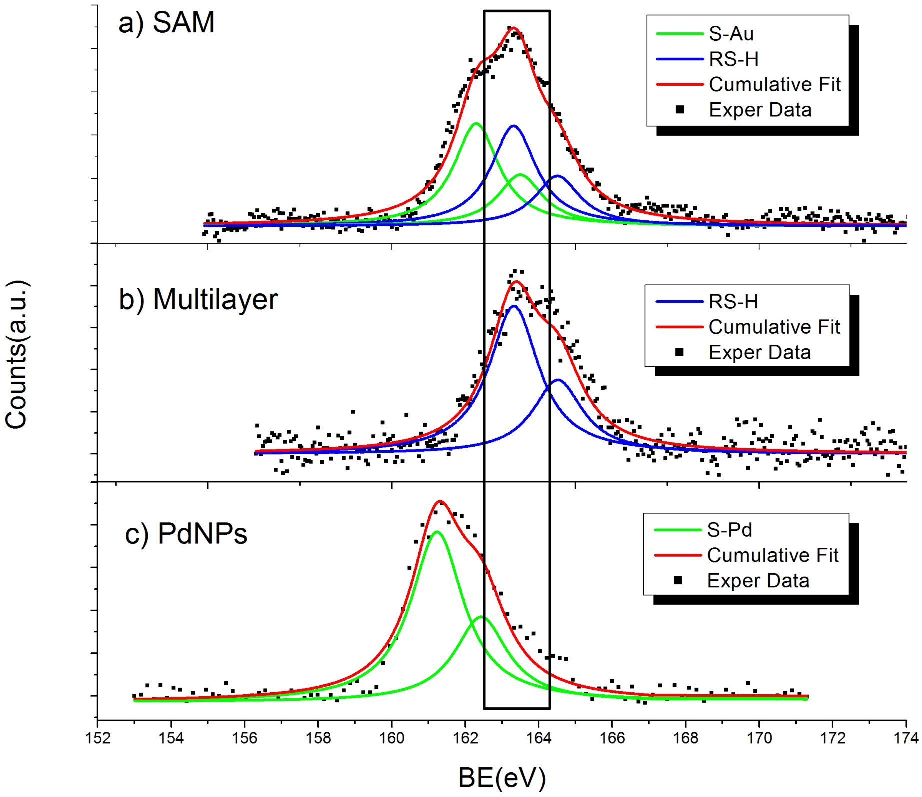

Figure 5.16: SR-XPS S2p of SAM a), multilayer b) and palladium functionalized NPs c), respectively.

As shown in figure 5.16 a), the sulfur signal collected on SAM shows two doublets (S2p$_{3/2}$ BE=162.3 eV and S2p$_{3/2}$ BE=163.3 eV), whereas for the multilayer sample, see figure 5.16 b), only a single spin-orbit pair is detected, with the 3/2 component at about 163.3 eV in BE. Accordingly to literature [107], the spin-orbit doublet at lower binding energy is due to organometallic thiols chemically linked to metals through a covalent S-metal bond, while the signal at higher BE values is associated with sulfur atoms of free thiol terminal groups. It is noteworthy that the atomic ratio between the two components is 1:1 for SAM; this suggests the formation of a monolayer in which each molecule is anchored on the surface while preserving a free terminal group (as depicted in figure 5.17).

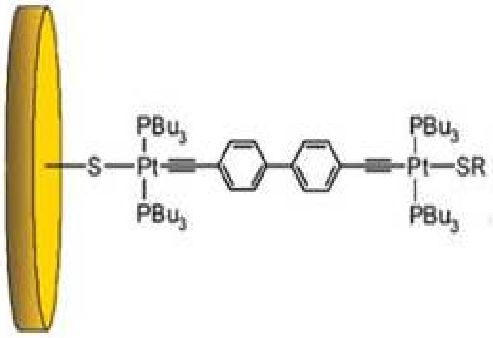

(a) SAM

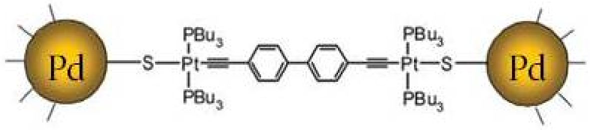

(b) PdNPs

Figure 5.17: Schematic representation of SAM (a) and PdNPs (b) stabilized by PtDEBP(SH)$_2$ dimers.

Conversely, S2p spectra of gold, silver and palladium nanoparticles showed a single signal at low BE values, similarly to the low BE signal observed in SAM (*i.e.* around 160-161 eV in BE) and attributed to organometallic thiols chemically bonded to metals through a S-metal bond [100, 101], suggesting that all thiol groups of MNPs are involved in sulfur-metal chemical bonds (S2p spectrum collected on PdNPs is reported as an example in figure 5.16 c)). This finding support the hypothesis of the formation of a NPs network organized in a “thiols bridges” configuration. Furthermore, the absence of a spin-orbit pair at higher BE values, that would have been indicative for free thiol groups [108], indicates the lack of physisorbed thiols, whose signal usually appears around 163.4 eV [109], or of oxidized sulfur products, which usually give rise to a feature at about 167 eV.

Pt4f SR-XPS spectra gave interesting information about the interaction between adjacent ligand molecules; as reported for similar systems [110], molecular self-assembling is commonly observed in films of polymeric conjugated systems containing transition metal centers σ- or π-bonded to organic main chain. For the here discussed samples, except for the SAM, all Pt4f spectra showed a second component, at higher BE values (≈ 73.5 eV) respect to the previously discussed signal related to square-planar platinum(II). This secondary feature observed in Pt4f spectra can be attributed to Pt atoms electronically interacting with the ethynyl-biphenyl groups of adjacent molecules, as expected for rod-like poly-ynes, giving rise to intra and inter-molecular charge transfer between metal and ligand (see figure 5.18). BE, FWHM, atomic ratio values and assignments of Pt4f collected on all the here presented samples are reported in table 5.7.

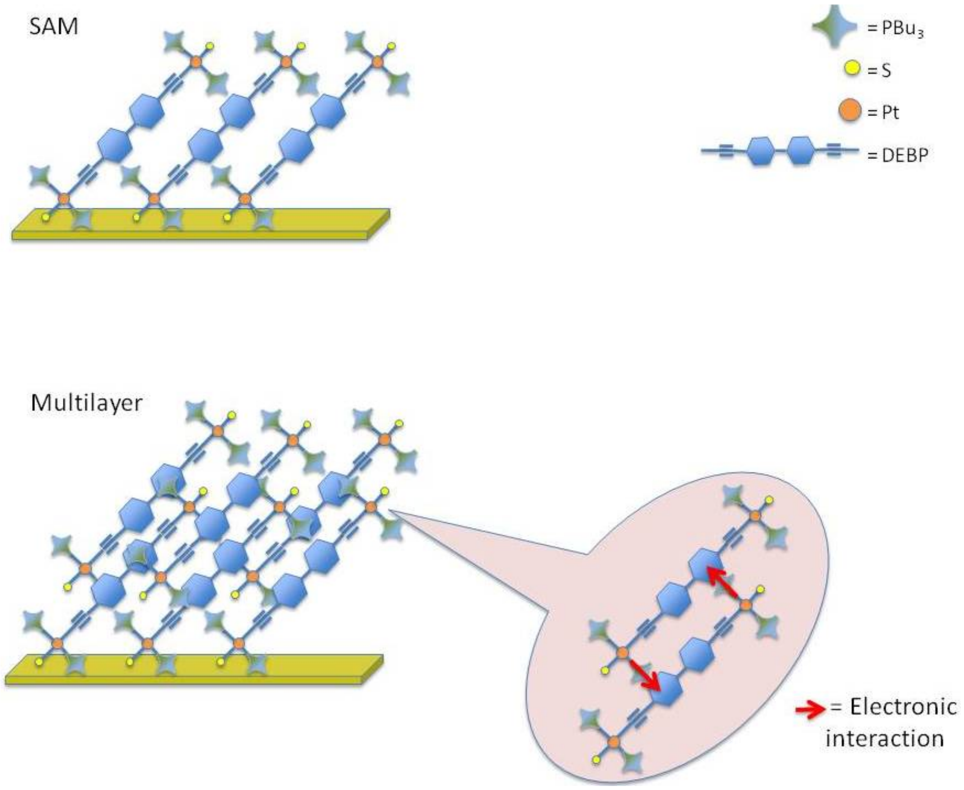

Figure 5.18: SAM and MUL schematic configuration. The presence of the second SR-XPS Pt4f component can be ascribed to the inter-molecular charge transfer between Pt atoms and ethynyl-biphenyl groups of adjacent molecules.

As a matter of fact, a variety of d-transition metal complex, involving metal ions like Ru(II), Re(I), Pt(II) and Ir(III), show interesting optical properties related to inter- and intra-molecular charge transfer (CT). Among these metal complexes, square-planar Pt(II) complexes are quite interesting, since they show metal to ligand CT (MLCT), ligand-centered (LC), and/or

Sample	Signal	BE	FWHM	*I ratio	Assignments
SAM	Pt4f$_{7/2}$	72.83	1.45	1	PtDEBP-like
MUL	Pt4f$_{7/2}$	72.59	1.74	85%	PtDEBP-like
		73.44	1.74	15%	Pt(δ^+)
AuNPs	Pt4f$_{7/2}$	72.61	1.68	85%	PtDEBP-like
		73.59	1.68	15%	Pt(δ^+)
AgNPs	Pt4f$_{7/2}$	72.63	1.64	82%	PtDEBP-like
		73.34	1.64	18%	Pt(δ^+)
PdNPs	Pt4f$_{7/2}$	72.80	1.82	78%	PtDEBP-like
		74.04	1.82	22%	Pt(δ^+)

*I ratios=I$_{peak}$/I$_{tot}$ signal for a selected element

Table 5.7: SR-XPS Pt4f$_{7/2}$ collected on SAM and multilayer of Pt poly-ynes Pt-DEBPn and on NPs stabilized by PtDEBPn (BE, FWHM, atomic ratios and assignments).

metal-metal-to ligand CT (MMLCT) optical emission, depending on ligand structure, temperature, medium and concentration [111]. It can be noticed a switching between metal-to-ligand charge transfer, intraligand charge transfer (ILCT), ligand-to-ligand charge transfer (LLCT), or intraligand (IL) transitions in platinum(II) complexes. These excited states might be interchanged by a change of solvent or pH, or by the introduction of metal ions, thereby yielding a variety of interesting photophysical properties [112].

Therefore the presence of a second doublet in the Pt4f of multilayer and NPs samples (see figure 5.19 and figure A.1 in Appendix) seems to be due to inter-chain interactions arising between metal centers and adjacent acetylene moieties and aromatic rings.

This behavior in the self-assembling organization of dinuclear Pt(II)-based complexes and organometallic poly-ynes was already observed and reported in previous works [113]. Conversely, the Pt4f signal of SAM shows a single spin-orbit pair, confirming the formation of a monolayer without inter-chain interactions [114], probably due to the larger inter-chain distances, and/or to a different molecular packing that does not allow Pt-phenyl ring communication. Generally speaking, Pt4f and S2p spectra collected on SAM suggest the presence of a molecular orientation, as already observed in thin films of Pt-DEBP and Pd-DEBP deposited onto Au/Si(111) substrates and investigated by *angular dependent NEXAFS spectroscopy* [115]; this aspect will be subject to a future investigation.

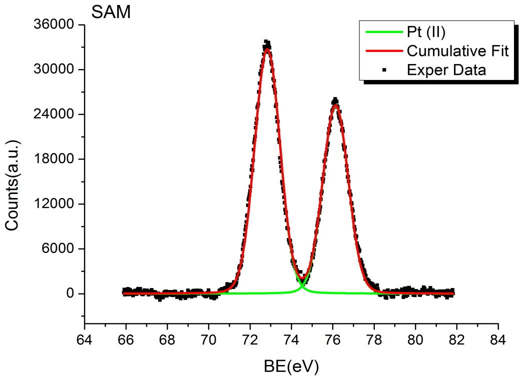

(a) Pt4f XPS signal (SAM)

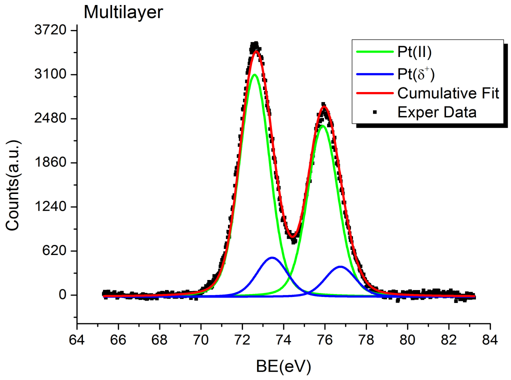

(b) Pt4f XPS signal (MUL)

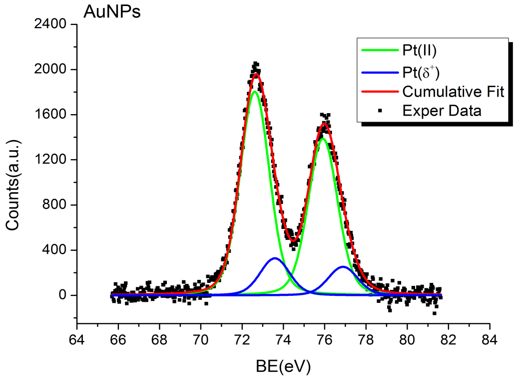

(c) Pt4f XPS signal (AuNPs)

Figure 5.19: SR-XPS Pt4f of SAM, multilayer and gold functionalized NPs, respectively.

Conclusions

The synthesis and characterization of palladium nanoparticles (PdNPs) stabilized by a novel bifunctional thiolate organometallic complex containing Pt(II) centers is reported. A self assembled monolayer (SAM) and a multilayer (MUL) of the organometallic complex deposited onto gold surfaces were prepared and investigated as a reference. PdNPs with an average diameter 4±1 nm were obtained and linkage between the nanoparticles can be envisaged with the formation of dyads. Synchrotron Radiation induced X-ray photoelectron spectroscopy (SR-XPS) measurements allowed to assess the covalent attachment of the sulfur atoms as thiolates to the surface of metals. S2p spectra of PdNPs showed a single signal, suggesting that the organometallic dithiol can graft vicinal nanoparticles with both terminal groups in dyads. The new hybrids show a direct link between Pt(II) and Pd nanoparticles through a single S bridge, confirming the hypothesised achievement of $2D$ or $3D$ networks. Furthermore, the comparison between SR-XPS data collected on MNPs and SAM and MUL of the pristine rod-like dithiols deposited onto “flat” polycrystalline gold surfaces leads to ascertain that an electronic interaction occurs between the Pt(II) centres and the biphenyl moieties of adjacent ligands, stabilizing the organic part of the network; this behaviour was observed for all noble-metal NPs, *i.e.* AuNPs, AgNPs and PdNPs.

In conclusion, the here demonstrated ability to obtain networks of regularly spaced noble metal nanoparticles, successfully tested on three different noble metals, opens outstanding perspectives in the field of optoelectronics. As a future perspective, a more detailed analysis of this system should be carried out by means of well suited spectroscopic techniques, such as *High Resolution Infrared (IR) Spectroscopy* and *Resonant Photoemission Spectroscopy* (RPES), to confirm and deeply understand the metal/ligand charge transfer mechanism. Indeed, using the absorption edge of Pt4f$_{7/2}$ as source e-nergy, is it possible to obtain resonant photoemission of the valence band. This resonant photoemission enables to enhance intensity and resolution in photoemission study for low-cross-section structures as valence band.

The results above, supported by *Field Emission Scanning Electron Microscopy* (FESEM) images, will be soon published in the article *“Networks of noble metal nanoparticles (Au, Ag, Pd) stabilised by rod-like π-conjugated dithiols: molecular and electronic structure and morphology”.*

Conclusions

The electronic and molecular structure, as well as the chemical nature of noble metal (silver, gold) nanoparticles (AgNPs, AuNPs) stabilized by the negatively charged hydrophilic organic thiol *Sodium 3-mercapto-1-propanesulfonate* (3MPS) and the *2-diethylaminoethanethiol hydrochloride* (DEA) has been probed combining Synchrotron Radiation-induced X-ray Photoelectron Spectroscopy (SR-XPS) and Surface Enhanced Raman Spectroscopy (SERS).

Complementary information about the electronic, chemical and molecular structure can be obtained combining SERS and SR-XPS data, allowing to evidence structural similarities and differences related to the noble metal choice. These results coherently suggest the effective 3MPS and DEA chemical adsorption onto the nanoparticle surface, which allows to obtain a stable and biocompatible system, suitable for *ad hoc* further functionalization as required for several applications in biotechnology.

It was observed that the NPs molecular overlayer is made up by covalent bonds between thiols and metallic surface atoms, without degradation of the molecules. SERS spectroscopy was employed for the investigation of the NP molecular conjugation. SERS spectra acquired on the capped AgNPs and AuNPs are in very good agreement and suggest that the same organic layer is covering the NPs. The conjugation with 3MPS and DEA is confirmed by comparing SERS data with the conventional Raman signature of the ligands. The reproducibility of SERS measurements overall points out the high purity and homogeneity of the system and the good integrity of the organic capping layer.

The here reported investigation leads to assess that *AuNPs/3MPS/DEA* and *AgNPs/3MPS/DEA* can be prepared on demand, by following the chemical procedure discussed above, obtaining nanostructured materials that are chemically stable and soluble in aqueous solution; the reported proof of concept is a mandatory prerequisite for *AuNPs/3MPS/DEA* and *AgNPs/3MPS/DEA* applicability in the fields of biophotonics and nanomedicine, through *ad hoc* further functionalization.

In terms of penetration depth and size-sensitivity, SERS and SR-XPS are complementary techniques; in fact, while SERS is specifically sensitive to the metal/thiol interface, SR-XPS, by selecting an appropriate photon energy, can be used to probe the most external layers of a surface. Such complementarity was specifically used in this research work to investigate the molecular organization of the mixed thiols around Au and Ag nanoparticles.

The SR-XPS and SERS measurements carried out on the here presented mixed-thiol functionalized MNPs pointed out interesting information concerning changes arising in the molecular overlayer configuration due to different 3MPS:DEA stoichiometric molar ratios. A careful data analysis leaded to a new interpretation of the interaction dynamics between the two thiols and the metallic atoms on the NP surface.

If we hypothesize that the thiols have different reaction kinetics with metals, in particular assuming that the quickly reactive DEA is the first molecule chemisorbed on the NP surface, the steric hindrance of this thiol leads to a fast saturation of DEA molecules on the first shell around the metal. For AuNPs, several gold sites at the NP surface will be still available for chemical bonds with thiol groups, then the 3MPS intercalates between DEA chains chemically bonding the AuNP surface. Thus, increasing the DEA amount, an external shell of physisorbed DEA is observed. Therefore, the SR-XPS measurements point out a decrease in the sulfonates intensity (that corresponds to a higher amount of physisorbed DEA respect to 3MPS) associated to an increase of the DEA concentration in the synthesis stoichiometric molar ratio, while SERS analysis indicates a higher amount of 3MPS chemisorbed.

Following the “quickly reactive DEA” hypothesis also in the case of functionalized AgNPs, probably the DEA molecules are involved in the Ag_2S shell formation and/or chemically bonded to the surface. As a consequence, increasing the DEA concentration during the synthesis, a higher amount of DEA is chemisorbed on the surface (as indicated by the SERS results), thus only a few metallic silver atoms remains available to form the chemical bond with the 3MPS, which is mostly physisorbed, according to the increase in the intensity of the S2p SR-XPS signals related to sulfonates.

The information acquired by SR-XPS and SERS can be used to stress the structural similarities and differences in the proposed systems, that play a key role in their chemico-physical behaviour, with foreseeable implications in noble metal NPs applicability in different fields of nanomedicine. On the other hand, the different sensitivity to the molecular overlayer of SR-XPS and SERS spectroscopies can be used to explore the potential synergy of these techniques in order to give new insights in the field of nanomaterials.

As a future perspectives and to verify the here formulated hypothesis, the dynamics of interaction during the synthesis process between AgNPs (or AuNPs) and thiols, also with different stoichiometric molar ratios respect the ones here reported, should be deep investigated, for example by means of *Quick EXAFS* measurements at the metal and sulfur absorption edges. The reactions kinetic, for both mixed-thiols functionalized gold and silver NPs, is of about 1÷2 h and the first 25 min are crucial. Therefore, a time-resolved spectroscopy of the reaction kinetic, can be exploited to study the formation of the chemical species, the metals reduction, the Ag_2S shell growth and the sulfur-metal coordination, allowing to explain and fully characterize the chemico-physical changes at the NP-organic ligands interface as the synthesis stoichiometric molar ratio is changed.

Appendix A

Supplementary Information

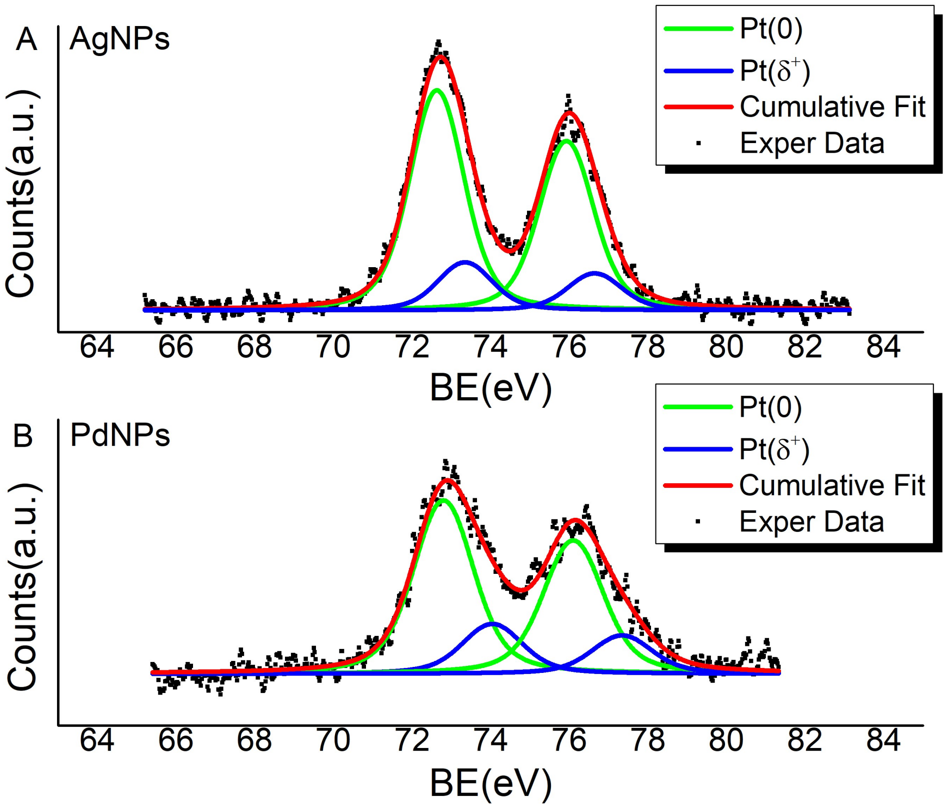

Figure A.1: Pt4f SR-XPS signals for AgNPs (panel A) and PdNPs (panel B) functionalized by PtDEBP(SH)$_2$ dimers.

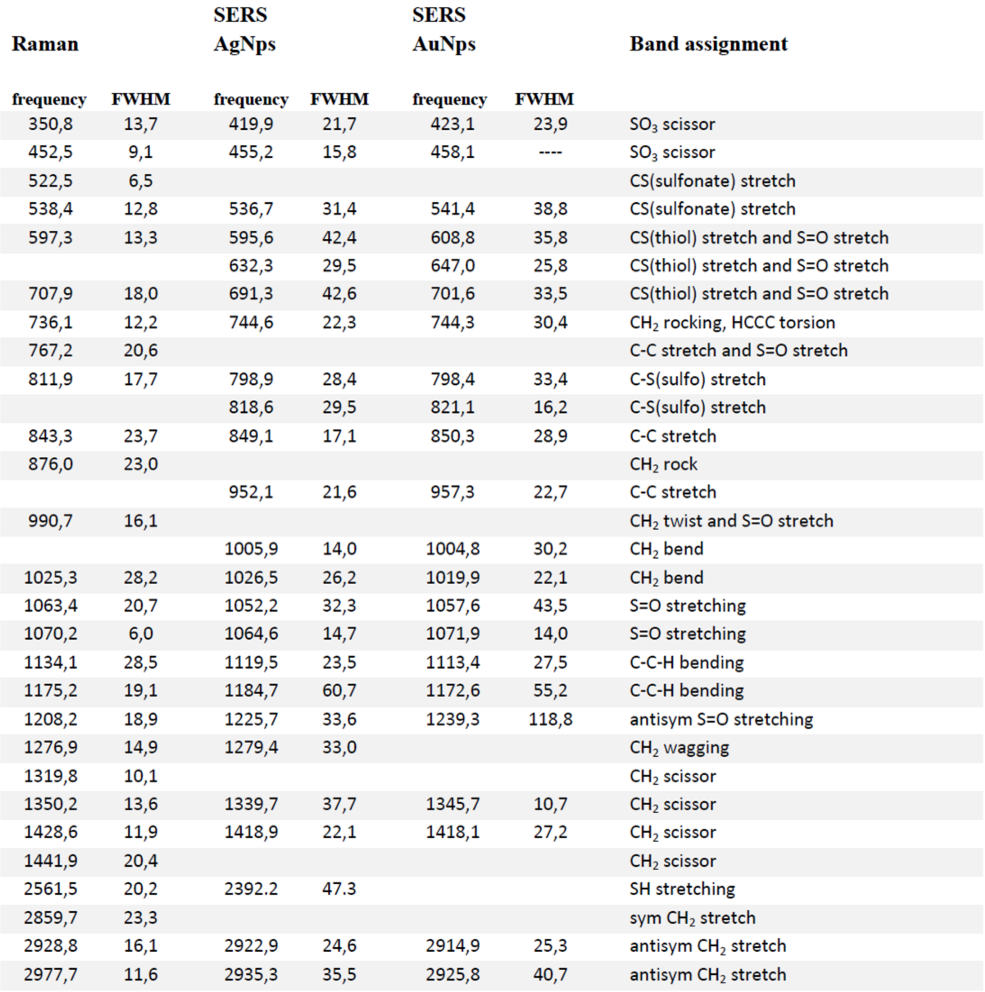

Raman		SERS AgNps		SERS AuNps		Band assignment
frequency	FWHM	frequency	FWHM	frequency	FWHM	
350,8	13,7	419,9	21,7	423,1	23,9	SO_3 scissor
452,5	9,1	455,2	15,8	458,1	----	SO_3 scissor
522,5	6,5					CS(sulfonate) stretch
538,4	12,8	536,7	31,4	541,4	38,8	CS(sulfonate) stretch
597,3	13,3	595,6	42,4	608,8	35,8	CS(thiol) stretch and S=O stretch
		632,3	29,5	647,0	25,8	CS(thiol) stretch and S=O stretch
707,9	18,0	691,3	42,6	701,6	33,5	CS(thiol) stretch and S=O stretch
736,1	12,2	744,6	22,3	744,3	30,4	CH_2 rocking, HCCC torsion
767,2	20,6					C-C stretch and S=O stretch
811,9	17,7	798,9	28,4	798,4	33,4	C-S(sulfo) stretch
		818,6	29,5	821,1	16,2	C-S(sulfo) stretch
843,3	23,7	849,1	17,1	850,3	28,9	C-C stretch
876,0	23,0					CH_2 rock
		952,1	21,6	957,3	22,7	C-C stretch
990,7	16,1					CH_2 twist and S=O stretch
		1005,9	14,0	1004,8	30,2	CH_2 bend
1025,3	28,2	1026,5	26,2	1019,9	22,1	CH_2 bend
1063,4	20,7	1052,2	32,3	1057,6	43,5	S=O stretching
1070,2	6,0	1064,6	14,7	1071,9	14,0	S=O stretching
1134,1	28,5	1119,5	23,5	1113,4	27,5	C-C-H bending
1175,2	19,1	1184,7	60,7	1172,6	55,2	C-C-H bending
1208,2	18,9	1225,7	33,6	1239,3	118,8	antisym S=O stretching
1276,9	14,9	1279,4	33,0			CH_2 wagging
1319,8	10,1					CH_2 scissor
1350,2	13,6	1339,7	37,7	1345,7	10,7	CH_2 scissor
1428,6	11,9	1418,9	22,1	1418,1	27,2	CH_2 scissor
1441,9	20,4					CH_2 scissor
2561,5	20,2	2392.2	47.3			SH stretching
2859,7	23,3					sym CH_2 stretch
2928,8	16,1	2922,9	24,6	2914,9	25,3	antisym CH_2 stretch
2977,7	11,6	2935,3	35,5	2925,8	40,7	antisym CH_2 stretch

Table A.1: Main vibrational components in 3MPS conventional Raman and SERS spectra (obtained on Ag and AuNPs). Band assignment was performed according to references [93, 94].

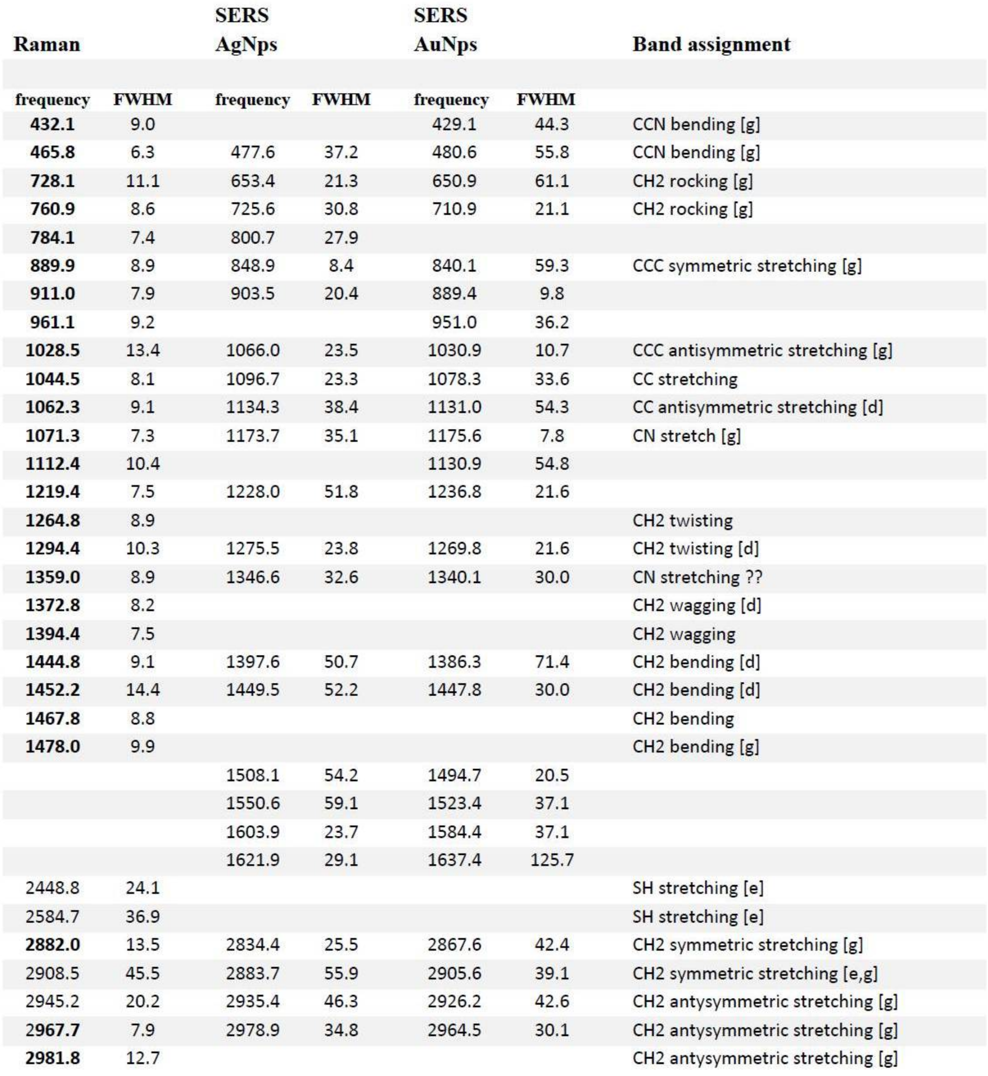

Raman		**SERS AgNps**		**SERS AuNps**		**Band assignment**
frequency	**FWHM**	**frequency**	**FWHM**	**frequency**	**FWHM**	
432.1	9.0			429.1	44.3	CCN bending [g]
465.8	6.3	477.6	37.2	480.6	55.8	CCN bending [g]
728.1	11.1	653.4	21.3	650.9	61.1	CH2 rocking [g]
760.9	8.6	725.6	30.8	710.9	21.1	CH2 rocking [g]
784.1	7.4	800.7	27.9			
889.9	8.9	848.9	8.4	840.1	59.3	CCC symmetric stretching [g]
911.0	7.9	903.5	20.4	889.4	9.8	
961.1	9.2			951.0	36.2	
1028.5	13.4	1066.0	23.5	1030.9	10.7	CCC antisymmetric stretching [g]
1044.5	8.1	1096.7	23.3	1078.3	33.6	CC stretching
1062.3	9.1	1134.3	38.4	1131.0	54.3	CC antisymmetric stretching [d]
1071.3	7.3	1173.7	35.1	1175.6	7.8	CN stretch [g]
1112.4	10.4			1130.9	54.8	
1219.4	7.5	1228.0	51.8	1236.8	21.6	
1264.8	8.9					CH2 twisting
1294.4	10.3	1275.5	23.8	1269.8	21.6	CH2 twisting [d]
1359.0	8.9	1346.6	32.6	1340.1	30.0	CN stretching ??
1372.8	8.2					CH2 wagging [d]
1394.4	7.5					CH2 wagging
1444.8	9.1	1397.6	50.7	1386.3	71.4	CH2 bending [d]
1452.2	14.4	1449.5	52.2	1447.8	30.0	CH2 bending [d]
1467.8	8.8					CH2 bending
1478.0	9.9					CH2 bending [g]
		1508.1	54.2	1494.7	20.5	
		1550.6	59.1	1523.4	37.1	
		1603.9	23.7	1584.4	37.1	
		1621.9	29.1	1637.4	125.7	
2448.8	24.1					SH stretching [e]
2584.7	36.9					SH stretching [e]
2882.0	13.5	2834.4	25.5	2867.6	42.4	CH2 symmetric stretching [g]
2908.5	45.5	2883.7	55.9	2905.6	39.1	CH2 symmetric stretching [e,g]
2945.2	20.2	2935.4	46.3	2926.2	42.6	CH2 antysymmetric stretching [g]
2967.7	7.9	2978.9	34.8	2964.5	30.1	CH2 antysymmetric stretching [g]
2981.8	12.7					CH2 antysymmetric stretching [g]

Table A.2: Main vibrational components in DEA conventional Raman and SERS spectra (obtained on Ag and AuNPs). Band assignment was performed according to references [102, 103, 104].

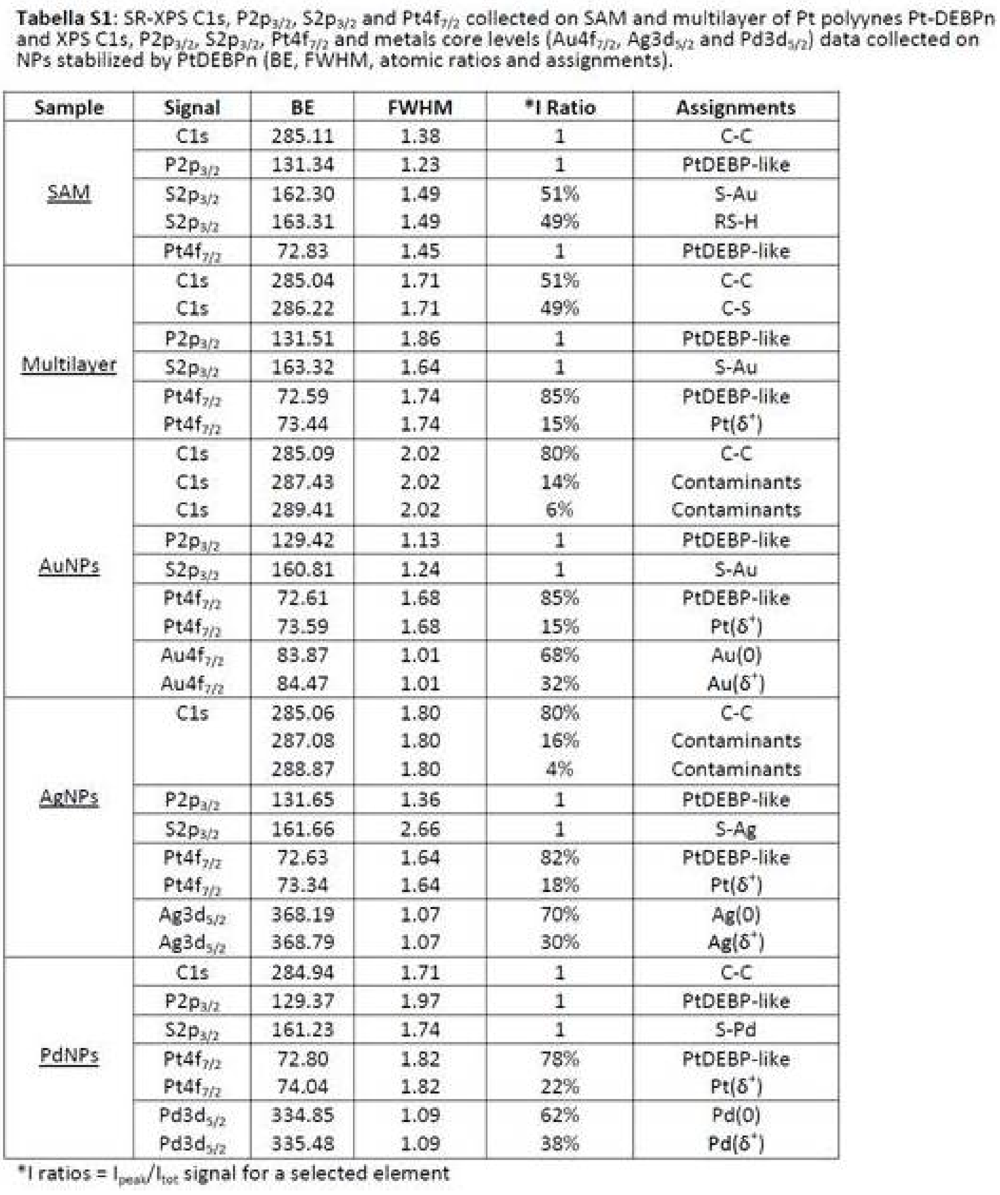

Tabella S1: SR-XPS C1s, P2p$_{3/2}$, S2p$_{3/2}$ and Pt4f$_{7/2}$ collected on SAM and multilayer of Pt polyynes Pt-DEBPn and XPS C1s, P2p$_{3/2}$, S2p$_{3/2}$, Pt4f$_{7/2}$ and metals core levels (Au4f$_{7/2}$, Ag3d$_{5/2}$ and Pd3d$_{5/2}$) data collected on NPs stabilized by PtDEBPn (BE, FWHM, atomic ratios and assignments).

Sample	Signal	BE	FWHM	*I Ratio	Assignments
SAM	C1s	285.11	1.38	1	C-C
	P2p$_{3/2}$	131.34	1.23	1	PtDEBP-like
	S2p$_{3/2}$	162.30	1.49	51%	S-Au
	S2p$_{3/2}$	163.31	1.49	49%	RS-H
	Pt4f$_{7/2}$	72.83	1.45	1	PtDEBP-like
Multilayer	C1s	285.04	1.71	51%	C-C
	C1s	286.22	1.71	49%	C-S
	P2p$_{3/2}$	131.51	1.86	1	PtDEBP-like
	S2p$_{3/2}$	163.32	1.64	1	S-Au
	Pt4f$_{7/2}$	72.59	1.74	85%	PtDEBP-like
	Pt4f$_{7/2}$	73.44	1.74	15%	Pt(δ^+)
AuNPs	C1s	285.09	2.02	80%	C-C
	C1s	287.43	2.02	14%	Contaminants
	C1s	289.41	2.02	6%	Contaminants
	P2p$_{3/2}$	129.42	1.13	1	PtDEBP-like
	S2p$_{3/2}$	160.81	1.24	1	S-Au
	Pt4f$_{7/2}$	72.61	1.68	85%	PtDEBP-like
	Pt4f$_{7/2}$	73.59	1.68	15%	Pt(δ^+)
	Au4f$_{7/2}$	83.87	1.01	68%	Au(0)
	Au4f$_{7/2}$	84.47	1.01	32%	Au(δ^+)
AgNPs	C1s	285.06	1.80	80%	C-C
		287.08	1.80	16%	Contaminants
		288.87	1.80	4%	Contaminants
	P2p$_{3/2}$	131.65	1.36	1	PtDEBP-like
	S2p$_{3/2}$	161.66	2.66	1	S-Ag
	Pt4f$_{7/2}$	72.63	1.64	82%	PtDEBP-like
	Pt4f$_{7/2}$	73.34	1.64	18%	Pt(δ^+)
	Ag3d$_{5/2}$	368.19	1.07	70%	Ag(0)
	Ag3d$_{5/2}$	368.79	1.07	30%	Ag(δ^+)
PdNPs	C1s	284.94	1.71	1	C-C
	P2p$_{3/2}$	129.37	1.97	1	PtDEBP-like
	S2p$_{3/2}$	161.23	1.74	1	S-Pd
	Pt4f$_{7/2}$	72.80	1.82	78%	PtDEBP-like
	Pt4f$_{7/2}$	74.04	1.82	22%	Pt(δ^+)
	Pd3d$_{5/2}$	334.85	1.09	62%	Pd(0)
	Pd3d$_{5/2}$	335.48	1.09	38%	Pd(δ^+)

*I ratios = I_{peak}/I_{tot} signal for a selected element

Table A.3: SR-XPS C1s, P2p$_{3/2}$, S2p$_{3/2}$ and Pt4f$_{7/2}$ collected on SAM and multilayer of Pt polyynes Pt-DEBPn and XPS C1s, P2p$_{3/2}$, S2p$_{3/2}$, Pt4f$_{7/2}$ and metals core levels (Au4f$_{7/2}$, Ag3d$_{5/2}$ and Pd3d$_{5/2}$) data collected on NPs stabilized by PtDEBPn (BE, FWHM, atomic ratios and assignments).

Greetings

First of all I would like to thank Prof. Chiara Battocchio, Prof. Giovanna Iucci, Dr. Guido Infante and Dr. Iole Venditti for the opportunity they gave me to develop and refine my PhD thesis project in their laboratory (Laboratorio di Chimica dei Materiali, University of Rome, “Roma Tre”).

Prof. Battocchio introduced me to the research world giving me a chance to participate in seminaries, conferences and Schools. In particular, I would like to thank Prof. Battocchio for her help and support (not only from the academical point of view) during my entire PhD.

A sincere thank you is dedicated also to Dr. Francesco Porcaro, Dr. Stefano Franchi, Dr. Valeria Secchi and Dr. Chiara Nicolafrancesco for all the moments we have shared, for the scientific and non-scientific quests we faced up, for their help and support and because they were always close to me, when I needed them.

Bibliography

[1] S. Liu, D. Leech and H. Ju, "Application of colloidal gold in protein immobilization, electron transfer and biosensing", Anal. Lett., 2003, 36, 1-19.

[2] "National Nanotechnology Initiative" (NNI), *http //www.nano.gov.*

[3] M. S. Khan, G. D. Vishakante and H. Siddaramaiah, "Gold nanoparticles: A paradigm shift in biomedical applications", Advances in Colloid and Interface Science 2013, 199-200, 44-58.

[4] J. F. Hainfeld, D. N. Slatkin and H. M. Smilowitz, "The use of gold nanoparticles to enhance radiotherapy in mice", Physics in Medicine & Biology, 49, 18, 2004.

[5] E. C. Dreaden, A. M. Alkilany, X. Huang, C. J. Murphy and M. A. El-Sayed, "The golden age: gold nanoparticles for biomedicine", Chem. Soc. Rev. 2012, 41, 2740-2779.

[6] L. Dykman and N. Khlebstov, "Gold nanoparticles in biomedical applications: recent advances and perspectives", Chem. Soc. Rev. 2012, 41, 2256-2282.

[7] Q. H. Wang, K. Kalantar-Zadeh, A. Kis, J. N. Coleman and M. S. Strano, "Electronics and optoelectronics of two-dimensional transition metal dichalcogenides", Nature Nanotechnology, 7, 699-712 (2012).

[8] N. Dur*á*n, M. Dur*á*n, M. B. de Jesus, A. B. Seabra, W. J. F*á*varo and G. Nakazato, "Silver nanoparticles: A new view on mechanistic aspects on antimicrobial activity", Nanomedicine: Nanotechnology, Biology and Medicine, 12 (3), 2016, 789-799.

[9] S. J. McMahon and F. J. Currell, "Nanomedicine: Chapter 3. Gold Nanoparticles for Imaging and Radiotherapy", 2013.

[10] S. Her, D. A. Jaffray and C. Allen, “Gold nanoparticles for applications in cancer radiotherapy: Mechanisms and recent advancements”, Advanced Drug Delivery Reviews, 109 (15), 2017, 84-101.

[11] R. A. Freitas Jr, “Nanotechnology, nanomedicine and nanosurgery”, International Journal of Surgery, 2005, 3 (4), 243-246.

[12] F. Porcaro, C. Battocchio, A. Antoccia, I. Fratoddi, I. Venditti, A. Fracassi, S. Moreno, I. Luisetto, M. V. Russo and G. Polzonetti, “Synthesis of functionalized gold nanoparticles capped with 3-mercapto-1-propansulfonate and 1-thioglucose mixed thiols and «in vitro» bioresponse”, Colloids Surf. B: Biointerfaces, 142 (2016), 408-416.

[13] I. Venditti, C. Palocci, L. Chronopoulou, I. Fratoddi, L. Fontana, M. Diociaiuti and M. V. Russo, “Candida rugosa lipase immobilization on hydrophilic charged gold nanoparticles as promising biocatalysts: Activity and stability investigations”, Colloids and Surfaces B: Biointerfaces, 2015, 131, 93-101.

[14] C. Battocchio, F. Porcaro, S. Mukherjee, E. Magnano, S. Nappini, I. Fratoddi, M. Quintiliani, M. V. Russo and G. Polzonetti, “Gold Nanoparticles Stabilized with Aromatic Thiols: Interaction at the Molecule-Metal Interface and Ligand Arrangement in the Molecular Shell Investigated by SR-XPS and NEXAFS”, J. Phys. Chem. C, 2014, 118, 8159-8168.

[15] M. Prochàzka, “Surface-Enhanced Raman Spectroscopy: Bioanalytical, Biomolecular and Medical Applications”, Springer (2016).

[16] Y. Cheng, M. Wang, G. Borghs and H. Chen, “Gold Nanoparticle Dimers for Plasmon Sensing”, Langmuir 2011, 27, 7884-7891.

[17] M. Li, S. Johnson, H. Guo, E. Dujardin and S. Mann, “A Generalized Mechanism for Ligand-Induced Dipolar Assembly of Plasmonic Gold Nanoparticle Chain Networks”, S. Adv. Funct. Mater. 2011, 21, 851-859.

[18] M. Quintiliani, M. Bassetti, C. Pasquini, C. Battocchio, M. Rossi, F. Mura, R. Matassa, L. Fontana, M. V. Russo and I. Fratoddi, “Network assembly of gold nanoparticles linked through fluorenyl dithiol bridges”, J. Mater. Chem. C, 2014, 2, 2517-2527.

[19] I. Fratoddi, I. Venditti, C. Battocchio, G. Polzonetti, F. Bondino, M. Malvestuto, E. Piscopiello, L. Tapfer and M. V. Russo, “Gold Nanoparticle Dyads Stabilized with Binuclear Pt(II) Dithiol Bridges”, J. Phys. Chem. C, 2011, 115, 15198-15204.

[20] R. Matassa, I. Fratoddi, M. Rossi, C. Battocchio, R. Caminiti and M. V. Russo, “Two-Dimensional Networks of Ag Nanoparticles Bridged by Organometallic Ligand”, J. Phys. Chem. C 2012, 116, 15795-15800.

[21] C. Battocchio, I. Fratoddi, L. Fontana, E. Bodo, F. Porcaro, C. Meneghini, I. Pis, S. Nappini, S. Mobilio, M. V. Russo and G. Polzonetti, “Silver nanoparticles linked by a Pt-containing organometallic dithiol bridge: study of local structure and interface by XAFS and SR-XPS”, Phys. Chem. Chem. Phys. 2014, 16, 11719-11728.

[22] B. H. Bransden and C. J. Joachain, “Physics of atoms and molecules”, 2003.

[23] R. Loudon, “The Quantum Theory of Light”, Chapt. 8, Clarendon Press. (Oxford), 1973.

[24] C. V. Raman and K. S. Krishnan, “A new type of secondary radiation”, Nature, 121 (1928), 501.

[25] S. H. Chen and M. Kotlarchyk, “Interaction of Photons and Neutrons With Matter: An Introduction”, World Scientific (Singapore), 1997.

[26] M. Fleischmann, P. J. Hendra and A. J. McQuillan, “Raman spectra of pyridine adsorbed at a silver electrode”, Chemical Physics Letters, 26 (1974), 163-166.

[27] J. A. Creighton, C. G. Blatchford and M. G. Albrecht, “Plasma Resonance Enhancement of Raman Scattering by Pyridine Adsorbed on Silver or Gold Sol Particles of Size Comparable to the Excitation Wavelength”, Journal of the Chemical Society, Faraday Transactions 2, 75 (1979), 790-798.

[28] J. Gersten and A. Nitzan, “Electromagnetic theory of enhanced Raman scattering by molecules adsorbed on rough surfaces”, Journal of Chemical Physics, 73 (1980), 3023-3137.

[29] M. Moskovits, “Surface-enhanced spectroscopy”, Reviews of Modern Physics, 57 (1985), 783-826.

[30] C. L. Haynes, A. D. McFarland and R. P. Van Duyne, "Surface-enhanced Raman Spectroscopy", Analytical Chemistry 2005, 338-346.

[31] A. Otto, I. Mrozek, H. Grabhorn and W. Akemann, "Surface-enhanced Raman scattering", Journal of Physics: Condensed Matter, 4 (1992), 1143-1212.

[32] E. J. Ayars H. D. and Hallen, "Surface enhancement in near-field Raman spectroscopy", Applied Physics Letters, 76 (2000), 3911-3913.

[33] A. Otto, "The «chemical» (electronic) contribution to surface-enhanced Raman scattering", Journal of Raman Spectroscopy, 36 (2006), 497-509.

[34] A. Kudelski and S. Wojtysiak, "Silica-Covered Silver and Gold Nanoresonators for Raman Analysis of Surfaces of Various Materials", Journal of Physical Chemistry C, 116 (2012), 16167-16174.

[35] K. Kneipp, M. Moskovits and H. Kneipp (eds.), "Surface-Enhanced Raman Scattering: Physics and Applications", Topics in Applied Physics 103, Springer Verlag, Berlin (Germany), 2006.

[36] P. L. Stiles, J. A. Dieringer, N. C. Shah and R. P. Van Duyne, "Surface-Enhanced Raman Spectroscopy", Annu. Rev. Anal. Chem. 2008, 1, 601-626.

[37] S. A. Maier, "Plasmonics: Fundamentals and Applications", Springer Verlag, Berlin (Germany), 2007.

[38] E. C. Le Ru and P. G. Etchegoin, "Principles of Surface Enhanced Raman Spectroscopy and related plasmonic effects", Elsevier B. V., Amsterdam (The Netherlands), 2009.

[39] E. C. Le Ru and P. G. Etchegoin, "Rigorous justification of the $|E|^4$ enhancement factor in Surface Enhanced Raman Spectroscopy", Chemical Physics Letters, 423 (2006), 63-66.

[40] P. G. Etchegoin, C. Galloway and E. C. Le Ru, "Polarization-dependent effects in surface-enhanced Raman scattering (SERS)", Physical Chemistry Chemical Physics, 8 (2006), 2624-2628.

[41] Z. Zhu, T. Zhu and Z. Liu, "Raman scattering enhancement contributed from individual gold nanoparticles and interparticle coupling", Nanotechnology, 15 (2003), 357-364.

[42] M. Baia, F. Toderas, L. Baia, J. Popp and S. Astilean, “Probing the enhancement mechanisms of SERS with p-aminothiophenol molecules adsorbed on self-assembled gold colloidal nanoparticles”, Chemical Physics Letters, 422 (2006), 127-132.

[43] H. Hertz, “Uber einen Einfluss des ultravioletten Lichtes auf die elektrische Entladung (On the influence of ultraviolet light on the electric discharge)”, Ann. Physik 31, 983 (1887); for a very good review on the history of photo emission see: H.P. Bartel, Ch. Kleint: Prog. Surf. Sci. 49, 107 (1995).

[44] J. J. Thompson, “LVIII. On the masses of the ions in gases at low pressures”, Phil. Mag. 48, 547 (1899).

[45] P. Lenard, “Erzeugung von Kathodenstrahlen durch ultraviolettes Licht”, Ann. Physik 2, 359 (1900).

[46] A. Einstein, “Doc 14. On a heuristic point of view concerning the production and transformation of light”, Ann. Physik 17, 132 (1905).

[47] D. Briggs and M. P. Seah, “Practical Surface Analysis, Vol 1, Auger and X-ray Photoelectron Spectroscopy”, 1994.

[48] B. K. Agarwal, “X-ray Spectroscopy”, Springer Series in Optical Sciences, Springer Verlag, 1991 (2nd ed.).

[49] S. Hufner, “Photoelectron Spectroscopy, Principles and Applications”, 2013.

[50] U. Becker, “Photoelectron spectroscopy of atoms”, J. Electron Spectr. And Rel. Phenomena, 75, 23-34 (1995).

[51] O. Travnikova, K. J. Børve, M. Patanen, J. Söderström, C. Miron, L. J. Sæthre, N. Mårtensson and S. Svensson, “The ESCA molecule - Historical remarks and new results”, J. Electron Spectr. And Rel. Phenomena, 185, 191-197 (2012).

[52] V. Schmidt, “Electron spectroscopy of atoms using synchrotron radiation”, Cambridge University Press (Cambridge), 1977.

[53] P. J. Feibelman and D. E. Eastman, “Photoemission spectroscopy - Correspondence between quantum theory and experimental phenomenology”, Phy. Rev. B, 10, 4932-4947 (1974).

[54] S. Mobilio, F. Boscherini and C. Meneghini, “Synchrotron Radiation: Basics, Methods and Applications”, 2015.

[55] K. Laajalehto, I. Kartio and E. Suoninen, “XPS and SR-XPS techniques applied to sulphide mineral surfaces”, Int. J. Miner. Process., 51 (1997), 163-170.

[56] M. Kahraman, E. R. Mullen, A. Korkmaz and S. Wachsmann-Hogiu, “Fundamentals and applications of SERS-based bioanalytical sensing”, Nanophotonics, 6 (5), 2017.

[57] C. Fasolato, F. Domenici, S. Sennato, F. Mura, L. De Angelis, F. Luongo, F. Costantini, F. Bordi and P. Postorino, “Dimensional scale effects on surface enhanced Raman scattering efficiency of self-assembled silver nanoparticle clusters”, Appl. Phys. Lett., 105 (7), 2014, 073105.

[58] B. Sharma, R. R. Frontiera, A. Henry, E. Ringe, and R. P. Van Duyne, “SERS: Materials, applications and the future”, Materials Today, 2012, 15, 1-2.

[59] J. Kneipp, “Interrogating cells, tissues and live animals with new generations of surface-enhanced raman scattering probes and labels”, ACS Nano 2017, 11, 1136-1141.

[60] C. Brechignac, P. Houdy and M. Lahmani, “Nanomaterials and Nanochemistry”, Springer, 2006.

[61] V. Pokropivny, R. Lohmus, I. Hussainova, A. Pokropivny and S. Vlassov, “Introduction to nanomaterials and nanotechnology”, University of Tartu, Institute of Physics, 2007.

[62] Reference figure 3.1: *http://www.ucd.ie/cbni/newsevents/cbni-in-the-news/name,196987,en.html.*

[63] E. M. Andréa, C. Passirania, B. Seijoc, A. Sanchezc and C. N. Montero-Meneia, “Nano and microcarriers to improve stem cell behaviour for neuroregenerative medicine strategies: Application to Huntington’s disease”, Biomaterials, 83, 2016, 347-362.

[64] Reference figure 3.3: *http://www.ucd.ie/cbni/newsevents/cbni-in-the-news/name,196987,en.html.*

[65] R. Casati and M. Vedani, “Metal Matrix Composites Reinforced by Nano-Particles - A Review”, Metals 2014, 4 (1), 65-83.

[66] I. Fratoddi, A. Cartoni, I. Venditti, D. Catone, P. O'Keeffe, A. Paladini, F. Toschi, S. Turchini, F. Sciubba, G. Testa, C. Battocchio, L. Carlini, R. Proietti Zaccaria, E. Magnano, I. Pis and L. Avaldi, "Gold nanoparticles functionalized by rhodamine B isothiocyanate: A new tool to control plasmonic effects", Journal of Colloid and Interface Science 2018, 513, 10-19.

[67] I. Fratoddi, I. Venditti, C. Battocchio, G. Polzonetti, C. Cametti and M. V. Russo, "Core shell hybrids based on noble metal nanoparticles and conjugated polymers: synthesis and characterization", Nanoscale Research Letters 2011, 6 (98).

[68] P. K. Jain, K. S. Lee, I. H. El-Sayed and M. A. El-Sayed, "Calculated absorption and scattering properties of gold nanoparticles of different size, shape, and composition: applications in biological imaging and biomedicine", J. Phys. Chem. B 2006, 110, 7238-48.

[69] O. Salata, "Applications of nanoparticles in biology and medicine", J. Nanobiotechnology 2004, 2:3.

[70] V. V. Mody, R. Siwale, A. Singh and H. R. Mody, "Introduction to metallic nanoparticles", J. Pharm. Bioallied Sci. 2010, 2 (4), 282-289.

[71] T. Tsuzuki, "Commercial scale production of inorganic nanoparticles", International Journal of Nanotechnology 2009, 6, 5-6.

[72] D. C. Kennedy, K. A. Hoop, L. L. Tay and J. P. Pezacki, "Development of nanoparticle probes for multiplex SERS imaging of cell surface proteins", Nanoscale 2010, 2 (8), 1413-1416.

[73] A. Rossi, S. Donati, L. Fontana, F. Porcaro, C. Battocchio, E. Proietti, I. Venditti, L. Bracci and I. Fratoddi, "Negatively charged gold nanoparticles as a dexamethasone carrier: stability in biological media and bioactivity assessment in vitro", RSC Adv. 6 (2016), 99016-99022.

[74] I. Venditti, L. Fontana, F. A. Scaramuzzo, M. V. Russo, C. Battocchio, L. Carlini, L. Gonon, V. H. Mareau and I. Fratoddi, "Nanocomposite Based on Functionalized Gold Nanoparticles and Sulfonated Poly(ether ether ketone) Membranes: Synthesis and Characterization", Materials 2017, 10, 258.

[75] I. Fratoddi, A. Macagnano, C. Battocchio, E. Zampetti, I. Venditti, M. V. Russo and A. Bearzotti, "Platinum nanoparticles on electrospun

titania nanofibers as hydrogen sensing materials working at room temperature", Nanoscale 2014, 6, 9177-9184.

[76] R. Güzel, Z. Üstündağ, H. Ekşi, S. Keskin, B. Taner, Z. G. Durgun, A. A. İ. Turan and A. O. Solak, "Effect of Au and Au@Ag core-shell nanoparticles on the SERS of bridging organic molecules", J. Colloid Interface Sci. 2010, 351, 35-42.

[77] A. C. Templeton, W. P. Wuelfing and R. W. Murray, "Monolayer-Protected Cluster Molecules", Acc. Chem. Res. 2000, 33, 27-36.

[78] L. Carlini, C. Fasolato, P. Postorino, I. Fratoddi, I. Venditti, G. Testa and C. Battocchio, "Comparison between silver and gold nanoparticles stabilized with negatively charged hydrophilic thiols: SR-XPS and SERS as probes for structural differences and similarities", Colloids and Surfaces A: Physicochemical and Engineering Aspects, 532 (5), 2017, 183-188.

[79] I. Venditti, G. Testa, F. Sciubba, L. Carlini, F. Porcaro, C. Meneghini, S. Mobilio, C. Battocchio and I. Fratoddi, "Hydrophilic Metal Nanoparticles Functionalized by 2-Diethylaminoethanethiol: A Close Look at the Metal-Ligand Interaction and Interface Chemical Structure", J. Phys. Chem. C 2017, 121, 8002-8013.

[80] I. Venditti, L. Fontana, I. Fratoddi, C. Battocchio, C. Cametti, S. Sennato, F. Mura, F. Sciubba, M. Delfini and M. V. Russo, "Direct interaction of hydrophilic gold nanoparticles with dexamethasone drug: Loading and release study", Journal of Colloid and Interface Science, 418 (2014), 52-60.

[81] C. Battocchio, C. Meneghini, I. Fratoddi, I. Venditti, M. V. Russo, G. Aquilanti, C. Maurizio, F. Bondino, R. Matassa, M. Rossi, S. Mobilio and G. Polzonetti, "Silver Nanoparticles Stabilized with Thiols: A Close Look at the Local Chemistry and Chemical Structure", J. Phys. Chem. C 2012, 116, 19571-19578.

[82] M. Brust, M. Walker, D. Bethell, D. J. Schiffrin and R. Whyman, "Synthesis of thiol-derivatised gold nanoparticles in a two-phase Liquid-Liquid system", J. Chem. Soc. Chem. Commun. 1994, 801-802.

[83] C. Cametti, I. Fratoddi, I. Venditti and M. V. Russo, "Dielectric Relaxations of Ionic Thiol-Coated Noble Metal Nanoparticles in Aqueous Solutions: Electrical Characterization of the Interface", Langmuir 2011, 27, 7084-7090.

[84] E. M. Goldys and M. A. Sobhan, "Fluorescence of Colloidal Gold Nanoparticles is Controlled by the Surface Adsorbate", Adv. Funct. Mater. 2012, 22, 1906-1913.

[85] H. Bessar, I. Venditti, L. Benassi, C. Vaschieri, P. Azzoni, G. Pellacani, C. Magnoni, E. Botti, V. Casagrande, M. Federici, A. Costanzo, L. Fontana, G. Testa, F.F. Mostafa, S.A. Ibraim, M.V. Russo and I. Fratoddi, "Functionalized gold nanoparticles for topical delivery of methotrexate for the possible treatment of psoriasis", Colloids Surf. B: Biointerfaces, 141 (2016), 141-147.

[86] M. Zangrando, M. Zacchigna, M. Finazzi, D. Cocco, R. Rochow and F. Parmigiani, "Polarized high-brilliance and high-resolution soft x-ray source at ELETTRA: The performance of beamline BACH", Rev. Sci. Instrum., 75 (2004), 31-36.

[87] M. S. Bootharaju and T. Pradeep, "Uptake of toxic metal ions from water by naked and monolayer protected silver nanoparticles: an X-ray photoelectron spectroscopic investigation", J. Phys. Chem. C, 114 (2010), 8328-8336.

[88] NIST X-ray Photoelectron Spectroscopy Database, Version 3.5 (National Institute of Standards and Technology, Gaithersburg, 2003), *http://srdata.nist.gov/xps/*.

[89] A. Mackova, V. Švorčik, P. Sajdl, Z. Strýhal, J. Pavlík, P. Malinský and M. Šlouf, "RBS, XPS, and TEM study of metal and polymer interface modified by plasma treatment", Vacuum, 82 (2008), 307-310.

[90] X.-R. Yu, F. Liu, Z.-Y. Wang and Y. Chen, "Auger parameters for sulfur-containing compounds using a mixed aluminum-silver excitation source", J. Electron Spectrosc. Relat. Phenom., 50 (1990), 159-166.

[91] V. K. Kaushik, "XPS core level spectra and Auger parameters for some silver compounds", J. Electron Spectrosc. Relat. Phenom., 56 (1991), 273-277.

[92] F. Porcaro, L. Carlini, A. Ugolini, D. Visaggio, P. Visca, I. Fratoddi, I. Venditti, C. Meneghini, L. Simonelli, C. Marini, W. Olszewski, N. Ramanan, I. Luisetto and C. Battocchio, "Synthesis and structural characterization of silver nanoparticles stabilized with 3-mercapto-1-propansulfonate and 1-thioglucose mixed thiols for antibacterial applications", Materials, 9 (2016), 1028.

[93] K. G. Schmitt, R. Schmidt, H. F. von-Horsten, G. Vazhenin and A. A. Gewirth, “3-Mercapto-1-Propanesulfonate for Cu Electrodeposition Studied by in Situ Shell-Isolated Nanoparticle-Enhanced Raman Spectroscopy, Density Functional Theory Calculations and Cyclic Voltammetry”, The Journal of Physical Chemistry C, 119(41), 23453-23462 (2015).

[94] A. Kudelski, “Structures of monolayers formed from different HS-$(CH_2)_2$-X thiols on gold, silver and copper: comparitive studies by surface-enhanced Raman scattering”, Journal of Raman Spectroscopy, 34(11), 853-862 (2003).

[95] F. Domenici, C. Fasolato, E. Mazzi, L. De Angelis, F. Brasili, F. Mura, P. Postorino and F. Bordi, “Engineering microscale two-dimensional gold nanoparticle cluster arrays for advanced Raman sensing: an AFM study”, Colloid Surf. A, 498 (2016), 168-175.

[96] Z. D. Schultz, Z. V. Feng, M. E. Biggin and A. A. Gewirth, “Vibrational spectroscopic and mass spectrometric studies of the interaction of bis(3-sulfopropyl)-disulfide with Cu surfaces”, J. Electrochem. Soc., 153 (2), 2006, C97-C107.

[97] K. G. Schimtt, R. Schmidt, H. F. von-Horsten, G. Vazhenin and A. A. Gewirth, “3-Mercapto-1-propanesulfonate for Cu electrodeposition studied by in situ shell-isolated nanoparticle-enhanced raman spectroscopy, density functional theory calculations and cyclic voltammetry”, J. Phys. Chem. C, 119 (41), 2015, 23453-23462.

[98] H. Sellers, A. Ulman, Y. Shindman and J. E. Eilers, “Structure and binding of alkanethiolates on gold and silver surfaces: implications for self-assembled monolayers”, Am. Chem. Soc. 1993, 115, 9389.

[99] A. J. Leavitt and T. P. Beebe Jr., “Chemical reactivity studies of hydrogen sulfide on Au(111)”, Surf. Sci. 1994, 314, 23.

[100] T. Ishida, M. Hara, I. Kojima, S. Tsuneda, N. Nishida, H. Sasabe and W. Knoll, “High Resolution X-ray Photoelectron Spectroscopy Measurements of Octadecanethiol Self-Assembled Monolayers on Au(111)”, Langmuir 1998, 14, 2092-2096.

[101] T. Ishida and N. Choi, “High-Resolution X-ray Photoelectron Spectra of Organosulfur Monolayers on Au(111): S(2p) Spectral Dependence on Molecular Species”, Langmuir 1999, 15, 6799-6806.

[102] *www.sigmaaldrich.com* (see the Raman reference spectrum for DEA).

[103] Z. Hu, X. Wang, W. Wang, Z. Zhang, H. Gao and Y. Mao, "Raman spectroscopy for detecting supported planar lipid bilayers composed of ganglioside-GM1/sphingomyelin/cholesterol in the presence of amyloid-β", Physical Chemistry Chemical Physics, 17 (35), 22711-22720 (2015).

[104] P. Bazylewski, R. Divigalpitiya and G. Fanchini, "In situ Raman spectroscopy distinguishes between reversible and irreversible thiol modifications in L-cysteine", RSC Advances, 7 (5), 2964-2970 (2017).

[105] K. Ohno, S. Matsumoto, M. Aida and H. Matsuura, "Protonation-induced Conformational Changes of 2-(N, N-Dimethylamino) ethanethiol. Importance of Strong N-$H^+ \cdots$ S and N-$H^+ \cdots S^-$ Hydrogen Bonding", Chemistry letters, 32 (9), 828-829 (2003).

[106] J. R. Durig, W. B. Beshir, S. E. Godbey and T. J. Hizer, "Raman and infrared spectra, conformational stability and Ab initio calculations for n-propylamine", Journal of Raman spectroscopy, 20 (5), 311-333 (1989).

[107] D. Nilsson, S. Watcharinyanon, M. Eng, L. Li, E. Moons, L. S. O. Johansson, M. Zharnikov, A. Shaporenko, B. Albinsson and J. Mårtensson, "Characterization of Self-Assembled Monolayers of Oligo(phenyleneethynylene) Derivatives of Varying Shapes on Gold: Effect of Laterally Extended π-Systems", Langmuir, 23, 6170-6181, 2007.

[108] S. Ramsaywack, S. Martic, S. Milton, L. Gates, A. S. Grant, M. Labib, A. Decken and H. -B. Kraatz, "Synthesis and Surface Investigations of N-Substituted 2,5-Dithio-7-azabicyclo[2.2.1]heptanes on Gold Surfaces", J. Phys. Chem. C 2012, 116, 7886-7896.

[109] S. Zhang, G. Leem and T. R. Lee, "Monolayer-Protected Gold Nanoparticles Prepared Using Long-Chain Alkanethioacetates", Langmuir 2009, 25 (24), 13855-13860.

[110] I. Fratoddi, C. Battocchio, A. L. Groia and M. V. Russo, "Nanostructured polymetallaynes of controlled length: Synthesis and characterization of oligomers and polymers from 1,1'-bis-(ethynyl)4,4'-biphenyl bridging Pt(II) or Pd(II) centers", Journal of Polymer Science: Part A: Polymer Chemistry, 45, 3311-3329, 2007.

[111] G. S. Grasa and J. C. Abanades, “CO_2 Capture Capacity of CaO in Long Series of Carbonation/Calcination Cycles”, Inorganic Chemistry, 45 (26), 2006.

[112] X. Han, L. -Z. Wu, G. Si, J. Pan, Q. -Z. Yang, L. -P. Zhang and C. -H. Tung, “Switching between Ligand-to-Ligand Charge-Transfer, Intraligand Charge-Transfer, and Metal-to-Ligand Charge-Transfer Excited States in Platinum(II) Terpyridyl Acetylide Complexes Induced by pH Change and Metal Ions”, Chem. Eur. J. 2007, 13, 1231-1239.

[113] I. Fratoddi, C. Battocchio, A. Furlani, P. Mataloni, G. Polzonetti and M. V. Russo, “Study of chemical structure and conjugation length in organometallic Pt(II) oligomers and polymers containing 1,4-diethynylbenzene derivatives as bridging units”, Journal of Organometallic Chemistry, 674, 10-23, 2003.

[114] R. Vitaliano, I. Fratoddi, I. Venditti, G. Roviello, C. Battocchio, G. Polzonetti and M. V. Russo, “Self-Assembled Monolayers Based on Pd-Containing Organometallic Thiols: Preparation and Structural Characterization”, J. Phys. Chem. A 2009, 113, 14730-14740.

[115] C. Battocchio, I. Fratoddi, M. V. Russo, V. Carravetta, S. Monti, G. Iucci, F. Borgatti and G. Polzonetti, “Binuclear transition-metal complexes on gold: molecular orientation by angular dependent NEXAFS spectroscopy”, Surface Science 2007, 601, 3943-3947.